THEORETICAL AND EXPERIMENTAL DEVELOPMENT OF A ZnO-BASED LATERALLY EXCITED THICKNESS SHEAR MODE ACOUSTIC WAVE IMMUNOSENSOR FOR CANCER BIOMARKER DETECTION

A Thesis
Presented to
The Academic Faculty

by

Christopher D. Corso

In Partial Fulfillment
of the Requirements for the Degree
Doctor of Philosophy in the
School of Biomedical Engineering

Georgia Institute of Technology
August, 2008

THEORETICAL AND EXPERIMENTAL DEVELOPMENT OF A ZnO-BASED LATERALLY EXCITED THICKNESS SHEAR MODE ACOUSTIC WAVE IMMUNOSENSOR FOR CANCER BIOMARKER DETECTION

Approved by:

Dr. William D. Hunt, Advisor
School of Electrical and Computer Engineering
Georgia Institute of Technology

Dr. Peter J. Edmonson
P.J. Edmonson Ltd.
Hamilton, ON, L9B 1A9, Canada

Dr. Bruno Frazier
School of Electrical and Computer Engineering
Georgia Institute of Technology

Dr. Ruth O'Regan
School of Medicine
Emory University

Dr. Dale Edmondson
School of Biochemistry
Emory University

Dr. Marie Csete
School of Medicine
Emory University & The California Institute for Regenerative Medicine

Date Approved: May 9th, 2008

For my family and the love of my life, Mindi

May I always make you proud

ACKNOWLEDGEMENTS

I would first like to thank Dr. William D. Hunt, my advisor and friend for giving me the opportunity and freedom to explore the areas of research that interested, excited, and often dumbfounded me. His continued support and helpfulness throughout my years in the Microelectronic Acoustics Group has been greatly appreciated. I also wish to thank my committee members: Drs. Bruno Frazier, Dale Edmondson, Peter Edmonson, Ruth O'Regan, and Marie Csete for reviewing my thesis and providing me with support and guidance. Special thanks go to Anthony Dickherber, with whom I have worked closely for the past four years. A better person, friend, and researcher cannot be found. I wish to acknowledge the rest of the outstanding members of the acoustics group - Desmond Stubbs, Sang-Hun Lee, Ryan Westafer, John Perng, Adam Wathen, Farasat Munir, and Eric Massey – whom I am proud to call friends and colleagues. It was always a pleasure working with such a good group of people and many good times were had along the way. I would like to thank my family for their constant support and love throughout my academic endeavors. Lastly, I wish to thank my wife for her support and understanding throughout the long days and nights I spent away from home working in the laboratory.

TABLE OF CONTENTS

LIST OF TABLES

Page

LIST OF FIGURES

Page

LIST OF ABBREVIATIONS

APM	Acoustic Plate Mode
BAW	Bulk Acoustic Wave
FBAR	Film Bulk Acoustic Resonator
FEM	Finite Element Modeling
FITC	Fluorescein-Isothiocyanate
FPW	Flexural Plate Wave
IC	Integrated Circuit
LFE	Lateral Field Excitation
Q	Quality Factor
QCM	Quartz Crystal Microbalance
RF	Radio Frequency
SAW	Surface Acoustic Wave
SH-SAW	Shear Horizontal Surface Acoustic Wave
SMR	Solidly Mounted Resonator
STW	Surface Transverse Wave
TE	Thickness Excitation
TSM	Thickness Shear Mode
ZnO	Zinc Oxide

SUMMARY

One of the most promising ways to reduce cancer mortality is through early detection. The five year survival rate for many of the most common cancers is above 95% when the disease is detected in its earliest stages. In contrast, the five year survival rate for advanced stage cancers is less than 30%. These statistics indicate the need for assays that are capable of detecting low quantities of tumor-associated biomarkers. A promising technology in the development of highly sensitive, arrayable biosensors is acoustic wave device technology. Acoustic wave device biosensors measure changes in the resonant frequency of a piezoelectric crystal in response to changes in surface adsorbed mass such as antibody-antigen binding events.

The object of this thesis research was to develop and characterize a new type of acoustic biosensor - a ZnO-based laterally excited thickness shear mode (TSM) resonator in a solidly mounted configuration. The first specific aim of the research was to develop the theoretical underpinnings of the acoustic wave propagation in ZnO. Theoretical calculations were carried out by solving the piezoelectrically stiffened Christoffel equation to elucidate the acoustic modes that are excited through lateral excitation of a ZnO stack. A finite element model was developed to confirm the calculations and investigate the electric field orientation and density for various electrode configurations. A proof of concept study was also carried out using a Quartz Crystal Microbalance device to investigate the application of thickness shear mode resonators to cancer biomarker detection in complex media. The results helped to provide a firm foundation for the design of new gravimetric sensors with enhanced capabilities.

The second specific aim was to design and fabricate arrays of multiple laterally excited TSM devices and fully characterize their electrical properties. The solidly mounted resonator configuration was developed for the ZnO-based devices through theoretical calculations and experimentation. A functional mirror comprised of W and SiO_2 was implemented in development of the TSM resonators. The devices were fabricated and tested for values of interest such as Q, and electromechanical coupling (K^2) as well as their ability to operate in liquids.

The third specific aim was to investigate the optimal surface chemistry scheme for linking the antibody layer to the ZnO device surface. Crosslinking schemes involving organosilane molecules and a phosphonic acid were compared for immobilizing antibodies to the surface of the ZnO. Results indicate that the thiol-terminated organosilane provides high antibody surface coverage and uniformity and is an excellent candidate for planar ZnO functionalization.

The fourth and final specific aim was to investigate the sensitivity of the acoustic immunosensors to potential diagnostic biomarkers. Initial tests were performed in buffer spiked with varying concentrations of the purified target antigen to develop a dose-response curve for the detection of mesothelin-rFc. Subsequent tests were carried out in prostate cancer cell line conditioned medium for the detection of PSA. The results of the experiments establish the operation of the devices in complex media, and indicate that the acoustic sensors are sensitive enough for the detection of biomolecular targets at clinically relevant concentrations.

CHAPTER 1

INTRODUCTION

1.1 Introduction

Most experts agree that early detection is a key component to reducing the mortality rate of cancer. The primary barriers to early detection are insufficient diagnostic markers and the lack of highly sensitive diagnostic tests that are affordable enough for screening purposes. With the exception of prostate specific antigen (PSA) which is FDA approved for prostate cancer screening, no currently known markers are widely regarded to have sufficient sensitivity or specificity for use in screening [1]. However, as screening tests become ever more sensitive, the ability to monitor extremely low concentrations of markers will allow physicians to explore new markers for use in early detection and prevention.

Every year, approximately 33,700 Americans are diagnosed with pancreatic cancer and approximately 32,300 will die from the disease [2]. Pancreatic cancer is one of the most deadly types of cancer with an estimated 5-year survival rate of only 4% [2]. This is in-part due to the fact that most cases of pancreatic cancer go undetected until the cancer has reached an advanced stage. There are, unfortunately, no screening tests that have the sensitivity and specificity needed to screen for pancreatic cancer. One of the best available tests for pancreatic cancer is serum carbohydrate antigen (CA) 19-9 [3, 4]. While CA 19-9 is useful for following the therapeutic response of patients with pancreatic cancer that have an elevated serum CA 19-9 level, there are several significant shortcomings with serum CA 19-9 levels as a screening test for pancreatic cancer. First,

the test is not specific [4]**.** Diseases other than pancreatic cancer, including benign diseases, can elevate serum CA 19-9 levels. Second, the test lacks the sensitivity needed for a diagnostic test. In addition, many of the cancers detected using serum CA 19-9 as a screening test are advanced incurable cancers. Clearly, there is an urgent need for tumor markers and for detection systems capable of measuring slightly elevated amounts of these markers in the body. One potentially valuable marker is mesothelin, a 40-kDa glycoprotein, which was identified by Chang and Pastan in 1994 as an antigen present on the surface of mesothelial cells, mesotheliomas, and ovarian cancers [5] but was not fully characterized until 1996 [6]. In 2001, Argani *et al.* demonstrated that mesothelin is overexpressed in almost all pancreatic adenocarcinomas [7]. Because of this overexpression, the discovery of elevated levels of mesothelin in the blood may prove a sensitive marker for this disease [5, 7-9].

Breast cancer is another disease from which patients and doctors alike could benefit greatly from improved early detection screening tools. Each year, approximately 214,000 Americans are diagnosed with breast cancer and approximately 41,000 will die from the disease [2]. Despite a relatively high five-year survival rate of 88% [2], there exist no true molecular biomarkers for the early diagnosis of breast cancer. Cancer antigen (CA) 27-29 is a monoclonal antibody to a glycoprotein (MUC1) that is present on the apical surface of normal epithelial cells. CA 27-29 is highly associated with breast cancer, although levels are elevated in several other malignancies [1]. The level of CA 27-29 is elevated in approximately one third of women with early-stage breast cancer (stage I or II) and in two thirds of women with late-stage disease (stage III or IV). Another marker, CA 15-3 has been studied in the past as a potential marker for breast

cancer. It is typically used to monitor the course of treatment in women diagnosed with breast cancer, especially advanced stage disease. CA 15–3 levels are rarely elevated in women with early stage breast cancer, but in a study comparing CA 15-3 to CA 27-29 in preoperative serum, both markers showed a statistically significant, direct relationship, with pathological stage [10]. Elevated levels of CA 15-3 have also been correlated with the presence of lymph node metastases in preoperative serum and have been indicated as a possible prognostic marker [11].

A detection method exhibiting extremely high sensitivity and selectivity is required to identify the telling compounds like mesothelin or CA 27-29 which could indicate the development of pancreatic, breast, or other types of cancer. Moreover, it is critical that such a detection method have a process for minimizing reports of false positives or negatives. Most diagnostic procedures today require immunological lab equipment and trained medical staff to perform the procedures. This is expensive and there is often a significant delay in obtaining results. For many applications, current techniques such as ELISA tests are infeasible for efficiently screening a large number of patients. The results of an ELISA test often take 2 to 4 days to become available and these tests are most commonly used to screen for only one target antigen. The solution to these problems is to make use of existing technology to develop a cheaper and more accurate minimally-invasive diagnostic test that improves and shortens the decision making process and requires minimal training or expertise. I am proposing the employment of piezoelectrically-based solidly mounted bulk acoustic wave (BAW) biosensors in an array configuration to address these issues.

1.2 Biosensors & Sensor Arrays

A sensor is typically considered to be a device or system that produces an output signal in response to some input. The output signal is a representation of the input quantity and can be used to predict the presence, absence, or concentration of specific targets in the environment. More specifically, a biosensor produces an output signal as a result of some sort of biochemical interaction with the device. Figure 1.1 illustrates a typical series of events for a biosensor. The process begins with the exposure of the biosensor to the sample. This is the sample that is being tested for the presence or absence of the molecular target(s) of interest. If the biosensor contains a biorecognition element, such as an antibody coating, then it will react with the antigen for which the antibodies are specific. After exposing the device to the sample, molecular recognition events will occur if the sample contains the target of interest. These are often called "binding-events" because of the physical interaction that takes place in an antibody-antigen interaction. As a result of this interaction, one or more properties of the sensor may be altered. The type of property that is altered by the interaction, whether it be a physical, electrical, or optical property of the sensor depends on the mode of operation. The response of the device to a change in one of these properties will manifest itself as a change in the output signal. After suitable signal processing and conditioning, this quantity can be used to provide information about the type and magnitude of binding events that occurred in the sensor.

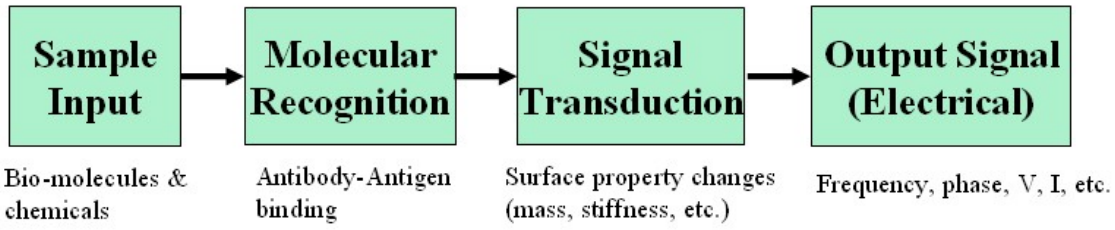

Figure 1.1 Biosensor detection: a typical sequence of events

This dissertation focuses mainly on the development of a particular kind of biosensor that uses elastic waves as a signal transduction mechanism. This type of device is referred to as an acoustic biosensor. The output signal of an acoustic biosensor is an oscillatory voltage that represents the frequency of resonance of the piezoelectric substrate that comprises the device. When the device is configured as a resonator, changes in operating frequency of the resonator can be a highly sensitive indicator of changes in the surface conditions. A resonator can be transformed into a biosensor through the immobilization of a bio- or chemi-specific layer at the surface of the device. Binding events at the biolayer cause perturbation of the boundary conditions which results in a change of the resonance condition (i.e. resonance frequency) - an easily monitored parameter. As a result, acoustic sensors are sensitive to mass-loading at the surface of the device. The added mass of proteins bound to the surface of the device can affect the resonant frequency. Devices that are sensitive to mass loading are often termed "gravimetric sensors". The general principle behind the operation of an acoustic biosensor is depicted in Figure 1.2.

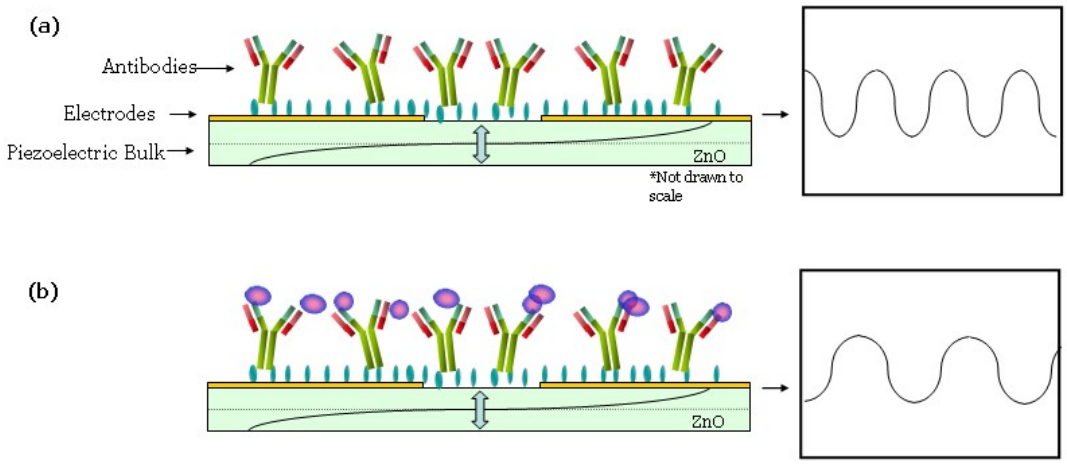

Figure 1.2 The principles of a general bulk acoustic wave sensor. (a) A resonator device coated with antibodies. The image to the right of the sensor drawing illustrates the output signal voltage at resonance f_0 when the device is in its normal state. (b) The resonator after target molecules have bound to the antibodies located at the surface. The output signal frequency is reduced which corresponds to a reduction in the operating frequency of the device. This "frequency shift" can be used to monitor molecular recognition events.

Acoustic devices are one type of sensor technology that is currently being explored, however there are many others. In optical sensors, the output voltage or current typically corresponds to the magnitude of fluorescence or optical density. Optical technologies have shown great potential and are useful for large-scale array testing. Cantilever-based biosensor systems often take advantage of piezoresistive materials. When the target molecule of interest binds to the cantilever causing it to bend, the resistivity of the material changes and the output current is altered. Surface plasmon resonance devices operate on the principal that light can excite surface plasmons at metal-dielectric boundaries only at certain angles of incidence. The excitation condition is dependent upon properties of the boundary. When biomolecules adsorb to the surface, the boundary conditions are changed, and the angle of maximum light absorption is shifted.

Sensors are typically characterized by four major quantities: Sensitivity, specificity, resolution, and detection limit. The sensitivity of a device refers to the measure of the output signal in response to an input quantity of given magnitude. The specificity of a device quantifies how well a sensor can distinguish between two different input quantities. In the case of biosensors used for medical diagnostics, high specificity is important for minimizing false positives. The resolution of a device refers to the minimum change in input quantity that manifests itself as a repeatable change in the output signal of the sensor. A device that has good resolution is desirable for most biosensors that are used for quantitative purposes. The detection limit is the minimum detectable input quantity that effects a change in the output signal above the inherent noise level of the sensor. This is tied to the resolution of the device. In biosensor experiments, this is typically referred to in units of g/ml or M.

There are many types of biosensors that are currently being developed to meet the needs of the scientific and medical communities. One of the most important aspects of a cancer biomarker sensor technology is that it be amenable to an array configuration. An array of biosensors allows for the flexibility of detecting multiple different targets simultaneously from a single sample, or for detecting the same target with multiple sensors. This type of multi-sensor testing adds a level of redundancy and statistical significance to the test that is important especially in diagnosis applications where false positives or false negatives can have disastrous effects. Optical sensors have been widely used in array formations, including microprotein arrays. However, these tests require expensive equipment to operate and are generally very expensive to perform at approximately $1,700 for one array (note: one array can look for 8,000 proteins at once).

Acoustic sensors possess the capability to be configured into multiple device arrays. There is theoretically no limit to the number of acoustic sensors that can be operated simultaneously, however the circuitry required to run and process many sensors becomes more difficult to design and implement on a very large scale.

It is believed that one method for developing highly predictive tests for individual cancer types will involve the evaluation of a combination of biomarkers from a patient sample. This would give rise to a protein level "signature" that may be more effective in predicting the onset of disease than a single non-specific biomarker. The goal for researchers however, is not just to make an array of biosensors to detect the expression of various biomarkers, but rather to do it well and do it inexpensively. This is the key. If a sensor is both inexpensive and highly sensitive, then it holds implications as a cancer screening technology for all people, regardless of their access to healthcare. The acoustic sensors discussed herein are fabricated using standard microelectronic fabrication techniques – similar to those used for the production of microprocessors which is easily streamlined and can be implemented for very high throughput.

1.3 Specific Aims

In this thesis, the development of a new type of bulk acoustic wave sensor that draws on many of the strengths of other existing acoustic sensor technologies is detailed. The pertinent aspects of the device including material choice, excitation configuration, and acoustic mode of operation as well its characterization as a biosensor are discussed. The specific hypothesis behind the proposed research is that *the lateral field excitation (LFE) of a ZnO-based thickness shear mode resonator can result in a sensor that is*

highly sensitive to mass loading. The specific aims have been designed to provide a comprehensive analysis of the bulk acoustic wave sensor from theory to application:

1. ***To develop the theoretical underpinnings of the acoustic wave propagation in ZnO, establish finite element models to corroborate the theoretical findings, and provide a proof-of-concept study for Thickness Shear Mode gravimetric biosensors.***

Theoretical proof that the lateral field excitation of *c*-axis oriented ZnO couples to the thickness shear mode (TSM) is important for validating the proposed sensor design. In order to do this, the crystal structure of the piezoelectric film was verified through XRD as a basis from which to build the models. The theoretical calculations were carried out by solving the piezoelectrically stiffened Christoffel equation to elucidate the acoustic modes that are excited through lateral excitation of a ZnO stack.

A ZnO finite element model was developed to investigate the electric field orientation and density for various electrode configurations. The models were used to visualize the electric field for assurance that the piezoelectric thin film is being laterally excited as well as the energy density and particle displacements for comparison with the theoretical calculations.

A proof of concept study was carried out using a Quartz Crystal Microbalance (QCM) device to investigate the application of thickness shear mode resonators to cancer biomarker detection in complex media. The verification of this commercially available TSM acoustic wave device helped to provide a firm foundation for the design of new gravimetric sensors with enhanced capabilities.

2. To design and fabricate arrays of multiple laterally excited TSM devices and fully characterize the electrical properties of the solidly mounted resonators.

The design phase of engineering new devices is the most time-consuming. Device performance may be predicted by theory, but fabricating working devices and translating theory into experimental results in the laboratory is another matter entirely. The devices were fabricated and tested for the purpose of characterization.

A program that calculates the stack layer thicknesses needed to produce a mirror that will approximate air for reflecting the acoustic wave was developed. The purpose of the acoustic mirror is to transform the apparent acoustic impedance of the silicon substrate into that of air to allow for reflection of the acoustic wave at the lower boundary.

Electrode designs for the sensor arrays were developed through finite element modeling and prototyping. The devices were fabricated and then tested for values of interest such as Q, and electromechanical coupling (K^2) as well as their ability to operate in liquids and the energy losses associated with that.

3. Investigate the optimal surface chemistry scheme for linking the biolayer to the ZnO device surface.

Developing acoustic wave device technology into a standardized biosensor platform requires that the biospecific coating be uniform and reproducible over a large number of devices. From one device to another, if the number of available molecular binding sites varies dramatically, sensor responses will be radically different given the same initial target concentration.

Crosslinking schemes involving organo-silane molecules such as Mercaptopropyltrimethoxysilane (MTS), (3-glycidoxypropyl)trimethoxysilane (GPS) as well as a phosphonic acid were compared for immobilizing antibodies to the surface of the ZnO. A heterobifunctional crosslinker was used to link the organosilane to the F_c region of the antibody. The surface density, uniformity, and repeatability of each cross-linking scheme was analyzed and compared through fluorescent microscopy and atomic force microscopy. The optimal scheme was chosen as the method to be used for subsequent biosensor tests in buffer and complex media.

4. To investigate the sensitivity of the acoustic immunosensors to potential diagnostic cancer biomarkers.

To perform biosensor experiments with these devices, resonator arrays were coated with antibodies using the preferred method as determined from the completion of aim 3. Initial tests were performed in buffer spiked with varying concentrations of the purified target antigen to develop a dose-response curve for the detection of mesothelin. The development of a dose response curve indicates the sensor's ability for detecting specific amounts of the target molecule when compared to reference sensors.

Following successful completion of the initial buffer tests, further tests were carried out in prostate cancer cell line conditioned medium to look for levels of PSA in fluids of prostate cancer cell lines. The results of the tests help to establish the operation of the devices in complex media for clinically relevant biomarker detection.

The work described in this thesis is one that, in my opinion, is truly interdisciplinary. The research is comprised of principles from the fields of physics,

electrical engineering, chemistry and biochemistry, and the final result is applied to solve problems in the field of medical oncology. It was my goal to pursue the work in each of these scientific areas with as much rigor as one who works solely in one of the fields would.

The next chapter introduces the various types of acoustic biosensors and the underlying physical principles behind their operation as well as the different ways each of these devices are currently being used as biosensors. Chapter 3 focuses on the QCM and developing finite element models to simulate the operation of the QCM. Also included are results from a study performed with QCM devices illustrating their effectiveness in detecting tumor markers in complex media which are detailed in [12]. Chapter 4 details the development of the ZnO-based LFE TSM acoustic resonators. The theoretical calculations are provided as well as finite element modeling results which supply supporting evidence for the excitation of the TSM mode in ZnO. Also included in Chapter 4 is data from the characterization of the experimentally realized devices [13-15]. Chapter 5 focuses on the functionalization of the TSM resonators through the exploration of immobilization techniques for linking antibodies to the ZnO surface. This is a critical step in the development of high precision biosensors. Sensor testing results are provided in Chapter 6 for the detection of mesothelin and PSA as well as characterization of the devices as acoustic biosensors. A look at a new type of acoustic sensor system is provided in Chapter 7. This sensor system is based on the traditional ladder-type filter structure in which each device that comprises the filter network can be configured as a sensor. Rather than looking at the frequency shift of an individual device, the system exploits changes in the frequency response of the overall structure which is determined by the individual sensors that comprise it. Circuit modeling and experimental

results are provided. Some general conclusions about the work presented and suggestions for future work are provided in Chapter 8.

CHAPTER 2

ACOUSTIC WAVE DEVICE BIOSENSORS

There are numerous types of acoustic waves and an even greater number of devices that utilize these waves for a particular purpose. Acoustic wave devices in general are extremely versatile. They can be found in a wide variety of applications in a wide variety of industries. This chapter is meant to provide the reader with a discussion of how acoustic devices operate and the way in which such devices can be utilized as biosensors. An explanation of piezoelectricity will first be offered, followed by a non-rigorous mathematical description of acoustic wave propagation in solid piezoelectric materials. Subsequently, a discussion is provided of the main types of acoustic wave devices and how they operate, followed by the different ways each of these devices are currently being used as biosensors. The chapter will close with a discussion comparing and contrasting the various acoustic wave devices and an explanation will be given for why thickness shear mode resonators have been chosen in this work.

2.1 Acoustic Device Background

The name acoustic wave sensor comes from the fact that these devices "sense" by responding to physical and chemical changes in the characteristics of the path over which an acoustic wave propagates. Waves that propagate through the substrate or at the surface of the substrate will undergo changes in velocity or amplitude as a result of characteristic changes in the acoustic wave path. The frequency and phase information of the acoustic

wave can be measured electrically to determine if a change from the initial operating characteristics in the wave has occurred. This is possible because of the property of piezoelectricity.

2.1.1 Piezoelectricity

Almost all acoustic wave devices use a piezoelectric material to transform electrical signals to mechanical stress and vice versa. Piezoelectricity, which is greek for "pressing electricity" is the direct link between electrical and mechanical phenomena. It occurs only in specific materials comprised of certain crystalline structures which do not possess inversion symmetry [16]. The piezoelectric effect couples mechanical properties (stress and strain) to the electrical properties of the crystal. The coupling of these properties occurs as a result of polarization. Polarization occurs when an electric field causes physical separation between positive and negative charges, which results in a dipole moment and a polarization vector, which is proportional to the electric field.

In piezoelectric crystals, the polarization vector can be created not only by an external electric field, but also by an external stress that deforms the crystal – causing a separation of charges. As a result, stress or strain in a piezoelectric crystal will produce an electrical response. Similarly, the inverse effect also takes place: the application of an electric field produces a mechanical response. This means that a wave propagating through the piezoelectric crystal can be excited using an external field produced by transducers. It is also possible to measure the electric field generated by a returning acoustic wave at the transducer. Because the substrate material is piezoelectric, the traveling acoustic wave exists as a mechanical deformation, but also "carries" with it a

potential distribution. It is possible to excite a wave electrically, and then determine whether its characteristics have been altered during the course of wave propagation. This is a fundamental concept behind acoustic wave biosensors.

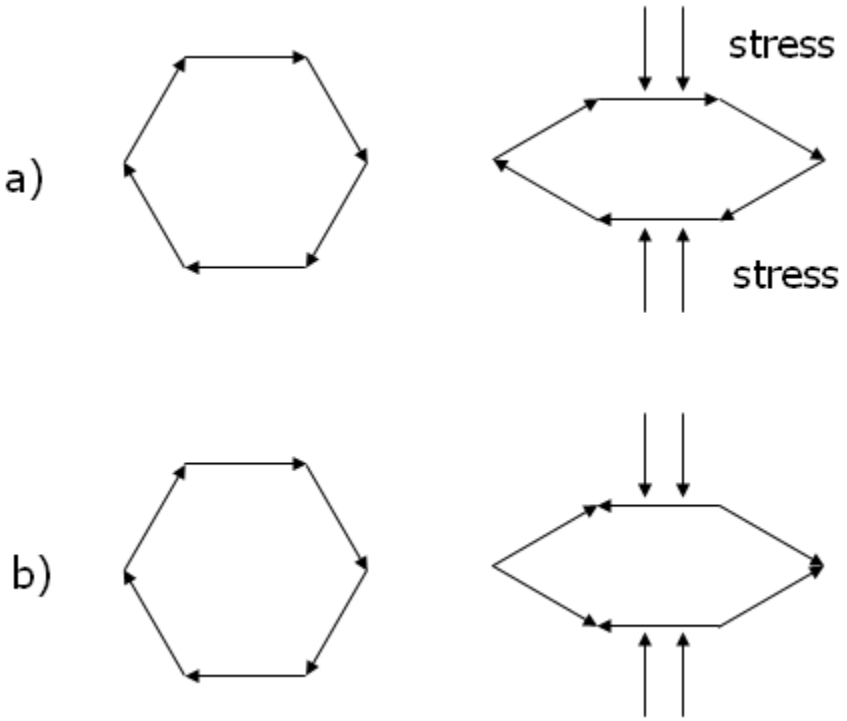

Figure 2.1 Coupling of a stress to electric polarization. The arrows represent individual dipole moments. Both a) and b) indicate hexagonal symmetry, but only in b) does the applied stress result in overall polarization (adapted from [17])

The coupling of an electric field to a mechanical strain depends on the symmetry class of the crystal. Typically, there are only specific external electric field orientations with respect to the crystal axes that will couple to a stress and vice versa. An applied symmetric force on one crystal symmetry class may not result in any polarization at all while the same symmetric forces on another crystal class will result in polarization. An example of this is shown in Figure 2.1. The figure illustrates two hexagonal crystal classes with the same external force applied. In Figure 2.1(a) the individual dipole

moments represented by the arrows all effectively cancel each other out leaving no net polarization of the material. In Figure 2.1(b) the same external stress causes the generation of non-symmetric dipoles, which leads to an overall polarization. The manner and direction in which stresses and e-fields couple together for various crystal classes is described by the piezoelectric coupling tensor. For the piezoelectric class, the inverse piezoelectric effect is defined through the tensor relation:

$$\mathbf{S} = \mathbf{d} : \mathbf{E} \tag{2.1}$$

Where S is the strain matrix, d is a matrix called the piezoelectric *strain* tensor, and E is the electric field vector. This can be transformed into an equation relating the stress and the electric field:

$$\mathbf{T} = \mathbf{e} : \mathbf{E} \tag{2.2}$$

where e is defined as the material stiffness multiplied by the piezoelectric *strain* tensor, d, and is named the piezoelectric *stress* tensor. T is defined as the stress vector. Of additional value is the introduction of D, the electric displacement. The displacement vector is related to E through the relation:

$$\mathbf{D} = \boldsymbol{\varepsilon}_r : \mathbf{E} \tag{2.3}$$

Where ε_r is the relative permittivity of the material multiplied by ε_0 - the permittivity of free space. These equations will be of more use in the next section when they will be integrated into the equations that describe acoustic wave propagation.

2.1.2 Acoustic Device Theory

The purpose of this section is to provide the reader with a fundamental understanding of acoustic wave propagation and the equations involved. The equations discussed here will be used later for deriving more directly useful equations, but they provide fundamental understanding of the forces involved in acoustic wave propagation and help in the development of intuition for understanding acoustic waves. While in-depth derivations of this theory can be found in many sources [17-19], a less rigorous approach will be taken here so that the information presented is useful to a wider audience.

Before a discussion of acoustic waves can take place, some important terms must first be defined. Stress refers to a force *F* applied per unit area *A* of a solid. Typically mechanical stress is denoted by the letter *T* and has units of N/m^2. To completely represent the state of stress at each point in a solid requires the use of a stress tensor. Each element of the tensor, T_{ij}, represents the i^{th} direction component of the force acting on the j^{th} face of an infinitesimal volume (i and j = x,y,z).

The particle displacement, in three dimensions can be represented by a displacement vector *u(x,y,z,t)*. A plane wave in a solid will produce harmonically varying particle displacements in the direction of the wave propagation. This can be described by a harmonic equation

$$u(x,y,z,t) = (u_x x + u_y y + u_z z)e^{(\omega t - ki)} \tag{2.4}$$

where *i* is the direction of wave propagation and ω is the angular frequency of the wave. In acoustic wave propagation, simple translation is not of interest. Rather, local

deformations such as local rotations or changes in the inter-particle distance are of primary importance.

Strain, denoted by S, is the gradient (spatial rate of change) of the particle displacement due to an applied stress and is dimensionless. It can be calculated for any direction in the solid and is given by the equation:

$$S_{ij} = \frac{1}{2}\left(\frac{\partial u_i}{\partial x_j} + \frac{\partial u_j}{\partial x_i} \right) = S_{ji} \tag{2.5}$$

$S_{ij} = S_{ji}$ are components of a 6x6 strain tensor that relates the rate of change of particle displacement in the i^{th} direction to the along the j^{th} axis. For example, S_{xx} represents the gradient of x displacement along the x-axis. This term would be nonzero in the case of a material fixed at one end being stretched along the x-axis. Thus, S_{22} and S_{33} represent strains in the y and z directions, respectively. The terms S_{ij} where $i \neq j$ are called shear strains. Nonzero shear strain represents, in a physical sense, an angular difference between elements initially in the i^{th} and j^{th} directions. Both stresses and strains in an elastic solid can be either compressive, tensile, or shear. A compressive stress tends to push particles together, while a tensile stress tends to pull them apart. These stresses form the class of longitudinal stresses [17].

An elastic medium behaves as a distributed mass-spring system. The perturbation of a single particle will propagate throughout the system due to elastic coupling between adjacent particles. Much like the high school physics system of a harmonically oscillating mass on a spring, the particles in an elastic medium will oscillate under perturbation. Thus, in an elastic solid, there exists a linear relation between the internal stresses and the deformation. In one dimension, this is known as Hooke's law, which relates the

deformation of an elastic system to the force applied. It is possible to generalize this equation to three dimensions for non-piezoelectric solids:

$$T_{ij} = \sum_{k,l=1}^{3} c_{ijkl} S_{kl} \tag{2.6}$$

In which the individual values c_{ijkl} that comprise the larger matrix of values are called the stiffness coefficients. The large matrix of all of these values is called the stiffness tensor. The stiffness coefficients can be thought of as "microscopic spring constants" that characterize the elastic behavior of a solid. At this point, it is useful to introduce a notation used to simplify the tensor notation. Since the stress and strain tensors are symmetric (ie. $T_{ij} = T_{ji}$), at most six of the nine elements of the tensor are unique. Therefore, it is possible to reduce the index ij to a single index usually denoted with a capital letter. Table 2.1 clarifies how the notation relates to the expanded subscripts.

Table 2.1 Reduced Index Notation

I, J	i, j
1	xx (11)
2	yy (22)
3	zz (33)
4	yz (23), zy (32)
5	xz (13), zx (31)
6	xy (12), yx (21)

Use of this notation reduces the stress and stiffness matrices to 1x6 column vectors and the stiffness tensor from an 81-value matrix to a 6 x 6 matrix. This reduced notation is often referred to as "Einstein notation". Equation 2.6 can now be written in reduced form:

$$T_I = \sum_{J=1}^{6} c_{IJ} S_J \tag{2.7}$$

This equation is called the *Reduced Elastic Constitutive Relation* and is a three-dimensional form of Hooke's law. It relates the stress and strain in three-dimensions for a non-piezoelectric substrate. However, the sensors described here are piezoelectric devices, and we are interested in how stress and strain are related for piezoelectric materials. To develop a relationship that incorporates the piezoelectric effect, we can combine Eqs. 2.2 with 2.7 to get an equation in reduced form:

$$T_I = c_{IJ}^{E} S_J - e_{Ij} E_j \tag{2.8}$$

This equation describes stress at a particular point as a function of the material parameters as well as strain at that location and the electric field. In this equation, summation over the repeated indices is assumed. The values of the stiffness tensor are measured at constant electric field. The mechanical constants must be measured from a grounded crystal to prevent charge buildup, which can significantly alter the results [17]. From this equation, another equation can be derived which relates the electrical displacement D, to E and S from Equation 2.3:

$$D_i = \varepsilon_{ij}^{S} E_j + e_{iJ} S_J \tag{2.9}$$

where ε_{ij}^{S} is the permittivity which must be calculated from values measured at constant stress [17]. Together, Equations 2.8 and 2.9 are named the *Piezoelectric Constitutive Relations*. These equations are useful for making acoustic wave calculations because the

strain is related to the particle displacement by Eq. 2.5. This relationship can be written in a simpler form using a differential operator:

$$\mathrm{S} = \begin{bmatrix} S_1 \\ S_2 \\ S_3 \\ S_4 \\ S_5 \\ S_6 \end{bmatrix} = \begin{bmatrix} \frac{\partial}{\partial x} & 0 & 0 \\ 0 & \frac{\partial}{\partial y} & 0 \\ 0 & 0 & \frac{\partial}{\partial z} \\ 0 & \frac{\partial}{\partial z} & \frac{\partial}{\partial y} \\ \frac{\partial}{\partial z} & 0 & \frac{\partial}{\partial x} \\ \frac{\partial}{\partial y} & \frac{\partial}{\partial x} & 0 \end{bmatrix} \begin{bmatrix} u_x \\ u_y \\ u_z \end{bmatrix} \tag{2.10}$$

where $S_4 = 2S_{yz} = 2S_{zy}$, $S_5 = 2S_{xz} = 2S_{zx}$, $S_6 = 2S_{xy} = 2S_{yx}$. This can be written in shorthand notation as

$$\mathbf{S} = \nabla_s \mathbf{u} \tag{2.11}$$

where the gradient matrix operator ∇_s can be written as ∇_{Ij} where I = 1 to 6 for the six rows and j = 1 to 3 for three columns.

Another useful equation that can be derived from the piezoelectric constitutive relations is the wave equation for piezoelectric substrates. We can describe the electric field as the gradient of a scalar potential:

$$\mathbf{E} = -\nabla \phi \tag{2.12}$$

Newton's law in three dimensions can be written as:

$$\nabla \cdot \mathbf{T} = \rho \frac{\partial^2 \mathbf{u}}{\partial t^2} \tag{2.13}$$

Where T is the stress vector, ρ is the density of the piezoelectric substrate and u is the particle displacement. In similar fashion to the gradient matrix operator in Eq. 2.11, the

divergence of stress in Eq. 2.13 can be expressed as the product of a divergence matrix operator and stress matrix. The divergence matrix operator is a 3 x 6 matrix and often written using shorthand notation ∇_{iJ}:

$$\begin{bmatrix} \frac{\partial}{\partial x} & 0 & 0 & 0 & \frac{\partial}{\partial z} & \frac{\partial}{\partial y} \\ 0 & \frac{\partial}{\partial y} & 0 & \frac{\partial}{\partial z} & 0 & \frac{\partial}{\partial x} \\ 0 & 0 & \frac{\partial}{\partial z} & \frac{\partial}{\partial y} & \frac{\partial}{\partial x} & 0 \end{bmatrix} \tag{2.14}$$

This matrix is simply the transpose of the gradient matrix operator matrix. Substituting Eqs. 2.11 and 2.12 and applying Eq. 2.13 into Eq. 2.8 results in the wave equation in piezoelectric media:

$$\nabla \cdot \mathbf{c}^{\mathrm{E}} : \nabla_s \mathbf{u} + \nabla \cdot \boldsymbol{e} : \nabla \phi = \rho \frac{\partial^2 \mathbf{u}}{\partial t^2} \tag{2.15}$$

This equation contains a term involving the electric potential ϕ. The term may be considered a source term responsible for the generation of an acoustic wave by a time-varying electrical potential [19]. As a result of the piezoelectric effect, an electric potential can generate particle displacement and therefore an acoustic wave, but the particle displacements accompanying the acoustic wave also generate an electric potential. Consequently, electrodes can be used to generate an acoustic wave, and they can also be used to measure electric properties of the returning acoustic wave such as the frequency and phase. This is a fundamental result of the equations discussed in this section and forms the theoretical groundwork behind the operation of the acoustic wave devices discussed elsewhere in this thesis.

2.2 Types of Acoustic Wave Devices & Sensors

There are many different types of acoustic wave devices and a wide variety of applications for which the devices are used. The key to this wealth of applications is twofold. First, there are many types of acoustic waves that can propagate in elastic media. Each has specific attributes that can be employed to produce considerably different devices. The second key lies in the materials used for making acoustic wave devices. Device performance relies heavily on the material properties of the crystalline substrate. There is wide variation in crystalline material properties that arises mostly from a combination of the atoms that make up the crystal, the crystal structure, and the uniformity of the crystal with respect to defects and grain boundaries. Properties such as density, material Q, electromechanical coupling, piezoelectricity, and ferroelectricity among others arise from the atomic and structural makeup of each unique crystalline material. In this thesis, the devices are designed using Zinc Oxide primarily because it has specific properties that are useful for the type of sensors we wish to design. As will be shown in Chapter 4, the hexagonal crystal structure of the ZnO can support a thickness shear mode resonance through lateral field excitation. Additionally, it can be deposited through RF sputtering techniques to form highly oriented polycrystalline thin-films. Resonators made from these thin-films are often referred to as film bulk acoustic resonators or FBARs. Unlike some other piezoelectric materials such as Quartz and $LiNbO_3$ which are difficult to deposit in crystalline thin-films, ZnO can be deposited onto a Si wafer to form solidly mounted devices. These solidly mounted devices are structurally more robust than free-standing quartz crystal devices. Additionally, they are less expensive to produce than quartz devices and can be integrated with other ICs.

2.2.1 Bulk Acoustic Wave Devices

Bulk acoustic wave (BAW) devices are characterized by an acoustic wave that propagates through the bulk material. They are widely used in radio frequency (RF) filters for military applications and consumer electronics. One of the advantages of using BAW devices in RF applications is their capacity for operating at frequencies well above 1.5 GHz. Similarly, for sensor applications, BAW devices can be fabricated at frequencies well into the GHz range using standard microelectronic fabrication procedures. This is an important point because it has been shown that the sensitivity of a bulk sensor is related to the square of the operating frequency. Thus, as the operating frequency increases, the ability to detect smaller and smaller mass changes improves.

There are two major types of bulk acoustic waves that can be excited in a piezoelectric substrate. The most important for sensing applications is called the thickness shear mode (TSM) which is so named because the acoustic wave propagates through the thickness of the piezoelectric film while the particle displacement is perpendicular to the propagation direction vector. This is a type of transverse wave. The other main type of bulk acoustic wave is the longitudinal wave. The longitudinal wave is characterized by particle displacement in the same direction as the propagating wave. In a thin-film resonator, the wave propagates through the thickness of the thin film and the particle displacement is similarly normal to the surface. The propagation of a sound wave in air is an example of a longitudinal wave. The two main types of bulk waves are visually represented in Figure 2.2.

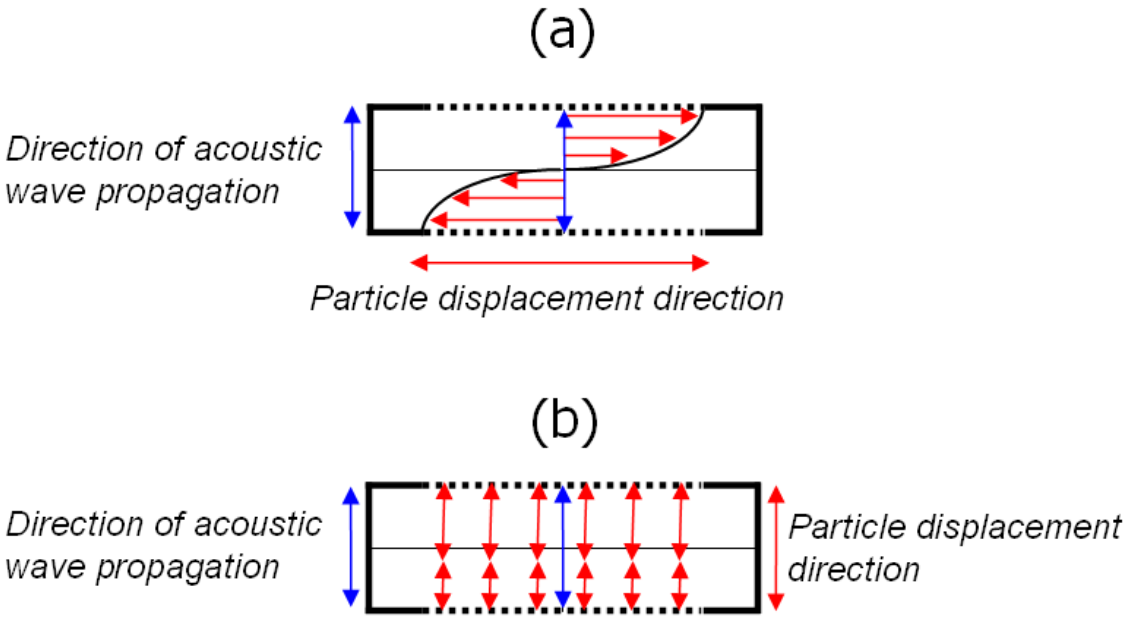

Figure 2.2 The two main types of bulk acoustic waves. a) The thickness shear mode illustrating particle displacement normal to the direction of wave propagation through the thickness of the crystal and b) the longitudinal bulk mode illustrating particle displacement parallel to wave propagation

Bulk acoustic wave device biosensors operate in a fairly simple manner. Typically, the device is comprised of a piezoelectric material with electrodes positioned either in the lateral field excitation or thickness excitation configuration. The lateral field excitation (LFE) electrode configuration involves two plane-parallel electrodes which can generate a laterally oriented electric field between them. The thickness excitation (TE) electrode configuration consists of electrodes on either side of the piezoelectric bulk which generate an electric field vector through the thickness of the bulk. The electrodes are used to excite and maintain an acoustic resonance. Positioned on one surface of the device is the sensing layer. This layer could be a chemical sensing layer or biological layer comprised of antibodies. During a sensor experiment, this surface is exposed to the sample under test and if the target of interest is present in the sample, it will react with

the sensing layer. The interaction will produce a mechanical change in the sensing layer through the addition or subtraction of mass, or some other mechanism. The mechanical change at this surface will affect the acoustic resonance causing it to shift in frequency. By monitoring the resonance frequency as the sensor is exposed to the sample under test, a correlation between the frequency shift from the initial frequency (f_o) and the amount of mass bound to the surface can be made.

For liquid sensing applications, the longitudinal particle displacement is typically considered to be undesirable. Normally when a longitudinal-mode resonator is operated in air, the acoustic impedance mismatch is very favorable and the acoustic energy incident on the boundary is reflected back into the piezoelectric substrate. This is a requirement for sustaining a resonant mode. However, when water or another aqueous fluid comprises the material at the upper boundary of the device, the impedance mismatch is no longer favorable. Water can support a longitudinal mode, and therefore the acoustic energy will be lost into the fluid. This results in either a complete loss of resonance, or a significantly reduced signal. Some researchers have still investigated the use of longitudinal mode ZnO FBARs as liquid sensors despite the large reduction in device quality (Q). For example, Zhang *et al.* developed a sensor capable of detecting ionic concentration changes for *in vitro* studies of neuronal activity [20]. Despite a reported 95% reduction in Q from 210 to 12 for operation in liquids as compared to air, they reported excellent sensitivity to mass loading. In another study, the same group reported the use of the 2nd harmonic for sensing purposes because it exhibited a higher quality factor when exposed to a liquid environment [21]. They reported a detection limit of 10^{-8} g/cm^2 which corresponds to 5 ppm of mass shift at the sensor surface. Another

example of a longitudinal ZnO FBAR biosensor was offered by Gabl et al. [22]. They illustrated the use of a solidly mounted resonator configuration for the detection of Streptavidin in solution. An in-air Q of 400 is cited, but they fail to mention the liquid loaded Q. Based on these results, it seems plausible that a longitudinal mode resonator could be used for high-sensitivity mass detection. The advantages of this type of sensor lie in its small size and the fact that it can be produced using standard IC techniques. However, in our experience a large reduction in device Q can reduce the detection limit and resolution of a device.

The more common type of bulk acoustic device used in liquid sensing applications is the thickness shear mode resonator. The advantage of TSM resonators lies in the particle motion with respect to the wave propagation direction. With longitudinal resonators, the particle displacement is normal to the sensor surface, whereas with TSM devices, the particle displacement is parallel to the surface. This particle motion results in reduced damping by an adjacent liquid layer since water does not support a shear mode. For detection purposes, this is important because a strong resonance is required for high sensitivity and good mass resolution. When a resonator is damped, much of the energy is lost to the surrounding medium and the sensitivity and resolution are reduced.

The quartz crystal microbalance (QCM) is by far the most common example of a TSM resonator used for sensor applications. The terms TSM and QCM are often (albeit incorrectly) used interchangeably. The reason for this is simply because there are very few reports in the literature of the TSM mode in other crystal types and even fewer reports of TSM devices other than the QCM being utilized for any practical purpose - let alone sensor applications. QCMs have been in use for nearly 50 years in a variety of

applications and are commonly used to monitor the thickness of metallic films deposited in vacuum deposition systems. In the 70s, it was discovered that the thickness shear mode was ideal for liquid sensing applications, and has since been used for a variety of liquid phase chemical and biological sensors [23-30]. However, there are many drawbacks to using QCMs as biological sensors which will be discussed in Chapter 4. For this reason, the desire to develop new TSM devices that improve upon standard QCM technology has grown recently. One of the main areas of TSM research involves using quartz plates similar to the QCM but with a LFE electrode configuration instead of the typical TE configuration. Work from the labs of da Cunha and Vetelino describes the sensitivity of these LFE quartz crystals to binding interactions of biological molecules. In one paper, they discuss the development of a sensor in which they immobilize biotin to the quartz surface and measure the sensor response to the binding of streptavidin [31]. They claim larger frequency shifts, and therefore higher sensitivity than a typical QCM with the thickness excitation electrode configuration.

In another TSM study, Weber *et al.*, claim to have implemented a ZnO-based FBAR operating in the thickness-shear mode for biosensor purposes [32]. In the paper, they utilize ZnO oriented at 17° from the vertical axis and a TE electrode configuration as the substrate for an avidin/BSA/anti-avidin sensor. They claim to have developed a TSM resonator with twice the sensitivity of the standard QCM. However, the paper is lacking in the sense that it supplies no true data on verification that the mode is actually a TSM as opposed to some sort of electromagnetic resonance. The electromagnetic resonance matches up much more accurately to their reported resonance frequency than the TSM or longitudinal mode.

Based on the current literature pertaining to TSM and BAW sensors, we feel that there is great potential to improve upon prior work in developing a sensor that is highly sensitive, amenable to an array configuration, and easy to manufacture.

2.2.2 Surface Acoustic Wave Devices

Perhaps the most widely studied class of acoustic sensor is the Surface Acoustic Wave (SAW) device. SAW devices are defined simply as those in which the acoustic wave is generated and propagates at or near the surface of the device. There are many combinations of electrode configurations and piezoelectric materials that have been used for sensor development. In the most general case, the surface acoustic wave is generated by electrodes located at the surface of the device in a configuration known as interdigitated transducers (IDTs). A rough schematic for a SAW device is shown in Figure 2.3.

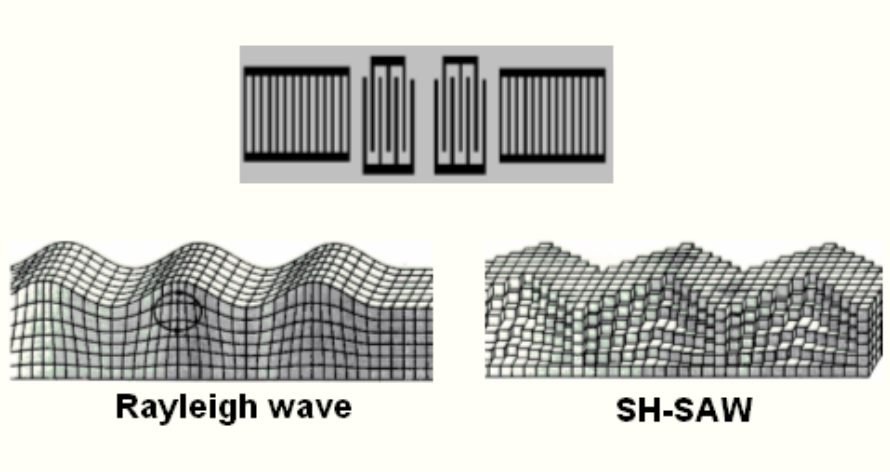

Figure 2.3 A two-port SAW resonator is shown (top) which is comprised of two IDTs in the center with two sets of reflector strips on either side of the IDTs. The IDTs generate the acoustic waves while the reflector strips reflect the acoustic energy back into the center of the device to trap as much acoustic energy as possible. Two types of SAW waves are shown (bottom). Image Courtesy of Dr. Sang-Hun Lee

An IDT is made up of pairs of "fingers" that generate the electric field necessary to excite a wave in the piezoelectric material. IDT parameters such as the number of finger pairs, the distance between fingers, the shape of the fingers, the apodization, etc. can be varied to produce the desired device response in the desired frequency range. In fact, by changing the IDT geometries and locations, a multitude of devices can be obtained – including those with signal processing functions operating with nonlinear effects eg. correlators/convolvers. The amount of research carried out for the characterization of SAW devices for complex signal processing functions and other applications is vast. A discussion of the body of work surrounding the history of SAW device research is certainly not within the scope of this dissertation. However, the author would recommend to any readers interested in a more in-depth discussion of SAWs especially for device operation principles to consult Dr. Colin Campbell's book which is considered by many to be an authority on the subject [33]. For our purposes, it is sufficient to discuss a few of the major types of acoustic wave devices used in biosensor applications.

First, it should be mentioned that there are many types of surface waves that can be excited with surface mounted IDTs. The shear-horizontal surface acoustic wave (SH-SAW) also called the surface transverse wave (STW), Love wave, leaky saw, and rayleigh waves are the most commonly used surface waves in biosensor applications.

The rayleigh wave is a wave that is somewhat similar to an ocean wave in that the particle motion follows an elliptical path. Because the particles have a component of motion in the vertical direction, when used in liquid sensing applications they suffer many of the same effects as longitudinal BAW devices because the acoustic energy is

dampened by the fluid. For this reason, they are rarely used as liquid-phase sensors. However, they have been shown to be highly sensitive for vapor-phase molecular detection of cocaine [34].

SH-SAW devices and Love wave devices are by far the most common type of SAW biosensor. Although there are fundamental differences between the wave types, the resulting sensor operates under the same principles. The particle displacement for both types of waves is in the plane of the piezoelectric crystal and the acoustic energy is focused at the surface of the devices. Changes in mechanical properties at the surface will alter the propagating wave. The shear mode of the SH-SAW device, like the TSM, is a mode in which the particle displacement is transverse to the propagation direction. The Love wave is essentially a surface skimming bulk wave that is converted into a waveguide mode in a layer that is deposited on the surface of the piezoelectric material. In order for the shear wave to be converted into the waveguide mode, the acoustic velocity in the waveguide layer must be lower than the acoustic velocity in the substrate. These waves may have horizontally polarized shear particle displacements depending on the material and crystal orientation of the piezoelectric substrate. There are numerous examples in the literature of both SH-SAW devices and Love-mode devices being used in biosensor applications. Recently, Berkenpas *et al.*, illustrated the detection of E-coli in PBS buffer using pure SH-SAW devices fabricated on Langasite [35]. In another study, a SH-SAW sensor was developed using 36° Y-rotated X-cut lithium tantalate for detecting phospholipid vesicles [36]. The waveguide layer required in Love-mode devices is something that when exploited properly, can be used to improve the sensor response to biological molecules. Since the wave propagates through this layer, most of the acoustic

energy is contained within it. Therefore, the regions of highest sensitivity are located nearest to the waveguide. If the capture molecules are positioned such that they are contained in, or directly adjacent to the waveguide, maximum sensitivity can be achieved. The waveguide layer can also be used as an insulator to protect the electrodes at the surface of the device from being affected by varying ionic concentrations in solution. In 2004, Branch and Brozik published a study comparing the use of polyimide and polystyrene as two different waveguide materials in a Love mode lithium tantalate sensor for bacillus thuringiensis [37]. They found that polyimide provided a detection limit of 1.0-2.0 ng/cm^2 in the liquid phase while polystyrene provided a detection limit of 2 ng/cm^2. In another study, Gronewold *et al.* employed aptamers as the molecular capture molecule for detecting human thrombin in PBS buffer using a Love-mode sensor with detection limits in the range of femtomole/cm^2 [38].

In addition to the numerous liquid-phase studies reported in the literature, there exist rports of vapor-phase sensing as well. Stubbs *et al.* report the use of antibody coated SAW devices in the vapor-phase. Through fluorescent molecule studies, they have shown that the antibody activity is maintained in air [39]. Though not the topic of discussion here, SAW devices have perhaps been studied in the greatest capacity as chemical-vapor sensors. Chemically selective coatings are often used as the waveguide layer, which are sensitive to reaction with specific chemicals of interest. If present in the environment, the chemical will react with the coating of the SAW device which results in perturbation of the device.

2.2.3 Other Acoustic Wave Device Sensors

While SAW and BAW devices are the most common types of acoustic devices used for chemical and biological sensing, there are other types of devices that have found use in these areas. Namely, acoustic plate mode (APM), flexural plate wave (FPW), and lamb wave devices. APM devices are very similar to SAW delay line devices in that the input and output IDTs are located on the surface of the device. However the main difference is that while a SAW device is built on a piezoelectric substrate that can be modeled to look like an infinite half-space, an APM device uses a thin plate (or membrane) which serves as an acoustic waveguide to confine the acoustic energy between the upper and lower surfaces of the plate. This is in contrast to a standard SAW device where nearly all of the acoustic energy is concentrated within one wavelength of the surface. The APM can be likened to a hybrid between a thickness shear mode BAW device and a SH-SAW delay line. Much like the TSM, the particle displacement is shear to the propagation vector and the upper and lower surfaces have displacement maxima. However in the APM, the propagation vector is not through the thickness of the plate, rather it is down the length of the waveguide. Physical perturbations at the upper or lower boundaries of the plate will modify the acoustic mode. There is currently not a large amount of published literature on the use of APM devices as biosensors. However, the first studies came from Andle *et al.* from the University of Maine who showed that the APM in $LiNbO_3$ is sensitive to both antigen-antibody interactions, and DNA hybridization [40-42]. More recently, the detection limit for an APM immunosensor was reported to be approximately 0.5 μg/ml from experiments performed using an aminosilane surface chemistry on gold [43]. Our own work with aminosilane surface

treatments could explain why such a low sensitivity was obtained. Rather than the lack of sensitivity being inherent to the APM device, we found the surface chemistry utilized in the study to be extremely inconsistent in its ability to bind antibodies to the surface of the device.

Flexural plate wave devices operate through the excitation and propagation of a wave through a thin plate similar to APM devices. This plate is typically a membrane of some sort that is freed from the surrounding substrate through a chemical etching step in the fabrication. The wave is generated at the surface of the device using IDTs but is transferred into the plate and propagates through the plate in similar fashion to a SAW delay line where it is converted back into an electrical signal at the output IDT. The main difference between a FPW device and an APM device lies in the manner in which the acoustic mode propagates through the plate. In FPW devices, elements of the plate undergo flexure as the wave propagates. One type of wave that propagates in an FPW device is called the Lamb wave. There are two main types of Lamb waves - symmetric and asymmetric. These waves are characterized by areas of compression and rarefaction within the plate. The shape of the plate in an asymmetric Lamb wave mode (Figure 2.4 (a)) can be likened to a flag waving in the wind – where the entire plate is physically rippling in a periodic manner. In the asymmetric case, adjacent particles at the top and bottom surfaces move with the same displacement vector in unison.

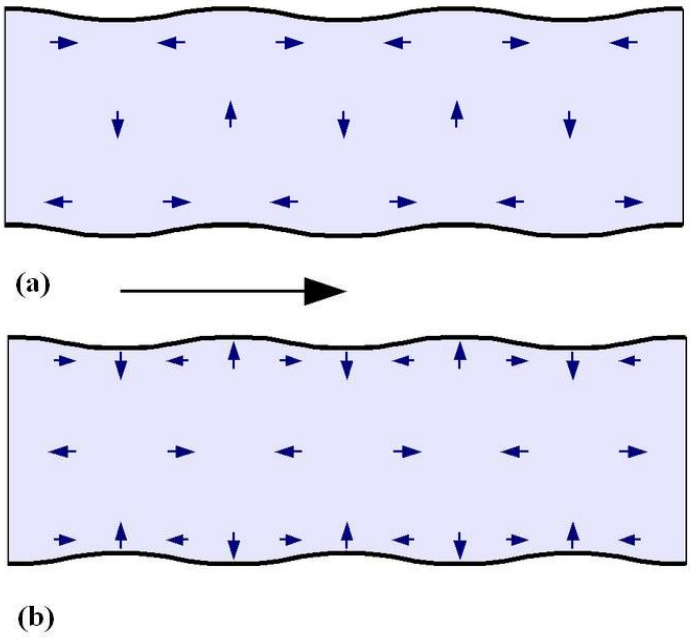

Figure 2.4 An illustration of Lamb waves in a thin acoustic plate. (a) The asymmetric mode and (b) the symmetric mode. The small arrows indicate the displacement vector fields while the large arrow corresponds to the direction of wave propagation. Image courtesy of Michael Schmid (GFDL)

In the symmetric mode, which is illustrated in Figure 2.4 (b), the adjacent particle displacement is 180º out of phase which results in alternating areas of compression and rarefaction. Given that the particulate motion possesses a surface-normal component, it would seem that the acoustic response of such a device would be degraded when operated in liquid. In fact, if the phase velocity in the acoustic plate is below the velocity of sound in water, the acoustic energy is not lost into the surrounding medium. Recently published studies have reported on the incorporation of FPW devices into 8-device arrays on silicon chips for the detection of proteins and micro-organisms [44]. Another recent study detailed the development of an FPW sensor for monitoring adverse interactions between potential anti-SARS drugs and the hACE2 protein which these types of drugs are known to often interfere with [45].

2.2.4 Comparison of Acoustic Device Types for Biosensor Applications

The various types of acoustic devices discussed in the preceding pages each have their own pros and cons. As with most technologies, the people that work with each type of device tend to think that theirs is superior. Until one type of sensor device is commercially available and widely used in hospitals and doctor's offices for diagnosis, detection, etc. then no device has truly proven to be better than the others for anything more than simple academic gains.

It is a widely accepted idea that higher device operating frequency leads to a higher gravimetric sensitivity in acoustic sensors [19]. This, however, is usually tempered by the idea that higher frequency comes at the expense of more costly electronics. The main advantage of using thickness shear mode FBARs over any other acoustic device is that they can be fabricated to operate at extremely high frequencies – well into the GHz range without increasing the cost of fabrication. Therefore, it is possible to fabricate devices with theoretically higher sensitivity than lower frequency devices for the same cost. Further, advances in RF electronics have made possible low cost RF electronics such as 8-way RF switches in an integrated circuit configuration. With the advent of products like these, the cost of developing high frequency biosensor systems has been reduced dramatically.

The frequency of an FBAR device is dictated by the thickness of the piezoelectric film. In SAW devices, the center frequency of operation is determined by the spacing of the IDT finger pairs. The finger pair spacing must be reduced in order to increase the frequency. For devices operating with a center frequency above 300-500 MHz, the required finger pair spacing approaches the limit of most optical lithography systems

available in the university setting. In order to repeatably fabricate line widths thin enough for the device to operate in the GHz frequency range, e-beam lithography must be used. Figure 2.5 shows a picture of an RFID SAW device designed in collaboration with Wafa Soofi at the 2.4 GHz frequency range that was fabricated using the e-beam lithography system in the Microeletronics Research Center at Georgia Tech.

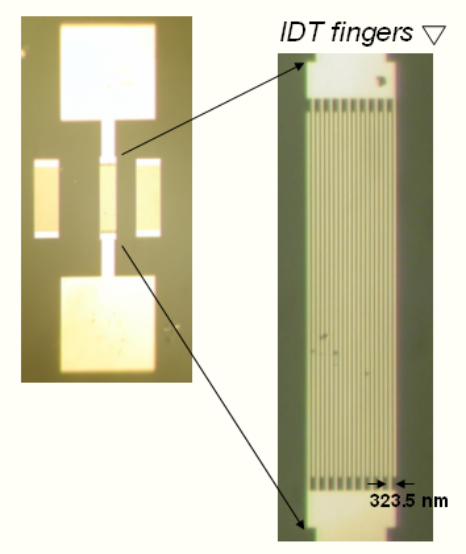

Figure 2.5 An image of a SAW device operating in the 2.4 GHz range. The device was fabricated in our lab using e-beam lithography to pattern the 325.5 nm line widths

The current problem with using e-beam lithography for mass production is that it is very expensive, as well as time-consuming. The e-beam uses a rastering method to expose the photoresist. This means that the beam must "draw" the pattern through every point in the design. For large-scale production, this is very expensive given that 1 hour of time on the current e-beam tool costs approx. $200.

FPW devices have shown promise in the field of acoustic biosensors. However, the main drawback to these devices lies in their robustness and the difficulty in fabricating them. Because they are comprised of very thin membranes of piezoelectric

material, they are not nearly as robust as a solidly mounted FBAR. Any shock to the device or extreme pressure can rupture the membrane, leaving the device unusable.

Solidly Mounted FBARs offer a promising alternative to other types of acoustic biosensors. FBARs can be fabricated to operate at high frequencies without increasing the cost or difficulty of fabrication, they can be easily fabricated in array configurations, they are extremely physically robust sensors, and they can be operated in the liquid-phase which is very important for biosensor applications. Additionally, their use as biosensors is relatively un-explored in the literature. For these reasons, we have chosen the FBAR configuration as a platform from which to build a new type of acoustic biosensor.

CHAPTER 3

QCM MODELING & LIQUID PHASE DETECTION

The QCM is a device that has found use in a variety of industries and applications. In Chapter 2, brief introductions to the thickness shear mode and the QCM were provided. In this chapter, the QCM is discussed in greater depth along with the theory behind using these devices as mass sensors, or more specifically, as biosensors. The development of a finite element model of the QCM is discussed along with some of the practical nuances to the development of such a model such as piezoelectric tensor values and definition of the AT-cut quartz plate. The model was used for verifying the finite element modeling process so that TSM devices fabricated from different materials could be similarly modeled and the results obtained could be trusted. The devices were utilized as biosensors for the detection of mesothelin in pancreatic cancer cell line supernatant to demonstrate the usefulness of TSM-biosensors in complex media. Finally, a discussion outlining the shortcomings of the QCM and the need for new sensor technology is provided.

3.1 Background & Theory

Before device design can begin, a thorough treatment of the device theory must be carried out to give direction for the research and warrant further progress in the design of acoustic devices. The process for this research begins at two separate points. We must prove that, in general, a TSM acoustic wave device can operate as a highly sensitive and

specific biosensor in the liquid-phase for detection of cancer marker proteins. The second point is to develop models based upon fundamental physical equations to predict the behavior of a device and aid in the design process. A widely available and generally accepted TSM technology is that of the QCM. Sensor experiments employing QCMs for the detection of a clinically relevant biomarker will serve to prove that TSM devices can be operated as biosensors even in complex media such as supernatant. It will also help to provide confidence that we are able to adequately perform the protocols needed to create a valid biosensor for operation in complex media.

Quartz Crystal Microbalances are a type of acoustic wave device that have been in use for nearly 50 years and are most commonly used to monitor the thickness of metallic films deposited in vacuum deposition systems. These piezoelectric devices were first thoroughly investigated in 1880 [46], but were not utilized as immunosensors until 1972 [47]. In the past decade, QCM-based immunosensors have drawn attention because of their ability to detect slight mass changes due to molecular binding [48-51].

It has been established through the work of numerous investigators that the sensitivity of piezoelectric biosensors is directly proportional to the square of the unperturbed operating frequency of the base resonator. Thereby, the sensitivity of the sensor increases with increasing resonant frequency. The initial demonstration of this was presented by Sauerbrey [52] in 1959 with an equation that relates a frequency change to a change in the mass density of the loading layer

$$\Delta f = \frac{-2 f_o^2 \Delta m}{A\sqrt{\rho_q \mu_q}} \tag{3.1}$$

where Δf is the change in frequency, f_o is the unloaded resonance frequency, Δm is the change in mass loading at the surface, A is the area of operation, ρ_q is the crystal mass

density and μ_q is the crystal elastic stiffness. More recently, Hunt *et al.* [53] presented the subsequent governing equation derived from the surface reciprocity relation using time-dependent perturbation theory,

$$t\frac{\partial\Delta\omega}{\partial t}+\Delta\omega=\frac{\omega_u\cdot h_f}{\pi\sqrt{\rho_q\mu_q}}\left\{-\omega_u\left[\Delta\rho_f-\frac{\Delta\mu_f}{V_S^2}\right]+i\left[\frac{\partial\Delta\rho_f}{\partial t}-\frac{1}{V_S^2}\cdot\frac{\partial\Delta\mu_f}{\partial t}\right]\right\} \quad (3.2)$$

where the subscript "*u*" denotes the unperturbed field condition, "*f*" denotes the immobilized chemi-specific film, ω is the radian frequency, V_S is the velocity of the shear acoustic wave, h_f is the height of the immobilized surface film and C is a constant to be utilized in satisfying the initial conditions of the differential equation. Assuming that $\Delta\mu_f$, $\Delta\rho_f$ and $\Delta\omega$ do not change with time, the Hunt equation reduces to

$$\Delta f=-\frac{2\cdot f_u^2\cdot h_f}{\sqrt{\rho_q\cdot\mu_q}}\left[\Delta\rho_f-\frac{\Delta\mu_f}{V_S^2}\right] \quad (3.3)$$

which is analogous to Sauerbrey's equation with the addition of a surface film stiffness dependency. The resulting equation predicts that a frequency shift in a TSM sensor will occur as a result of increased mass density in the immobilized film, as predicted by Sauerbrey. The equation also predicts that the operating frequency of the resonator can also be affected by a change in the stiffness of the film. An increased stiffness change could counteract the shift resulting from an increase in mass-density. This result helps to explain why a positive frequency shift may be observed in mass detection studies – wherein the mass detected is offset by a subsequent stiffening of the sensing layer.

A major limitation of the Sauerbrey equation is that it describes a simplified situation, which assumes operation in air and a rigid solid film deposited on the quartz surface. In the case of operation in a liquid environment, the situation becomes more complicated and can no longer be described by the Sauerbrey equation. The reduction in

resonant frequency by a fluid film can be attributed to a coupled interfacial fluid layer. To describe the operation in liquid more accurately, Kanazawa and Gordon [54] derived an equation that relates the frequency shift Δf to the effective mass loading of the fluid layer. The effective mass is related to the shear wave penetration depth, which is a function of the viscosity of the liquid, η_l, operating frequency, f_o, and density of the liquid ρ_l. The Kanazawa-Gordon relation is then:

$$\Delta f = -f_o^{3/2}\sqrt{\frac{\eta_l \rho_l}{\pi \mu_Q \rho_Q}} \tag{3.4}$$

where μ_Q is the stiffness of the quartz crystal, and ρ_Q is the density of the quartz. It is evident from Eq. 3.4 that a TSM-sensor based on viscosity-density changes of the contacting liquid can be developed [55]. That is not to say that mass, density, and viscosity, of the contacting film are the only determinants of the resonant frequency of the device. Surface roughness, fluidic pressure, surface hydrophobicity, and film viscoelasticity are just a few of the other parameters that can effect a change in the resonance condition. However, in the studies presented in this thesis, it is stressed that the use of a reference sensor is vitally important to cancel out any of the effects of these factors based on the assumption that they affect the target and reference sensor equally.

3.2 Finite Element Modeling

An initial step in the process of designing any complex device is typically to develop an effective model to help guide the design and optimization process. One particularly useful tool in the design of piezoelectric acoustic devices is finite element software. The finite element method is useful for solving partial differential equations over complex 2 and 3-dimensional spaces. In this work, Comsol Multiphysics© was used

for developing the finite element models because of its ease of usability, powerful processing capabilities for piezoelectric models, in-depth post-processing capabilities, and attractive output plots.

In order to verify the process of modeling piezoelectrically-coupled acoustics in Comsol, the first step was to model the Quartz Crystal Microbalance. The QCM is comprised of an AT-cut quartz plate and is by far the most widely studied and understood thickness shear mode resonator. For these reasons, it is a prime candidate for validation of the modeling process. If the results obtained from the modeling process are consistent with the well-known operation of the QCM, then assurance is provided that results obtained from the model of an unknown system can be trusted.

3.2.1 Material Definitions

One would assume that different cuts of quartz, i.e. the AT-cut, are relatively well documented in the field of crystallography since the QCM is so widely used in such a broad range of industries. This however, is not the case. It turns out that there are conflicting definitions of the AT-cut depending on what source is consulted. The definition of the cut corresponds to the angles at which the cut is made with respect to the original orientation of quartz. In the *IEEE Standard of Piezoelectricity* [56], an AT-cut plate is defined as having the notation (YX*l*) -35°. While the IEEE naming convention is of little importance here, the image describing the cut is shown in Figure 3.1 which describes the AT-cut as a cut made 35°from the positive z-axis towards the positive y-axis. Conversely, in Bottom [57] the cut is described as having an angle of +35.25°. The issue of the rotation of the plate with respect to the z-axis is what is most important, since quartz is a trigonal crystal. Figure 3.2 illustrates a conflicting definition of the AT-cut

which shows the cut at approximately 35°from the z-axis in the direction opposite from the +y-axis [58]. The difference in angles between 35° and 35.25° is not of importance here since the angle of cut for the QCMs used in the experiments discussed here was verified to be 35.25° from the manufacturer. Further, these cuts are all considered to be in the family of AT-cut quartz, each providing slightly different frequency-temperature characteristics.

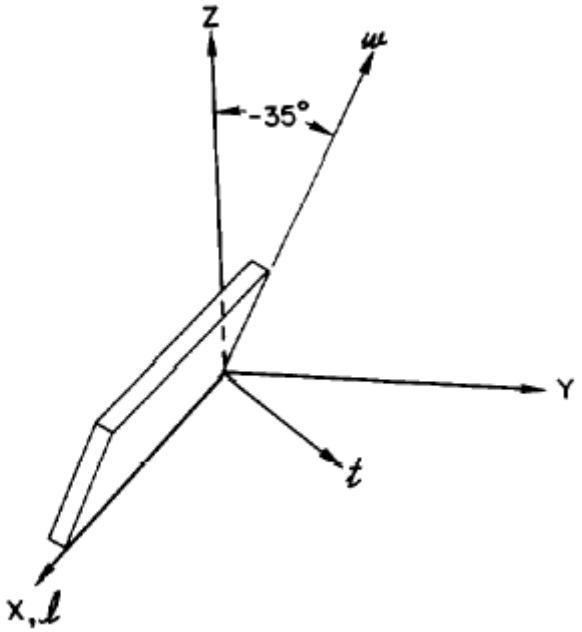

Figure 3.1 Illustration of an AT-Cut quartz plate having the notation (YXl)-35

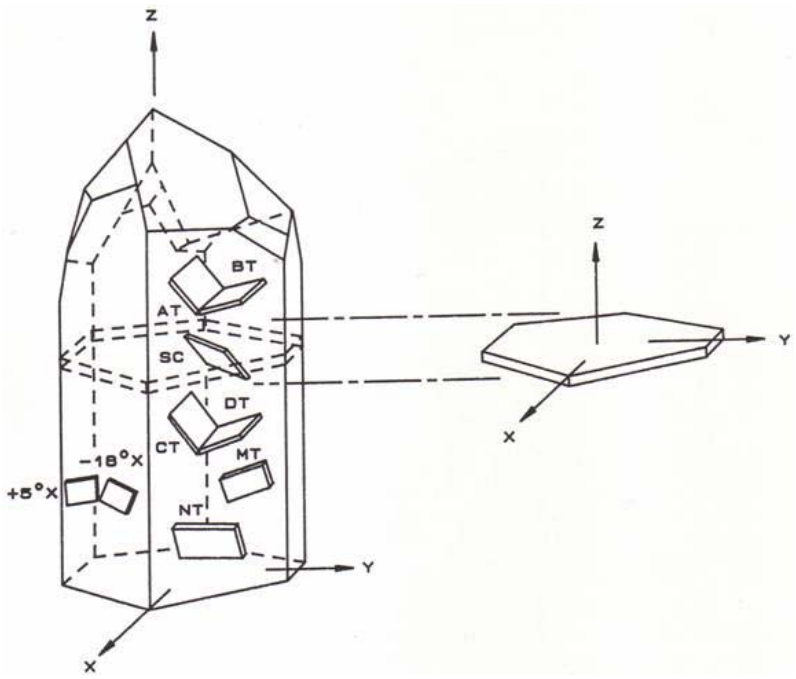

Figure 3.2 A composition of the most common quartz cuts in relation to the crystal structure. From [58]

The IEEE Standards Committee has recommended that coordinate systems be used such that right-handed systems of axes are used with right-hand quartz and conversely left-handed systems are used with left-hand quartz. In 2000, the IEEE retracted their *Standard on Piezoelectricity* and so the issue of the angles remains somewhat ambiguous. However, after speaking with one of the chief standards officers for the IEEE piezoelectricity committee, Dr. Thrygve Meeker, it was found that the proper alignment given a y-cut quartz plate as the starting substrate is -35.25° and that the AT-cut is always nearly parallel to the minor rhombohedral face regardless of handedness. The generally accepted convention is that when using right-handed systems for right-hand quartz and vice versa for left-hand quartz, a clockwise rotation about the x-axis is denoted as a negative angle when looking down the positive end of the axis toward

the origin, while a counter-clockwise rotation is positive. It turns out that part of the confusion about these angles stems from the fact that the conventions for handedness and the positive sense of the axis have changed several times in the past [59]. Particularly, the differences arose from the translation of ideas from crystallographers to engineers. In 1945, the Institute of Radio Engineers attempted to standardize the notation to the crystallographic nomenclature. However, it is apparent that this attempt must not have been very successful because sources still conflict on this matter 60 years later.

The ambiguities about quartz do not, however, end at the angles of rotation for various quartz cuts. In fact, the definitions of the stiffness and piezoelectric stress matrices vary from source to source as well. Quartz is classified under the trigonal system with a class of 32. This means that quartz has threefold symmetry about its z-axis (sometimes called *c*-axis) and the three x-axes (sometimes called a_1, a_2, a_3) have two-fold symmetry. There is some confusion as to what the correct value of the stiffness constant c_{56} is for trigonal 32 material stiffness matrices. Both Auld [18] and Rosenbaum [17] agree that it should be the same value as c_{14} hower, in a publication by Bechman, the value of c_{56} equates to 2* c_{14} [60]. Similarly, in Bechman, the value of e_{24} and e_{25} in the piezoelectric stress tensor are switched in relation to what Auld and Rosenbaum have published. These matters are just another example of the disarray of the documentation of information regarding quartz crystals and their properties. Because the Bechman work was published quite a long time ago and because Auld and Rosenbaum are considered to be such authorities in the field of resonator design, I have chosen to model the QCM with the tensor parameters described by Auld and Rosenbaum. The exact accuracy of this model is not very important. The aim of modeling a QCM is simply to show that it is

possible to accurately model the behavior of acoustic waves excited by time-varying fields in a piezoelectric bulk using Comsol.

3.2.2 Methods

To help make verifying the results easier, the geometric parameters of a device previously modeled by Lu et. al were chosen [61]. The crystal plate thickness was 0.4mm and the diameter was 12 mm. While this is thicker than a typical QCM, it was a necessary requirement of the model due to the immense computational power required to solve a model consisting of an aspect ratio as high as that of an actual QCM. In Comsol, a piezoelectric crystal can be modeled in one of two ways. In the first method, the crystal geometry can be aligned with any one of the three major axes and the normally un-rotated piezoelectric tensors can be transformed using Euler angles to give the correct tensor values for the crystal in relation to the local axis system. The other method is to align the model geometry with the unrotated tensor values which correspond to the x, y, and z-axis of the Comsol coordinate system. Essentially, rather than rotating the material tensors, the crystal geometry is rotated to match the cut similar to that seen in Figure 3.1.

The finite element analysis was performed using the Piezo_solid application mode. This application mode is formulated using the principle of virtual work which states that the sum of virtual work from internal strains is equal to work from external loads. It allows the user to set all material properties including stiffness tensors (if using the stress-charge form of the Constitutive Relations), permittivity tensors, coupling tensors, and density. The constitutive equations transformed for the analysis of choice are implemented in weak form, which is a result of the formulation through the principle of virtual work. The weak form of a differential equation gives the user direct access to the

terms of the weak equation and provides maximum freedom in defining finite element problems – including boundary conditions. This is one reason why the mathematical weak form is often used for finite element analyses. For a time-dependent analysis, Comsol uses the time-harmonic equation:

$$\nabla \cdot (c\nabla u) + \omega^2 \rho u = -\nabla \cdot T \tag{3.5}$$

where $u = \tilde{u}e^{j\omega t}$, ρ is the density, and c is the stiffness tensor. When combined with the equations for piezoelectricity, the resulting equation results in a coefficient form partial differential equation that can be implemented in weak form.

The electrodes were simulated without mass or volume because of the difficulty in meshing electrodes with such a small thickness compared to the thickness of the device. The electrodes are a requirement of the model for implementing a ground electrode and a boundary condition with a time varying voltage. The top electrode was set to a time-varying voltage with a frequency of 4.25 Mhz as per the resonance frequency of the model from Lu et al. The bottom electrode was set to ground. The other boundary conditions were set such that all boundaries except for the electrode-substrate boundaries were set to imitate an air boundary. Using scaling factors, the model was first decreased in size, then meshed, and then expanded to its normal size. This method allows for much coarser meshes than can typically be obtained. While a course mesh is typically undesirable, the computing power available at the time of simulation would not afford any further meshing. The mesh of the QCM device geometry is shown in Figure 3.3.

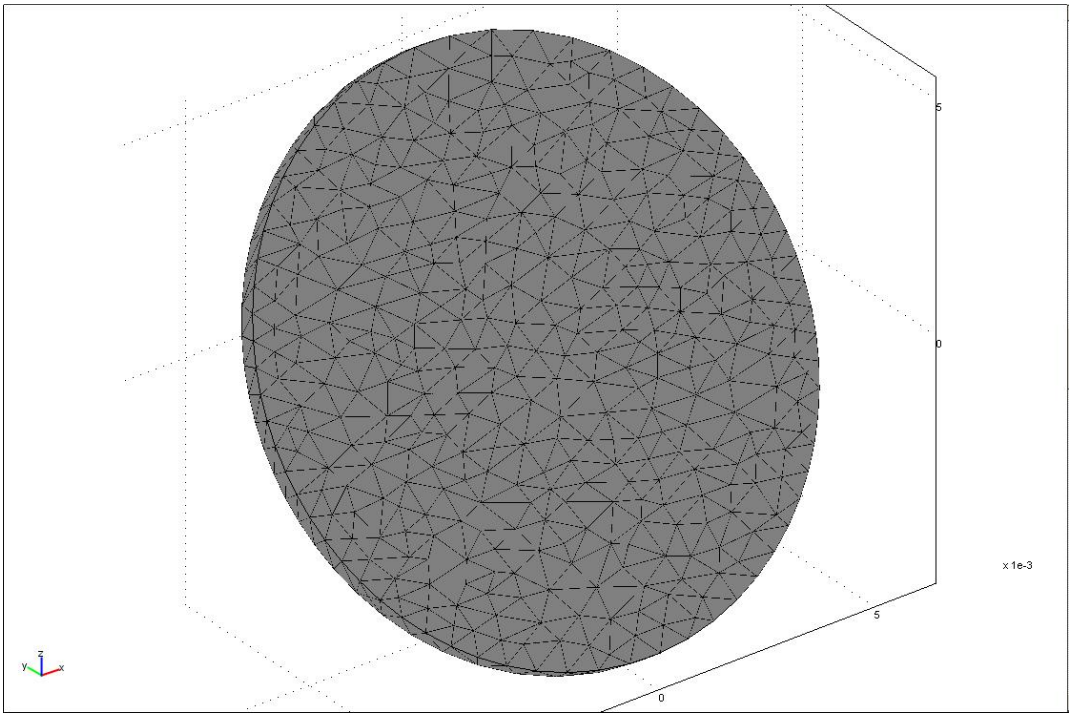

Figure 3.3 The mesh of the QCM device geometry

Given all of the material properties and boundary conditions, the model was solved using a time-dependent solver to step through four periods of excitation. Following successful solving of the model, the post-processing tools of Comsol were utilized for visualization of the particle displacement.

3.2.3 Modeling Results & Discussion

The results from this model were indicative of a thickness shear wave in the quartz. The wave exists almost exclusively where the electrodes overlap which is in accordance to what is predicted by Lu et al. Particle displacement can be seen just outside of the electrode area, however this particle displacement is due to waves propagating towards the perimeter of the crystal. The particle displacement in this region is not a direct result of the electric field coupling to mechanical strain. Rather, it is mechanically

coupled and therefore suffers from attenuation as the wave front propagates away from the electrode. A plot of the particle displacement is shown in Figure 3.4.

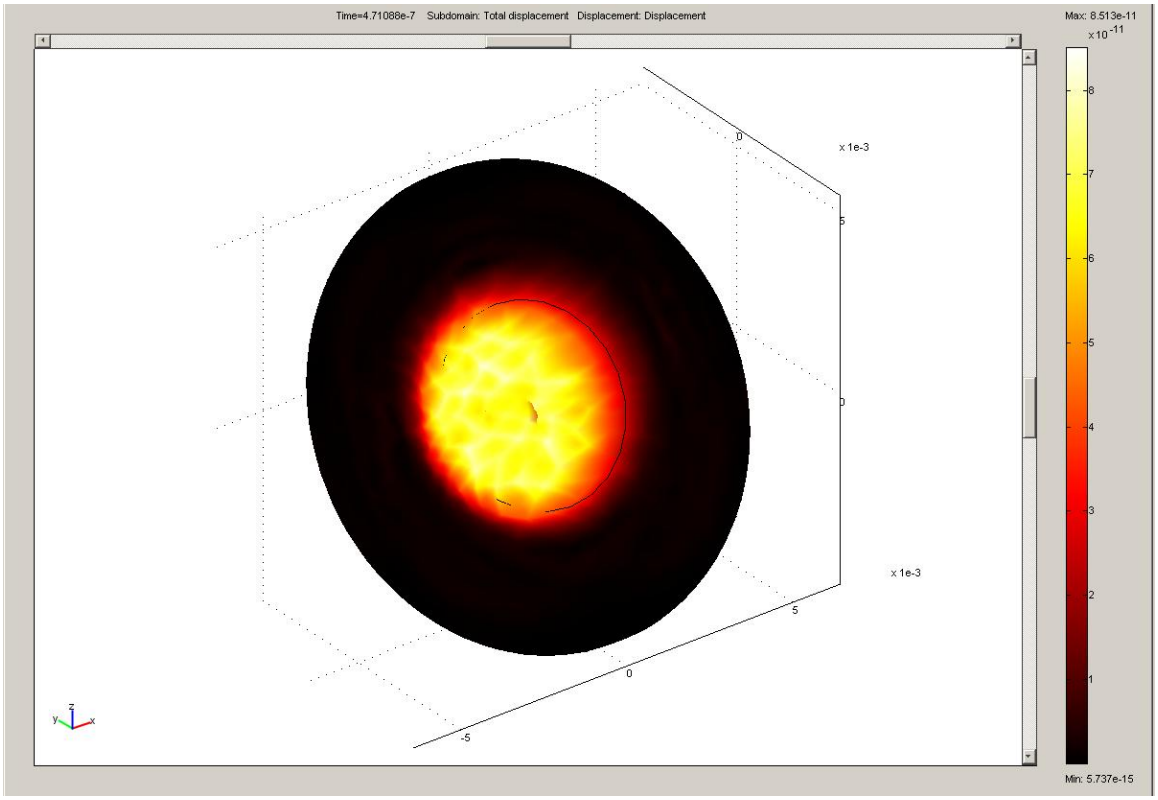

Figure 3.4 Visualization of the total particle displacement at its maximum

Areas of high particle displacement, indicated by the light areas, are located in the circular area in the center of the QCM. This is the only area where the electrodes on either side of the QCM overlap since the sections of the electrodes leading out to the edge of the crystal are on opposing sides. The resulting particle displacement confirms for us a few things that are important. First, the electric field being generated by the electrodes is confined almost entirely in the crystal sandwiched between the overlapping electrodes. Second, we see that this surface-normal directed electric field couples to the shear particle displacement as indicated by a cross-sectional plot of the particle displacement.

Since one of the analyses performed on the model was a time-dependent analysis, it was possible to visualize the build-up of particle displacement starting at t = 0 s which could help to indicate resonance taking place at a particular frequency. The idea is that the particle displacement would build over a few periods for frequencies near to the resonant frequency. For excitation at a frequency away from the resonant frequency, the particle displacement would be minimal because the natural harmonic resonance of the structure would not be in-phase with the excitation field resulting in destructive interference. It is not possible to monitor the build-up over many excitation periods due to computational complexity, however the particle displacement was monitored for four periods of the excitation frequency. The results indicate a definitive increase in the particle displacement amplitude at the point of maximum displacement as a function of increasing period number (i.e. 1 through 4). While this is not completely indicative of resonance being supported in the structure because of the short time period allowed for the model, it does give a good approximation of how resonance would exist for an excitation frequency that is at the fundamental harmonic frequency.

The results of the QCM model predicting the physical operation of the device agree very well not only with the operation of an actual QCM, but also with independent results of another finite element model for the QCM [61]. These results provide confidence in the Comsol software package for modeling piezoelectric devices as well as in the author's modeling process. The results seem to suggest that modeling a new acoustic device such as a ZnO-based resonator would be possible and that the results obtained from such a model would closely predict actual physical device operation.

3.3 Biosensor Testing

There have been many research articles published in the past employing the QCM as a sensor for detecting myriad molecules. However, prior to this work, there had been no demonstration of the ability for a QCM to operate as a biosensor in complex-media for the detection of a cancer biomarker. The usefulness of such a study lies in verification that, in general, a TSM acoustic wave device is capable of detecting specifically targeted proteins in a solution that contains hundreds if not thousands of different proteins, often in concentrations much higher than the one of interest. Validation of this will provide confidence that future TSM devices will likewise operate properly in a similar complex solution.

To study these capabilities, we chose to apply QCM sensor technology to the detection of mesothelin, a potential biomarker for mesothelioma, ovarian, and pancreatic cancer. As previously mentioned, when antigens such as mesothelin bind to an antibody layer immobilized on the surface of a QCM, mass and stiffness changes occur in the coating. These changes cause the resonant frequency of the device to shift. Since the resonant frequency is measurable in real-time, protein binding can be detected as it occurs. QCM technology has been implemented as an immunosensor to detect mesothelin in an effort to illustrate the feasibility of acoustic wave devices as real-time, early detection instruments for cancers that possess a specifically correlated protein biomarker The work described below has been published in a previous journal article by Corso *et al.* [12].

3.3.1 Materials and Methods

3.3.1.1 Reagents and Materials

Pancreatic cancer cell line supernatant samples were obtained from the Johns Hopkins Cancer Center. Anti-mesothelin NCL-MESO MAbs were obtained from Novocastra Laboratories Ltd. For all experiments, 10 MHz AT-cut Quartz Crystal Microbalance (QCM) oscillators were used. These were obtained from International Crystal Manufacturing Co, Inc.

3.3.1.2 Apparatus

Two 11Plus syringe pumps (Harvard Apparatus, Holliston) provided the fluidic injection. Syringe pumps were chosen, as opposed to peristaltic pumps, because they provide a more constant fluid flow. To concentrate the binding interaction to a small and specific volume, 70 µl reservoir acrylic flow cells (International Crystal Manufacturing Co, Inc., Oklahoma City) were used. Standard crystal oscillator circuits (International Crystal Manufacturing Co, Inc., Oklahoma City) amplified the resonant frequencies of the QCM crystals. The oscillator outputs were connected to a frequency counter (Maxtek, Inc., Santa Fe Springs) for the determination of the frequency. A laptop computer running a Labview software program written by Aysem Elgul was used to collect and display the data from the frequency counter in real-time.

3.3.1.3 Antibody Immobilization

Antibody immobilization was accomplished by using alkanethiol self-assembled monolayers (SAMs) [62]. These molecules are lined up into a well-ordered layer on the surface. For our purposes, a short-chain carboxylic acid-terminating alkanethiol layer

provided the adhesion for the antibodies to the gold electrode surface. The method of antibody immobilization employed in this study is a random one and does not denote any form of homogeneity in the biolayer. However, because the same protocol is applied to a control device we rely on a differential response to determine our ability to reproduce the data. In normal coupling schemes, coupling does not discriminate between possible attachment points near or removed from the specific binding site (or sites), which results in spatial orientation of antibodies on the electrode that may not provide the optimum conditions for forming antigen-antibody complex. The presence of lysine groups on the surface of an antibody provides possible attachment points. Consequently, this can result in different orientations of the antibody on the electrode depending on the location of the lysine group severely impairing its ability to bind the antigen.

To prepare the oscillators for the antibody coating, the gold surfaces of the QCM crystals were cleaned using a Piranha solution (3 parts H_2O_2 in 7 parts 1 M H_2SO_4). The Piranha solution was applied only to the gold surface and was left on for approximately two minutes to clean the surface. The solution was rinsed off with deionized water and the crystals were air-dried. 3,3'- dithiopropionic acid (0.0234g) was dissolved in 100% ethyl alcohol to make a 0.01 M alcoholic solution. The solution was applied to the gold electrodes and incubated overnight to allow the monolayer to assemble. The surface was then washed with 95% ethyl alcohol followed by aliquots of deionized water before being air-dried.

1-Ethyl-3-(3-dimethylamino-propyl) carbodiimide (EDC) (0.0133 g) was dissolved in 0.1 ml of 1X Tris-Acetate-EDTA (TAE) buffer (10 times less dilute than the 10X buffer). N-Hydroxysuccinimide (NHS) (0.0135 g) was also dissolved in 0.1 ml of

buffer and mixed with EDC solution and the resulting mixture was incubated with the QCM surface for 30 min. The surface was washed with de-ionized water and allowed to dry. Mouse anti-mesothelin IgG1 (10 µl of 100 µl/0.1 ml TAE buffer) was incubated on the QCM gold electrodes for 6hrs. For the control sensors, mouse monoclonal anti-Fluorescein isothiocyanate (FITC) IgG2a (10 µl of 100 µl/0.1 ml TAE buffer) was incubated on the QCM gold electrodes for 6hrs. Anti-FITC was chosen because it is specific to a synthetic molecule, which should not be present in cell supernatant. The reference sensor therefore includes a sensing layer with similar mass density characteristics as the target sensor, but should not bind any particles present in the supernatant. Following immobilization, the crystal was washed with TAE buffer and allowed to dry. Aliquots of ethanolamine were used to block remaining reactive sites on the QCM surface. Finally, the surface was washed with de-ionized water and allowed to air dry.

3.3.1.4 Experimentation

The PL1 cell line was chosen for testing because it is a low-passage pancreatic carcinoma cell line. The CAPAN2 cell line was chosen because it has previously been shown through serial analysis of gene expression (SAGE) to contain an elevated number of mesothelin transcripts (129 mesothelin tags/million) [7]. Supernatants of these cells were obtained by the Hruban group at Johns Hopkins by culturing these cells in serum free media (RPMI) for 48 hours. Since supernatant is a complex mixture of many different types of proteins, the supernatant samples in these experiments contained an unknown concentration of mesothelin. For this study, testing samples of purified mesothelin to corroborate findings from the supernatant would be a logical first step.

However, at the time, we were unable to obtain purified mesothelin due to its lack of availability. The other logical option would be to test the sensors against supernatant containing mesothelin versus supernatant without mesothelin. Because mesothelin naturally exists in pancreatic cell lines and is only overexpressed in various types of pancreatic cancer cells, it would be extremely difficult to find samples containing no mesothelin. In spite of this, it is possible to extract the pertinent information about the QCM system for biomarker detection in complex media and to offer some insight about the capabilities of a TSM resonator.

Syringe pumps were used to inject the buffer and target solutions into the flow cell because they provide an even flow rate. One pump controlled the flow rate of target sample solutions while the other syringe pump controlled the constant flow of 1X TAE buffer. The inlet of each flow cell was connected both to a supernatant syringe and a buffer syringe. The sensors were then connected to oscillator circuits, which were connected to the frequency counter. This novel approach uses a constant flow of buffer to wash away any unbound analyte and was first used by Lee et al. [63]. The setup described above is illustrated in Figure 3.5.

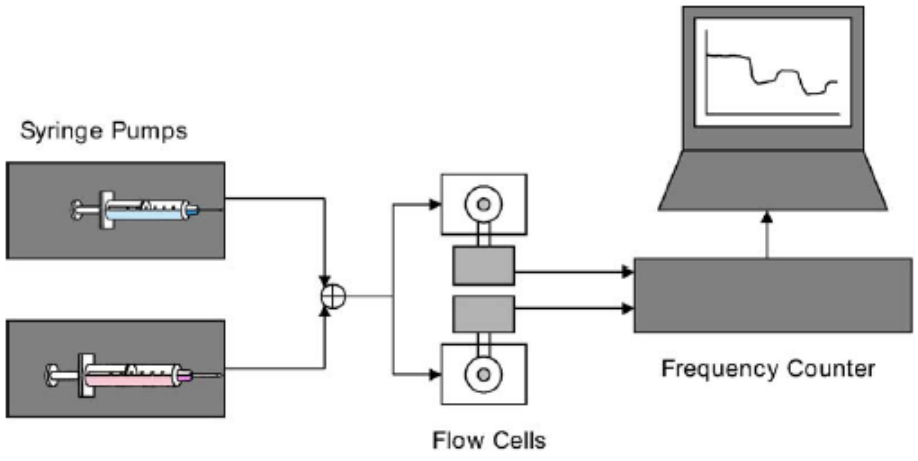

Figure 3.5 QCM experimental setup

This flow-through approach differs from the static "well" approach in which the analyte is introduced into a well such that the column of liquid is resting on the surface of the sensor. The "well" method allows the forces of gravity to pull particles down to settle on the sensor which may cause false-positive data readings over an extended period of time when injecting a solution such as supernatant because of the variety of proteins that are present. Flow-through experiments were performed in three different ways.

In the first type of experiments, buffer solution was flowed constantly through the flow cells at a rate of 0.1 ml/min to wash away any unbound analyte and to prevent faulty readings. Supernatant solutions (1 ml) were obtained by combining various amounts of PL1 or CAPAN2 with 1XTAE Buffer to obtain the desired concentration. The 1 ml supernatant solution was then injected into each of the flow cells at a rate of 0.3 ml/min. Following the injection of the supernatant, the sensor frequencies were allowed to settle. Once settled, another 1 ml sample of the supernatant was introduced to the each of the flow cells at a rate of 0.3 ml/min. The system was then allowed to settle again to the final resonant frequencies. This experiment was designed to show two frequency shifts due to two separate binding periods. The initial frequency shift occurs when the supernatant solution is first introduced to the sensor. The second frequency shift occurs after the second injection of supernatant. The second type of experiments followed roughly the same procedure. A 1X TAE buffer solution was flowed constantly through the flow cells at a rate of 0.1 ml/min. The constantly flowing buffer helps to remove unbound protein from the sensor surface. 1 ml supernatant solutions were obtained by combining varied amounts of supernatant with 1X TAE Buffer. A uranine solution was created by combining 20 µl of uranine solution with 980 µl of 1X TAE Buffer. Uranine is a

fluorescent molecule not found in biological samples. The 1 ml uranine solution was first injected at a rate of 0.3 ml/min into each of the flow cells. Following the injection of the uranine, the sensor frequencies were allowed to settle. Once settled, the 1 ml sample of the supernatant solution was introduced to each of the flow cells at a rate of 0.3 ml/min. The system was then allowed to settle again to the final resonant frequencies.

In the last type of experiments, 1 ml solutions of CAPAN2 and PL1 supernatant in buffer were prepared in the same way as above. The buffer was first constantly flowed through the flow cells at a rate of 0.1 ml/min to allow the sensors to settle to a beginning frequency. The buffer flow was then stopped and the supernatant solution was injected for a short period of time. After injection of the supernatant solution, all injections were stopped and the system was allowed to stabilize. After approximately five minutes, the buffer solution flow was restarted and the new baseline frequency shift was observed.

3.3.2 Results

The normalized transient responses of the anti-mesothelin sensor and the anti-FITC sensor for an experiment in which two consecutive supernatant samples were introduced to the sensors are shown in Figure 3.6. The normalized data was obtained by subtracting the sensor frequency when the experiment began from the frequency at each time point. The frequency fluctuations during injection are due to fluidic pressure and viscosity and can be interpreted as the noise floor because they are not a result of antigen-antibody binding. With constantly flowing buffer solution to wash away unbound analyte, the sensors were allowed to settle and the initial baseline shift was observed. The time period allowed for the sensors to settle was dependent upon the sensor responses. In

each experiment, the sensors were monitored and verified to have stabilized before introducing a second sample injection because the responses can be monitored in real-time. After the second supernatant injection, the systems were allowed to settle again and a new baseline frequency shift was observed.

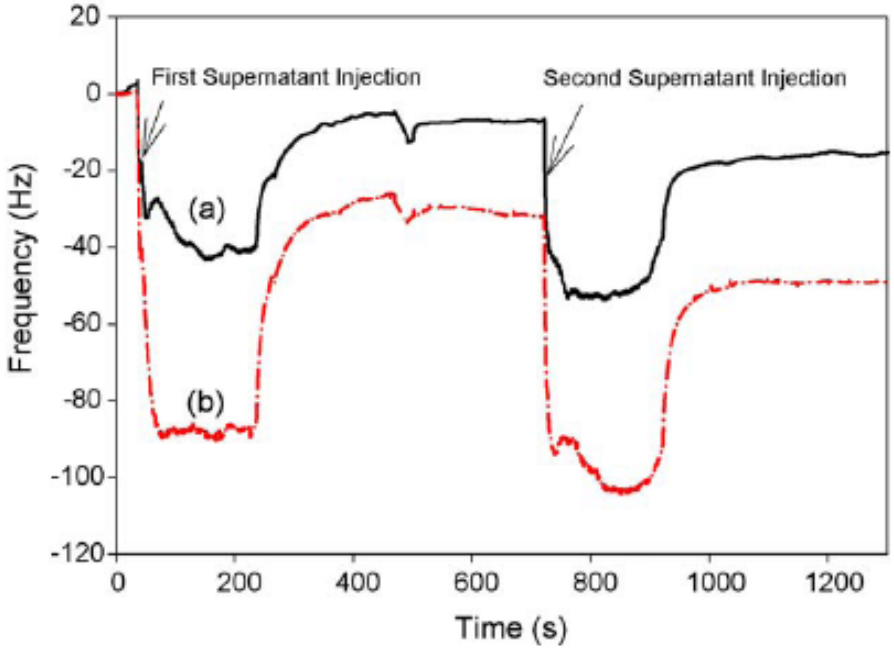

Figure 3.6 Normalized transient responses of a) anti-FITC and b) anti-mesothelin coated sensors to two injections of 20 µl/ml PL1 supernatant. The first injection of the supernatant solution was begun at 40 s with an injection rate of 0.3 ml/min. The injection finished at 235 s and frequencies were allowed to stabilize. At 716 s the second injection of PL1 supernatant was begun. The injection was finished at 925 s.

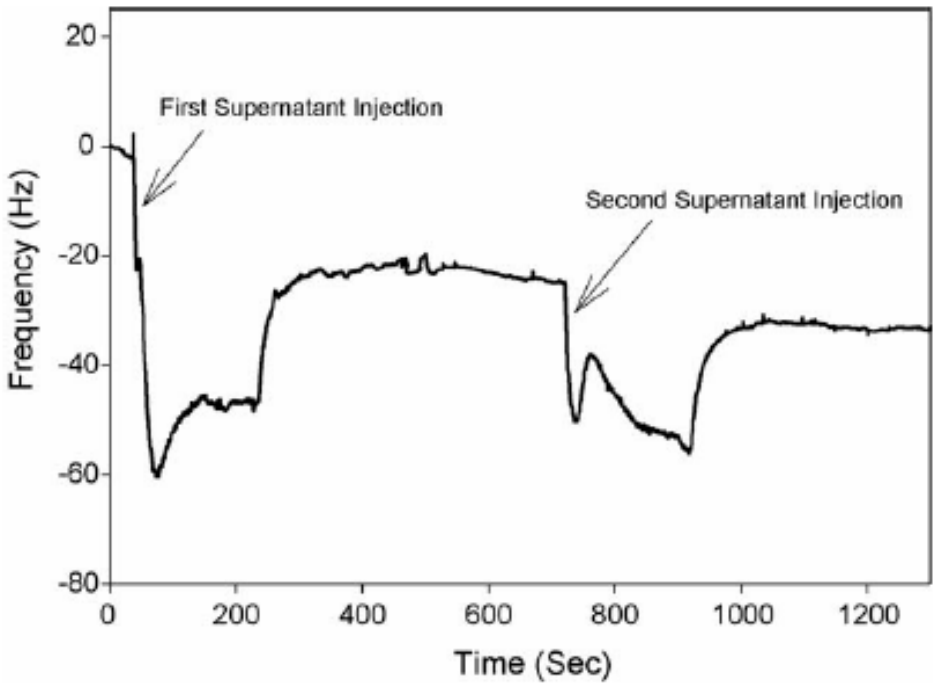

Figure 3.7 Normalized differential transient response of anti-mesothelin and anti-FITC coated sensors to two supernatant injections

To illustrate the true frequency shift in the anti-mesothelin coated sensor, a differential plot can be used. This plot is obtained by subtracting the normalized anti-FITC response from the anti-mesothelin response at every data point. This is done to subtract out any non-binding phenomena that occur in both sensors. For example, fluidic turbulence can cause acoustic sensors to react in ways that are uncharacteristic of their sensing responses. When only looking at the response of one device, it is impossible to discern to what effect factors like turbulence, pressure, and viscosity have on the resonant frequency shift. It is because of this that we have employed the use of a reference sensor. Ideally, the response of the reference sensor to the target solution will give us a standard for how these factors are affecting a coated QCM which should not bind the target. We can then use that response to subtract out the effects of these factors on the target sensor, leaving only the sensor response due to target binding. The differential transient response

of the experiment from Figure 3.6 is shown in Figure 3.7. This plot gives us the true response of the target sensor because all of the background disturbances such as pressure and viscosity effects that occurred in both sensors have been removed, thus allowing a clearer view of what is occurring throughout the experiment. The frequency after the first injection returns to a shifted frequency and fluctuates around -23 Hz. At this point, it is hypothesized that not all of the anti-mesothelin binding sites are occupied by mesothelin proteins. This is indicated by the response of the sensor following the second injection of the supernatant solution. At approximately 925 s, when the second injection is stopped, the sensor begins returning to a shifted resonant frequency. This time, the total shift is greater than after the first injection, roughly -33 Hz. More proteins in the supernatant were bound to the antibodies on the electrode causing a new mass change and a further frequency shift. It is important to note, however, that the frequency shift that occurred from the time after the first injection to the time after the second injection was only approximately 10 Hz, while the shift that occurred from the initial resonant frequency to after the first injection was approximately 23 Hz.

For clinical detection modalities, the frequency shift of the sensor is not very useful without quantifying the amount of protein bound. The Sauerbrey equation enables us to quantify the mass of protein bound to the surface by relating the frequency change to the mass difference when the parameters of the resonator are specified. This equation, however, does not account for a stiffness change in the biofilm as a result of conformational change upon antigen-antibody interactions as shown through X-ray crystallography [64].

As a best approximation for the amount of protein bound, we used the Sauerbrey equation. A frequency shift of -23 Hz corresponds to a calculated mass change of approximately 20.9 ng on the surface of the device. The final frequency shift of -33 Hz corresponds to a mass difference of approximately 30.0 ng.

It is important for a sensor used for mesothelin screening to show specificity for mesothelin and other molecules in a complex mixture. The second type of experiment that was performed involves the injection of both supernatant and uranine and aims primarily at showing the specificity of the anti-mesothelin coated sensor to mesothelin. Figure 3.8 shows the normalized response of the anti-mesothelin sensor both to uranine and the supernatant solution.

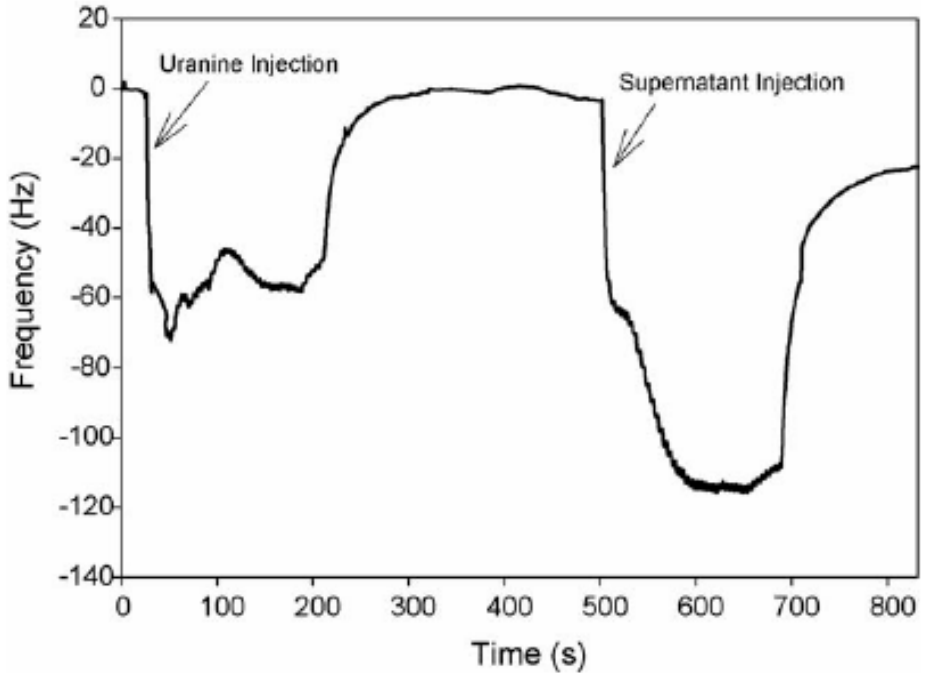

Figure 3.8 Normalized transient response of an anti-mesothelin coated sensor for an injection of uranine followed by an injection of 20 ml/ml PL1 supernatant solution. At 25 s, the injection of the uranine solution at 0.3 ml/min began. It was stopped at approximately 221 s. The frequencieswere allowed to settle to the baseline frequency.At approximately 500 s, the PL1 solution was injected into the flow cells at a rate of 0.3 ml/min. The injection was stopped at 690 s.

Since the frequency of the sensor returns to the baseline frequency at which it began following the injection of uranine, it is concluded that no binding occurred since there is no mass change and thus, no frequency change. Following the injection of the 20 µl/ml PL1 supernatant solution, the sensor response settles to a new shifted frequency of approximately -22.4 Hz. According to the Sauerbrey equation, a 22.4 Hz frequency shift corresponds to a mass difference of 20.3 ng.

The last type of experiments were carried out to investigate the sensor response when the buffer is not constantly flowed, but rather is injected at specific times to wash away unbound protein after the injected supernatant solution has been given time to react and bind in the chamber statically. Figure 3.9 illustrates the effect of allowing the

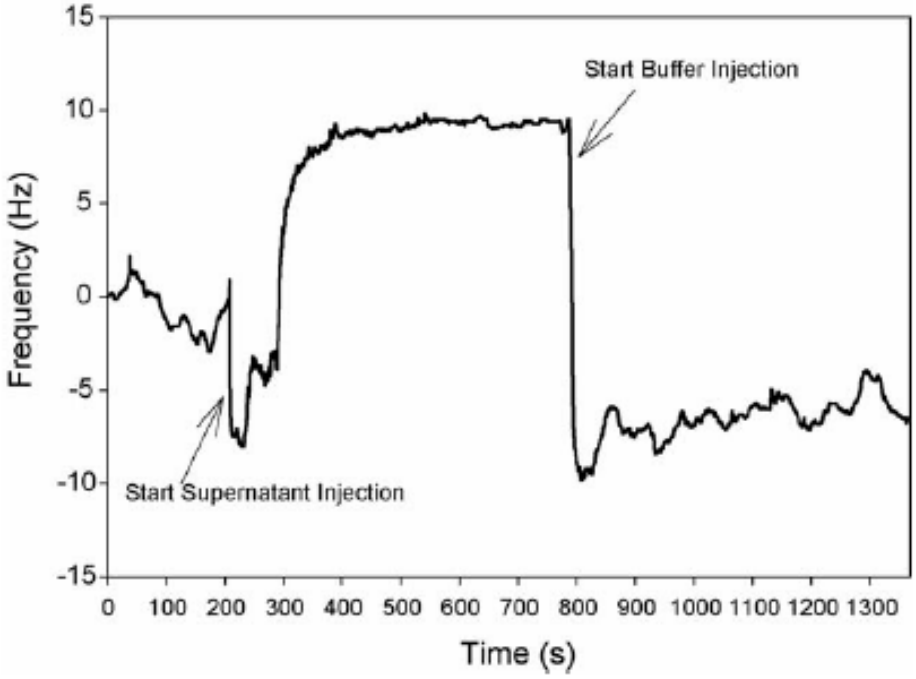

Figure 3.9 Normalized differential transient response of anti-mesothelin and anti-FITC coated sensors from non-constant injection of 10 ml/ml CAPAN2 supernatant and buffer. 1XTAE buffer was flowed through the flow cells until 210 s. The supernatant was injected from 210 s until 295 s. Following a period of no flow, the buffer was started again at 780 s.

supernatant to bind for a period of time, followed by a buffer washing step. The initial data is recorded while buffer flows through the chambers at a rate of 0.3 ml/minute. The buffer flow is then halted and simultaneously the supernatant flow is started. After 1ml of solution has been introduced to the sensor, all flows are stopped and the supernatant solution is allowed to interact with the sensor surface. Upon stabilization of the sensor frequencies, the buffer flow is then restarted. Since the sensor response under 1XTAE flow can be compared to the response of the sensors at the beginning of the experiment because of the equality of flow conditions, a mass related frequency shift can then be detected. It was observed that the restarted buffer flow slowly caused the initial frequency shift to decrease. In the experiment depicted by the data in Figure 3.9, the frequency jumped down to approximately –10 Hz when the buffer flow was restarted. Despite a somewhat varying signal, it was observed the time averaged frequency shift after 10 minutes was approximately –7 Hz.

The experiments discussed above were carried out many times in order to derive a dose-response curve which correlates experimentally obtained frequency shifts with their corresponding concentration of supernatant solution. Figure 3.10 shows the dose response curve with the correlations obtained experimentally for PL1 supernatant.

The frequency shifts for each experiment at the specified concentration were averaged together to get the values shown in the dose-response curve. The error bars correspond to one standard deviation (unbiased). It is possible to see that the responses are non-linear. If the concentration is doubled, the average frequency change does not necessarily double. This is more apparent in the lower concentrations. For those experiments in which a 0.1 µl/ml solution was used, the frequency shift was typically

around 2 Hz. In the experiments with a 1 µl/ml solution, the frequency shift was around 5.7 Hz. One possible explanation for this is because with such a small amount of active proteins in the solution flowing past the surface of the sensor, only slightly more mesothelin proteins interact with the immobilized antibodies and bind even though there is an overall higher concentration. By testing blood serum of both cancer patients and non-cancer patients, it will be possible to develop a dose-response curve as a diagnostic aid in predicting patients in the early stages of cancer less-invasively. However, further work as well as a standardization of flow-through techniques must be completed before this can be realized.

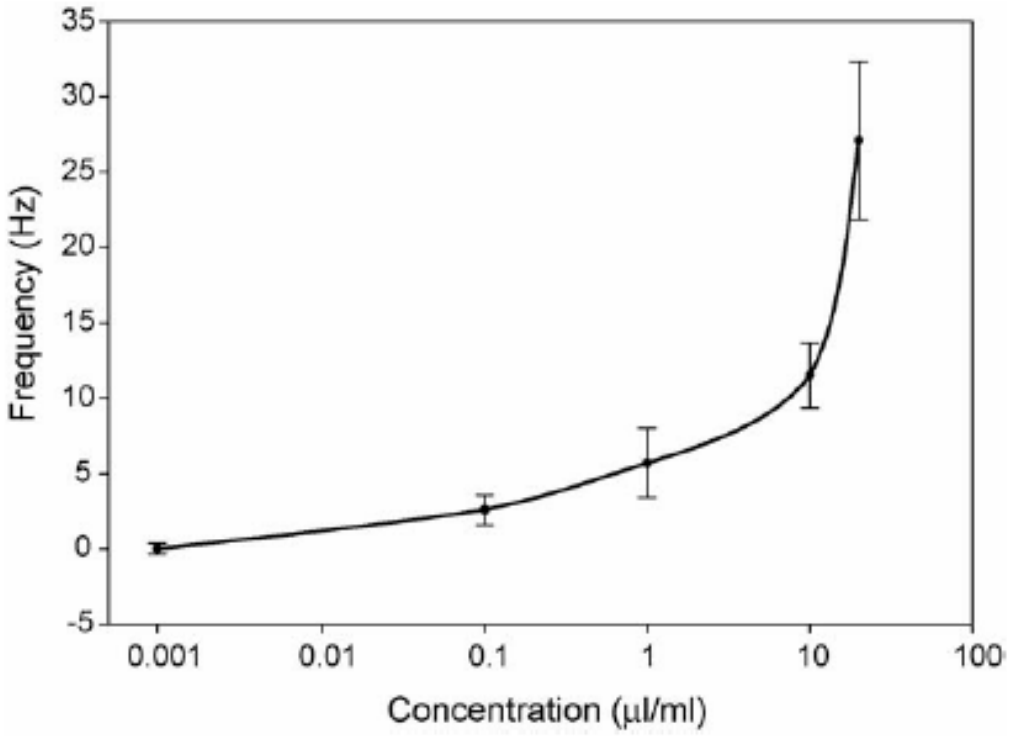

Figure 3.10 Dose-response curve for PL1 cell line supernatant. (Error bars = S.D.)

3.3.3 QCM Testing Discussion

This series of experiments aimed to demonstrate the prospective role of acoustic wave device-based immunosensors in molecular cancer biomarker detection. Since the sensor response to a sample can be monitored in real-time, these devices offer an advantage over other testing modalities. To illustrate this, a QCM system was used to detect mesothelin in two different pancreatic cancer cell line supernatants with three types of experiments. The first involved two injections of the supernatant solution to illustrate an initial frequency shift after the first injection followed by a second shift after the second injection. The sensor response showed that the second frequency shift was smaller than the initial shift. This is evidence that although there were still available binding sites for the mesothelin proteins during the second injection, they were much fewer, thus causing a lower additional mass deposition. The mass change calculated for the experiment described in the text for a PL1 supernatant solution sample was approximately 30.0 ng. This expression level has been indicated in pancreatic cancer cell lines, but further work must be completed to find the approximate amounts of mesothelin present in serum samples from patients with developing cancers before diagnostic testing can be completed.

The next type of experiment involved the injection of a uranine solution not containing mesothelin followed by an injection of the supernatant solution. The sensors showed no reaction to the uranine solution, but showed a clear frequency shift after the supernatant injection. These results suggests that the anti-mesothelin exhibits specificity for the target of interest. Since these sensors are label-free, they should only exhibit a response due to the detection of particles that are tightly bound to the surface since buffer

washing techniques were employed. Therefore, the specificity of the sensor to the antigen is related to the specificity of the antibody for the antigen.

The third and final type of experiment performed involved buffer-washing events to prove the importance of washing flows. Recognition events were verified when a buffer injection following a supernatant injection showed a shifted frequency from the stable state prior to the injection of supernatant during the initial buffer injections. This experiment is interesting because it displays the need for a buffer washing in acoustic wave biosensor detection schemes. It was discovered that when the buffer flow was restarted after the binding period of no flow, the sensor signals jumped down to a shifted frequency indicative of mass change on the surface of the device. This observation can be explained by the idea that the static resting period allowed non-specific particles to adsorb onto the surface of the sensor. When the buffer flow was restarted, it slowly washed away unbound particles from the surface of the sensors causing the frequency to rise as a result of the reduction of mass on the surface. The results obtained here help to illustrate why our methods of buffer washing are important for gaining accurate and dependable results with QCM.

3.4 Chapter 3 Conclusions

Here we have performed theoretical modeling and experimental testing to investigate the usefulness of a TSM acoustic wave for cancer biomarker detection. The QCM was chosen for modeling and for experimental testing because they are well-studied which is important for comparing modeling results, and widely available. However the QCM is not entirely representative of the sensitivity level and size of

acoustic sensors that are currently being developed. They differ from the devices discussed in Chapter 4 of this thesis because in general, they are much larger, and have a higher Quality Factor (Q) which improves their ability to be stably operated in an oscillator circuit. However, because they are lower frequency, they exhibit reduced sensitivity which is something that is important for clinical biomarker detection.

One important implication that arises from an electronic sensor technology such as this is the feasibility of sensor arrays containing numerous sensors coated with antibodies specific to different cancer biomarkers. The QCM is a rather large device and does not easily fit into an array configuration because the sensors cannot be integrated with one another. They are separate devices and must be treated in that way when developing a fluidics system. However, as will be discussed in future chapters, it is possible to develop a sensitive TSM device that has many of the properties of the QCM, but is small enough to be integrated into a multi-device array with relative ease. By combining sensor arrays with recent developments in microfluidic technology, flow cells will become increasingly less expensive to manufacture and the patient sample sizes required for testing will be greatly decreased. The need for sensor arrays arises from the idea that with many types of cancer, testing for just one particular marker does not provide enough information to make an informed decision as to the presence of cancer. However, looking for a specific "signature" of expression levels for a variety of specific proteins may prove to be very useful in future cancer screening protocols.

CHAPTER 4

LATERAL FIELD EXCITATION DEVICE THEORY AND DESIGN

As discussed in the previous chapter, a considerable amount of research has been conducted in characterizing AT-cut quartz resonators as biosensors. In this chapter, the development of a new ZnO-based solidly mounted resonator for biosensor applications is discussed. The proposed device is operated in the thickness shear mode similar to the QCM because of the advantages of the TSM for liquid-phase sensors. The acoustic wave is excited through lateral field excitation of the piezoelectric ZnO film. Theoretical Christoffel equation calculations are provided to explore the conditions for excitation of a TSM wave in *c*-axis oriented ZnO through lateral excitation. Additionally, finite element modeling is performed to supplement the theoretical calculations. The proposed device employs a solidly mounted resonator (SMR) configuration. The theory behind designing an SMR is explored and the advantages to this approach are discussed.

The process of developing a functional resonator based on theoretical evidence has proven to be a long and arduous task full of setbacks. However, functional devices have been achieved and the results embody a novel type of integrated thin-film sensor that can be configured in an array formation. The proof of existence for a TSM wave in the devices is verified through the comparison of theoretical and experimentally obtained acoustic velocity values from frequency versus thickness measurements, and through water loading of the resonators. Characterization of the devices is performed to identify typical device performance metrics such as quality factor, and electromechanical coupling. Additionally, the excitation of the TSM mode through an “off-axis” excitation

phenomenon is discussed and devices employing this mode are explored experimentally as viscosity sensors.

4.1 Introduction & Motivation

In the past, piezoelectric ZnO thin films have been used in the fabrication of FBARs for high frequency filters [65]. Typically these devices are operated in the TE longitudinal mode in which the frequency can be tuned simply by varying the thickness of the ZnO thin film. The particle displacement of the propagating acoustic wave in a longitudinal bulk mode is normal to the surface of the film and generates compressional waves in the medium adjacent to the device surface. When operated in an adjacent liquid medium, the longitudinal mode energy is dissipated into the liquid for devices utilizing waves that propagate at a velocity higher than the acoustic velocity in the liquid. This results in a highly reduced quality factor, Q, and poor mass resolution in a sensor application. The TSM is better suited for liquid sensing applications due to the shear particle displacement of the acoustic wave in the piezoelectric film. Since the adjacent liquid medium cannot effectively support a shear wave, very little energy is transferred into the liquid which results in minimal damping of the thickness shear mode.

As discussed previously, the most common type of TSM resonator is the QCM. It is widely accepted that the theoretical mass sensitivity of these devices is proportional to an exponential of the fundamental resonant frequency, f_o. QCMs typically operate in the frequency range between 5-35 MHz. In AT-cut quartz plates, it is difficult to further increase the fundamental operating frequency because of the dependence on the thickness of the quartz plate. At very small thicknesses, the quartz plate becomes extremely fragile and is difficult to handle. It is possible to achieve higher frequencies with the QCM by

monitoring harmonic modes beyond the fundamental, but these become progressively diminished with increasing harmonic number. Solidly mounted FBARs, on the other hand, do not suffer from this problem because the piezoelectric film is grown directly onto a solid foundation. SMRs are made possible by the fabrication of an acoustic reflector structure directly below the piezoelectric thin film. This acoustic reflector effectively presents the lower side of the piezoelectric material with an acoustic impedance close to that of air over a fairly broad range of frequencies [66]. This results in the reflection of the acoustic energy back into the piezoelectric film, which allows for the utilization of extremely thin piezoelectric sensing layers and, ultimately, very high frequency devices, (i.e. GHz range) can be produced.

The sensitivity of acoustic waves in AT-cut quartz plates has been widely exploited in QCMs which use the TE configuration to excite the wave. As has already been discussed, the lateral field excitation (LFE) can be used to excite the TSM wave as well [67-70] and the resulting device may be more sensitive to surface perturbations than the standard TE QCM for liquid-phase sensing applications [71-74]. The advantages of LFE over TE are mainly attributed to the fact that in LFE, the electrodes that generate the electric field are not directly in the path of the acoustic wave, as in TE. Since the metal that forms the electrode is a source of acoustic wave scattering and damping, its removal from the acoustic path results in higher Q values. Other advantages include increased stability at a given harmonic, and reduced aging of the crystal since the electrode is absent from the area of greatest vibrational motion [75]. For biosensor applications, removing the electrode from the acoustic path means that biological molecules can be immobilized directly onto the region of highest particle displacement which should result

in greater sensitivity of the sensor. While this is advantageous for device sensitivity, it requires the use of surface immobilization techniques that are capable of linking antibodies to the ZnO surface rather than to Au electrodes, which is the most common protocol used for functionalizing acoustic sensors. A discussion of the surface chemistry required to accomplish antibody immobilization on planar ZnO surfaces is provided in Chapter 5.

There has been varied interest, thus far, in generating a thickness shear mode in ZnO for acoustic devices. One of the more highly investigated methods involves the growth of inclined *c*-axis oriented films [76] coupled with an electrode pattern in which the electrodes are situated on opposite sides of the thin film to produce an electric field through the thickness. Wang and Lakin had excellent success in fabricating oriented films with the *c*-axis oriented 40° to the substrate normal [77]. While their resonator Q and electro-mechanical coupling were high, the operating frequency was low (~293 MHz) and the fabrication procedure required bulk etching of the Si wafer to produce the air-backed ZnO membrane resonators. More recently, Link *et al.* [78, 79] have revived inclined ZnO growth research with the intent of developing ZnO TSM resonators for liquid phase sensing. A shortcoming of the inclined ZnO growth method is that the thickness excitation requires that the electrodes be in the path of the acoustic wave. While it offers the benefit of a higher operating frequency than the QCM for sensing, it still suffers from the same pitfalls as the QCM because the electrodes are located in the area of highest sensitivity.

In a study by Woo Wai *et al.* focusing on non-inclined *c*-axis oriented ZnO, the thickness shear mode was excited through lateral field excitation [80]. The devices were

solidly mounted resonators fabricated through the use of a self-aligning process that involved ZnO liftoff and a spiral electrode structure spanning 2 mm in diameter. Operating close to 4.1 GHz, the devices illustrated the ability for ZnO FBARs to be operated at high frequencies with relative ease. However, an acoustic mirror was not implemented in the design, and the quality factor, Q, of the resonators was very low (roughly 35). Acoustic velocity calculations we made from the numbers given in the study come out to ~3,280 m/s as compared to a theoretical value of ~2,841 m/s calculated using bulk stiffness properties of ZnO available in Rosenbaum [17]. This value is reasonable considering variations in ZnO thin film material parameters.

4.2 Theoretical Analysis of the Thickness Shear Mode in *c*-axis ZnO

The process of designing a new acoustic device is aided by theoretical evidence that supports the feasibility of the desired mode of operation. The longitudinal mode of ZnO is very well studied, and the excitation of this mode is known to occur through thickness excitation of *c*-axis oriented ZnO. However, in this section we aim to explore the circumstances under which the thickness shear mode in *c*-axis oriented ZnO can be excited electrically, if at all. The results will provide insight into what types of acoustic waves are generated when a defined electric field is applied. By solving the equation with an arbitrary electric field, we can predict how an electric field oriented in any direction in the x-y plane of the crystal will affect the stress and strain in the crystal. For now, we will focus on *c*-axis oriented ZnO since this is the orientation of sputtered ZnO that is most easily grown with RF magnetron deposition. In a later section, evidence will be provided

to show that the ZnO grown in the Hunt lab has hexagonal symmetry and is well oriented in the *c*-axis orientation.

We begin the analysis by transforming the wave equation into an equation that is more directly useful for analytical calculations. To do this, we will consider a plane wave propagating through the medium in an arbitrary direction defined as the vector $\hat{\mathbf{l}} = l_x\hat{\mathbf{i}} + l_y\hat{\mathbf{j}} + l_z\hat{\mathbf{k}}$. The wave equation (Eq. 2.15) in its non-piezoelectric form can then be transformed using the gradient and divergence operator matrices discussed in Chapter 2. In three dimensions, particle displacement is directly related to time and space through the relationship:

$$\mathrm{u} = \mathrm{e}^{j(wt - k\hat{\mathrm{l}}\cdot\bar{\mathrm{r}})} \tag{4.1}$$

where $k = \omega / v_a$, and $\bar{\mathbf{r}} = x\hat{\mathbf{i}} + y\hat{\mathbf{j}} + z\hat{\mathbf{k}}$. The operation $\hat{\boldsymbol{l}} \cdot \bar{\boldsymbol{r}}$ results in the following expression from Eq. 4.1

$$\mathrm{e}^{j(wt - k\hat{\mathrm{l}}\cdot\bar{\mathrm{r}})} = \mathrm{e}^{j(wt - k(l_x x + l_y y + l_z z))} \tag{4.2}$$

which can be differentiated with respect to x to obtain

$$\frac{\partial}{\partial x}(\mathrm{e}^{j(wt - k\hat{\mathrm{l}}\cdot\bar{\mathrm{r}})}) = -jkl_x\mathrm{e}^{j(wt - k\hat{\mathrm{l}}\cdot\bar{\mathrm{r}})} = -jkl_x\mathrm{u} \tag{4.3}$$

Similar results are obtained for differentiation with respect to y and z. Starting with the non-piezoelectric form of the wave equation in Eq. 2.15, and utilizing the divergence and gradient matrix operator notation, we obtain a reduced equation

$$\nabla \cdot \mathbf{c} : \nabla_s \mathbf{u} = \rho \frac{\partial^2 \mathbf{u}}{\partial t^2} \longrightarrow \nabla_{iK} c_{KL} \nabla_{Lj} u_j = \rho \frac{\partial^2 u_i}{\partial t^2} \tag{4.4}$$

which requires summation over the dummy indices *j*, *K*, and *L*. Because of the differentiation required in using the divergence and gradient matrix operators, the

gradient of the particle displacement in Eq. 4.4 can be transformed using the gradient matrix operator to give

$$\nabla_{Lj}\mathbf{u} = \begin{bmatrix} \frac{\partial}{\partial x} & 0 & 0 \\ 0 & \frac{\partial}{\partial y} & 0 \\ 0 & 0 & \frac{\partial}{\partial z} \\ 0 & \frac{\partial}{\partial z} & \frac{\partial}{\partial y} \\ \frac{\partial}{\partial z} & 0 & \frac{\partial}{\partial x} \\ \frac{\partial}{\partial y} & \frac{\partial}{\partial x} & 0 \end{bmatrix} \mathbf{u} = -jk \begin{bmatrix} l_x & 0 & 0 \\ 0 & l_y & 0 \\ 0 & 0 & l_z \\ 0 & l_z & l_y \\ l_z & 0 & l_x \\ l_y & l_x & 0 \end{bmatrix} \mathbf{u} = -jkl_{Lj}u_j \tag{4.5}$$

where each component of the matrix described by l_{Lj} represent a propagation direction of the acoustic wave. Likewise the divergence operator becomes

$$\nabla_{iK} \longrightarrow -jk \begin{bmatrix} l_x & 0 & 0 & 0 & l_x & l_x \\ 0 & l_x & 0 & l_x & 0 & l_x \\ 0 & 0 & l_x & l_x & l_x & 0 \end{bmatrix} = -jkl_{iK} \tag{4.6}$$

Substituting these forms into Eq. 4.4, we reach a simple, and extremely useful equation called the non-piezoelectric Christoffel equation

$$k^2 l_{iK} c_{KL} l_{Lj} u_j = \rho \varpi^2 u_i \tag{4.7}$$

This equation accounts for material properties, particle displacement, and wave propagation direction in a single equation that is easily solvable as an eigenvalue problem. It is possible to solve the Christoffel equation to find the modes of propagation in the bulk given a defined electrical excitation direction. Note that the l_{Lj} matrix is simply the transpose of l_{iK}, and c_{KL} is the 6 x 6 material stiffness tensor rotated according to the desired Euler angles.

In *c*-axis oriented ZnO, the *c*-axis is oriented normal to the surface in a hexagonal crystal. To make things simple, we will arbitrarily choose to align the *z*-coordinate axis along this crystal axis for our calculations. For thickness shear mode propagation, wave propagation is then defined to be in the *z* direction, so l_x and l_y of the propagation vector become zero, and l_z becomes 1.

Equation 4.7 is used to solve for directions and velocities of bulk waves propagating in the substrate, but it does not account for the piezoelectric properties of a material, nor does it account for the possibility of the generation of these waves by an electric field. For this reason, we will turn to the piezoelectric form of the wave equation shown in Eq. 2.15. Converting into plane wave formalism, the equation becomes:

$$k^2 l_{iK} e_{Kj} l_j \varphi + k^2 l_{iK} c_{KL} l_{Lj} u_j = \rho \varpi^2 u_i \tag{4.8}$$

which is similar to Eq. 4.7 but now with the added piezoelectric coupling term. Assuming that the piezoelectric crystal is a dielectric material, then Gauss' law requires that:

$$\nabla \cdot \mathbf{D} = (\boldsymbol{\varepsilon}^S : \mathbf{E} + \mathbf{e} : \mathbf{S}) = 0 \tag{4.9}$$

which when converted to plane wave formalism becomes

$$-\nabla \cdot \boldsymbol{\varepsilon}^S : \nabla \varphi + \nabla \cdot \mathbf{e} : \nabla_S \mathbf{u} = 0 \rightarrow k^2 l_i \varepsilon_{ij} l_j \varphi - k^2 l_i e_{iL} l_{Lj} u_j = 0 \tag{4.10}$$

solving for φ in Eq. 4.10 and substituting the resulting expression into Eq. 4.8, gives the piezoelectric christoffel equation:

$$k^2 \left(l_{iK} \left(c_{KL}^E + \frac{(e_{Kj} m_j)(m_i e_{iL})}{m_i \varepsilon_{ij}^S m_j} \right) l_{Lj} \right) u_j = \rho \varpi^2 u_i \tag{4.11}$$

Where e_{Kj} is the piezoelectric coupling tensor, ε_{ij}^{S} is the 3x3 permittivity tensor at constant strain, m is the vector corresponding to external electric excitation field which is used to provide a clear differentiation from usage of *l* in the TE case. In TE, these vectors are oriented in the direction of acoustic propagation which is why the *l* vector is commonly used. However, for the LFE case, the vectors required are perpendicular to the acoustic propagation and therefore must be separate vectors. The c_{KL}^{E} term corresponds to the 6x6 stiffness tensor at a constant electric field. Upon inspection, Eq. 4.11 is similar to equation Eq. 4.8 except for inclusion of the term involving the piezoelectric and permittivity tensors, which is added to the stiffness tensor to apply piezoelectric "stiffening". The terms contained within the outermost set of parenthesis in Eq. 4.11 are known collectively as the stiffened Christoffel matrix. The Christoffel matrix is a 3 x 3 matrix whose elements depend on the propagation direction of the wave, the stiffness, permittivity, and coupling constants of the crystal, as well as the external electric field. Given any crystalline material, acoustic propagation direction, and external electric field, we can form the Christoffel matrix. Solving this matrix is an eigenvalue problem. The eigenvalues of the matrix are the three acoustic velocities of the possible propagating waves (one longitudinal, and two shear) while the eigenvectors correspond to the acoustic polarization or particle displacement directions.

For our analysis of the lateral field excitation of the *c*-axis oriented ZnO, we desire the electric excitation field to be orthogonal to the wave propagation. Therefore, if the wave propagation is in the direction of the *z*-axis, as we have defined it, the electric field is in the *x*-*y* plane. Here we will describe the coupling and acoustic wave

propagation for the general case of an electric field along any direction within the x-y plane. The electric field vector m_j is of the form

$$m_j = \begin{bmatrix} m_x \\ m_y \\ m_z \end{bmatrix} \tag{4.12}$$

Solving the piezoelectrically stiffened Christoffel equation for laterally excited ZnO, we set m_z=0 and $m_x^2 + m_y^2 = 1$. The *6mm* hexagonal system stiffness tensor is of the form

$$c = \begin{bmatrix} c_{11} & c_{12} & c_{13} & 0 & 0 & 0 \\ c_{12} & c_{11} & c_{13} & 0 & 0 & 0 \\ c_{13} & c_{13} & c_{33} & 0 & 0 & 0 \\ 0 & 0 & 0 & c_{44} & 0 & 0 \\ 0 & 0 & 0 & 0 & c_{44} & 0 \\ 0 & 0 & 0 & 0 & 0 & c_{66} \end{bmatrix} \tag{4.13}$$

and the form of the piezoelectric matrix is

$$e = \begin{bmatrix} 0 & 0 & 0 & 0 & e_{15} & 0 \\ 0 & 0 & 0 & e_{15} & 0 & 0 \\ e_{31} & e_{31} & e_{33} & 0 & 0 & 0 \end{bmatrix} \tag{4.14}$$

The resulting Christoffel Matrix is of the form

$$\Gamma = \begin{bmatrix} c_{44} + \dfrac{e_{15}^2 m_x^2}{\varepsilon_{11}} & \dfrac{e_{15}^2 m_x m_y}{\varepsilon_{11}} & 0 \\ \dfrac{e_{15}^2 m_x m_y}{\varepsilon_{11}} & c_{44} + \dfrac{e_{15}^2 m_y^2}{\varepsilon_{11}} & 0 \\ 0 & 0 & c_{33} \end{bmatrix} \tag{4.15}$$

The eigenvalues of this matrix correspond to terms that can be used to solve for v_a, the acoustic velocity in each of the three wave propagation modes, while the corresponding

eigenvectors relate to the direction of particle displacement. Solving for the eigenvectors and eigenvalues of Γ gives

$$x_1 = \begin{bmatrix} -m_y \\ m_x \\ 0 \end{bmatrix}, \lambda_1 = c_{44} \quad x_2 = \begin{bmatrix} m_x \\ m_y \\ 0 \end{bmatrix}, \lambda_2 = c_{44} + \frac{e_{15}^2}{\varepsilon_{11}} \quad x_3 = \begin{bmatrix} 0 \\ 0 \\ 1 \end{bmatrix}, \lambda_3 = c_{33} \tag{4.16}$$

From these results, we find that only one mode is piezoelectrically excited (defined by x_2 and λ_2) and that the particle displacement will be directly aligned with the electric field, regardless of the orientation of the field with respect to the *x*-*y* plane. This mode is a pure shear thickness mode and is the mode we seek. Another pure shear mode exists (defined by x_1 and λ_1) with particle displacement also in the *x*-*y* plane at an angle perpendicular to that of the piezoelectrically excited mode, however it is piezoelectrically inactive. The longitudinal mode (defined by x_3 and λ_3), importantly, is also piezoelectrically inactive. These results indicate that an electric field in the *x*-*y* plane will excite a pure shear thickness mode with particle displacement aligned with the electric field. The acoustic velocity for this mode can be calculated from Eq. (4.16):

$$v_a = \sqrt{\frac{c_{44} + \frac{e_{15}^2}{\varepsilon_{11}}}{\rho}} \tag{4.17}$$

Using bulk values for ZnO from Rosenbaum,[17] e_{15} = -0.48, c_{44} = 43x10^9 N/m^2, ε_{11} = 8.6 (rel.), ρ=5,700 kg/m^3, the theoretical acoustic velocity for the piezoelectrically stiffened thickness shear mode is approximately 2,841 m/s. Since most ZnO thin films include various dopants and are not of pure crystal uniformity, they will have stiffness, density, and piezoelectric constants that are different from these bulk values. This calculated acoustic velocity is therefore an approximate figure and not an absolute value

from which to evaluate an experimentally obtained mode. The theoretical piezoelectric coupling constant for the ZnO LFE resonator is given by

$$K^2 = \frac{e_{15}^2}{c_{44}\varepsilon_{11}} \tag{4.18}$$

Which is calculated to be approximately 0.07 or 7% for the case of the thickness shear mode.

All of the above calculations rely upon the assumption that the lateral excitation field is aligned in the *x*-*y* plane. Therefore, it is important to verify that a given electrode structure generates an electric field consisting of a primarily lateral component. To accomplish this, the electromagnetics module of the Comsol Multiphysics® finite element modeling software package was used to evaluate the electrode configuration.

4.3 Finite Element Modeling Results

The starting point for exploring the lateral field excitation of ZnO is to first develop a simple finite element model in which the electric field orientation is calculated and analyzed. This will aid in the evaluation and identification of LFE electrode configurations that are capable of generating the plane-parallel electric field that is required for TSM excitation. In this study, a variety of electrode configurations have been investigated and the results have been compared in both 2-D and 3-D using the Comsol Multiphysics software. Modeling was performed with the same methods as those outlined in Chapter 3. The stiffness, piezoelectric, and permittivity tensor values for bulk ZnO were used in the modeling process to accurately describe the substrate layer as piezoelectric *c*-axis oriented ZnO. Finite element analysis of the electric fields was performed using the Electromagnetics module. Adaptive meshing was performed so that

areas near the features of interest contained a high density mesh while areas away from the active regions had a lower density mesh. This was necessary because of the matrix size and computation time required to solve a large, densely meshed 3-D model. By increasing the elements size outside of the active region, the overall number of degrees of freedom and the total computation time was reduced.

Figure 4.1(a) illustrates the mesh of a 3-D model developed with two straight plane-parallel electrodes on top of a ZnO thin-film. Figure 4.1(b) shows the geometry of a circular electrode model which consists of two pairs of circular electrodes sandwiched on either side of the ZnO bulk material. The theory behind this configuration is that the electric field (e-field) generated between the electrodes in each pair would have horizontal components that would add together, while the vertical e-field components that would be equal and opposite resulting in cancellation in the vertical direction. This would result in an entirely laterally oriented electric field within the volume located between the gaps in the electrodes. Calculations performed for determining the location of electrical energy density show that the volume in-between the electrode gaps contain the majority of the energy. A plot of the electrical energy density is shown in Figure 4.2 where one electrode was defined at a positive potential, and the other held at ground.

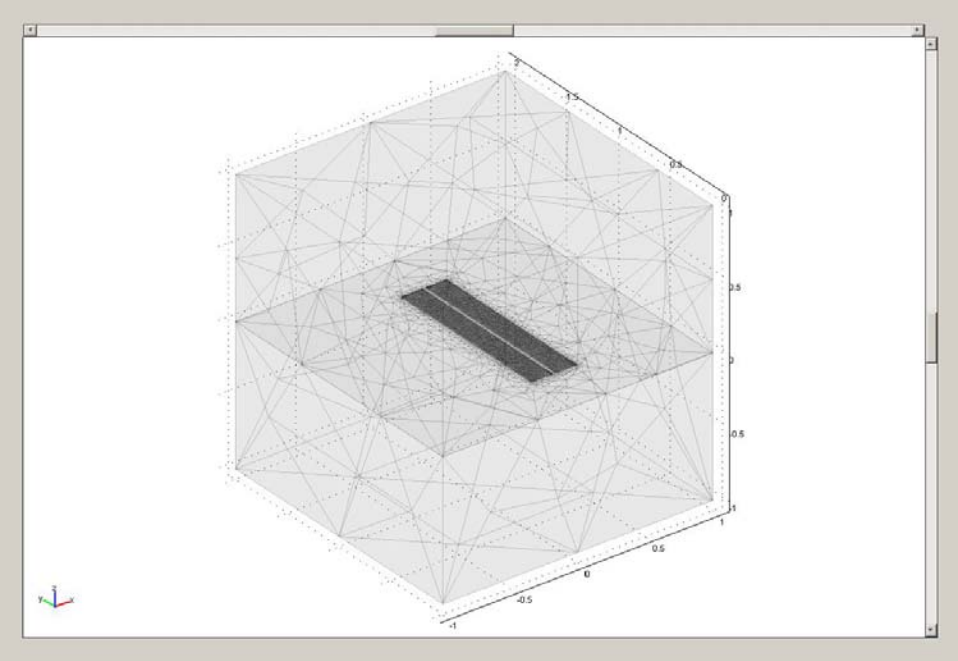

a)

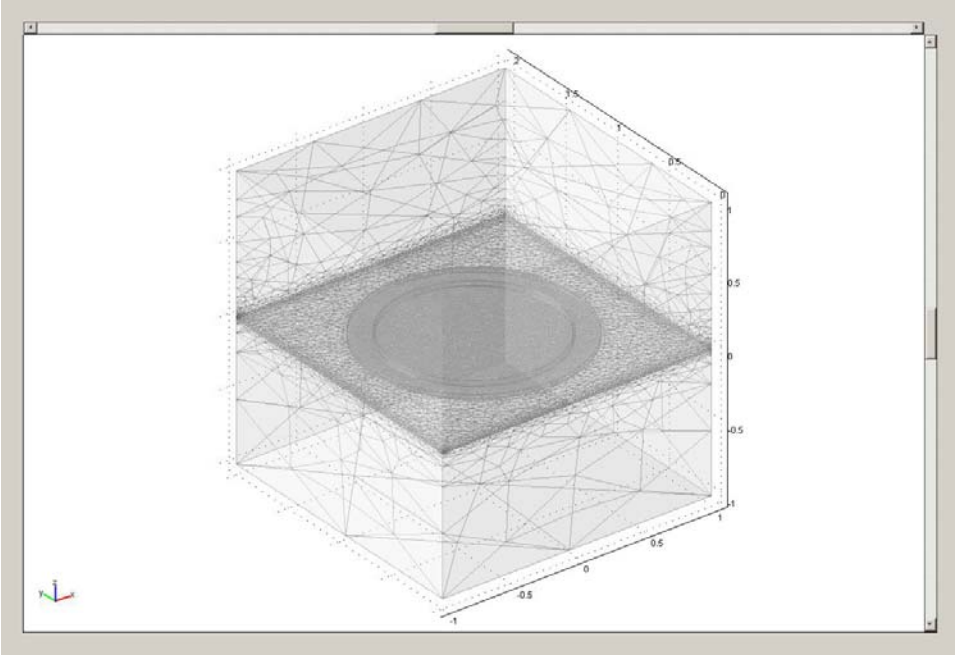

b)

Figure 4.1 Meshes of FEM model geometries (a) rectangular electrodes with a width: 15 µm, length: 125 µm, gap: 3 µm and ZnO below (b) circular electrodes on top and bottom with outside electrode width: 30 µm and gap: 3 µm. The thin film between electrode pairs was modeled as ZnO and the areas above and below were modeled as free space.

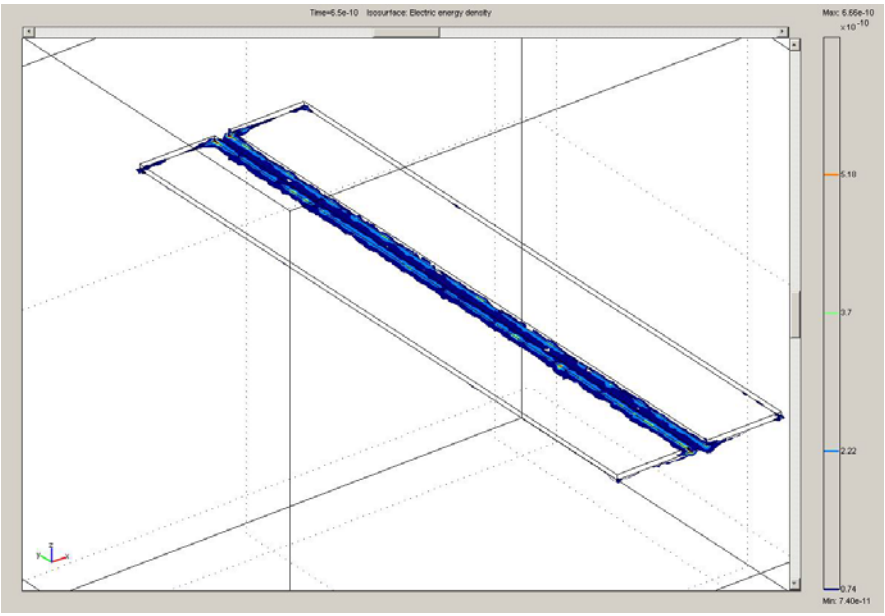

Figure 4.2 A 3-D electrical energy density plot for the electrode configuration depicted in Fig 4.1(a). The plot illustrates the energy density as a series of concentric isosurfaces. The energy density is located primarily between the electrodes within the ZnO substrate.

Similar results for the location of greatest electrical energy density were obtained for the double-sided circular electrode configuration. Based on these results, this area of high energy density is the location of greatest piezoelectric excitation in the ZnO crystal lattice. This region is expected to have the greatest particle displacement and therefore the greatest sensitivity to perturbation. As will be discussed later in Chapter 5, this surface region in between the electrodes is the target for the immobilization of antibodies.

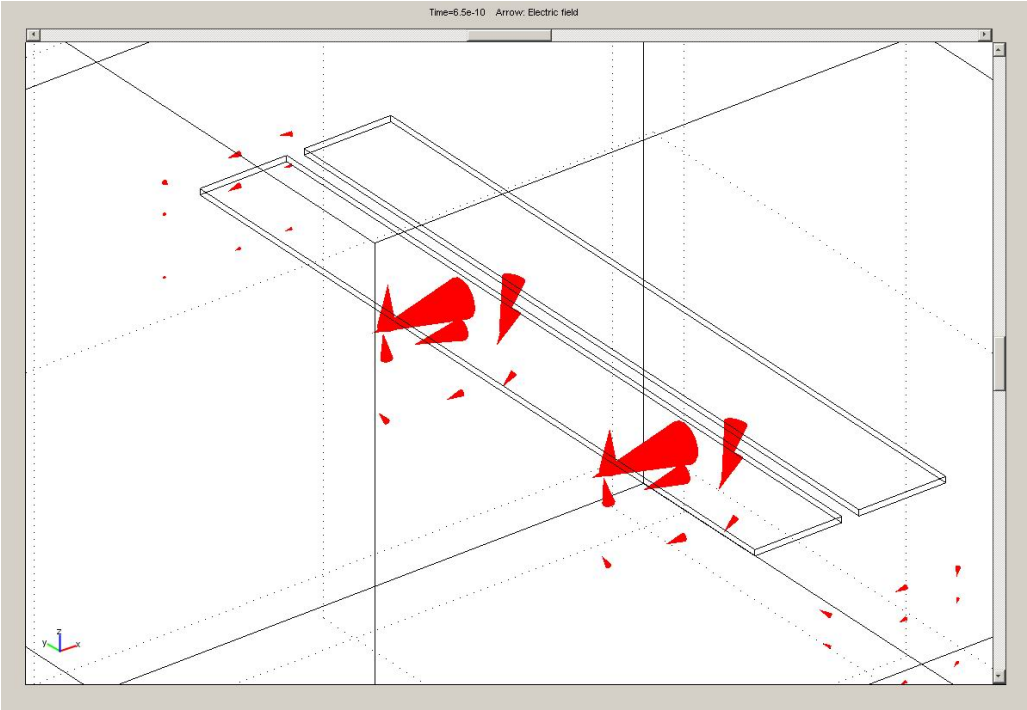

Figure 4.3 An arrow plot of the electric field orientation for rectangular electrodes modeled on a ZnO substrate half-space. The arrow size is related to the e-field strength and the direction of the arrow points in the direction of the e-field as determined at the center of the tail of the arrow.

While the energy density plots are important for elucidating the area of greatest sensitivity given plane-parallel electrodes, they do not give any information about the direction of the electric field within the volumes in-between the electrodes. For this, calculation of the electric field vectors was performed. A 3-D arrow plot of the vector field for the single-sided rectangular electrode configuration is shown in Figure 4.3. The size of the arrows is directly related to the strength of the electric field at the point located at the center of the tail. The direction that the arrow is pointing corresponds to the orientation of the vector electric-field at the particular point. The plot shows that the e-field in the ZnO substrate is oriented horizontally in the region directly in-between the electrodes. The electric field strength dies away with increasing distance from the

electrodes through the thickness of the ZnO. Directly below the center of the electrodes, the electric field has a large vertical component, indicating that the ZnO is not being excited solely through lateral field excitation and that the ZnO below is being excited with a thickness excitation field. Therefore, the assumptions made in the calculations in the previous section regarding a lateral field are no longer valid for this region of the ZnO, and the thickness excitation of a longitudinal wave is an expected outcome.

The electric field plots generated for the double-sided electrode configuration shown in Figure 4.4 depict a similar result to Figure 4.3 throughout the region in the gap between the electrodes. In this model, one set of adjacent top and bottom electrodes sandwiching the thin-film are held at ground while the other set of adjacent top and bottom electrodes are held at an arbitrary positive potential. The biggest difference between the electric field orientation derived by single vs. double-sided electrode configurations is that the electric field in-between the top and bottom electrodes is negligible in the double-sided case. The absence of the arrows directly between the electrodes is not because the e-field was not calculated at these points. Rather, it is because the magnitude of the e-field is so small at those points that they appear non-existent. However, it is evident from Figure 4.3 that a pair of plane-parallel electrodes produces an e-field below the electrode that is almost entirely vertically oriented. The absence of the electric field in this region of the ZnO for the double-sided configuration confirms the hypothesis that the vertical components of the electric field cancel out.

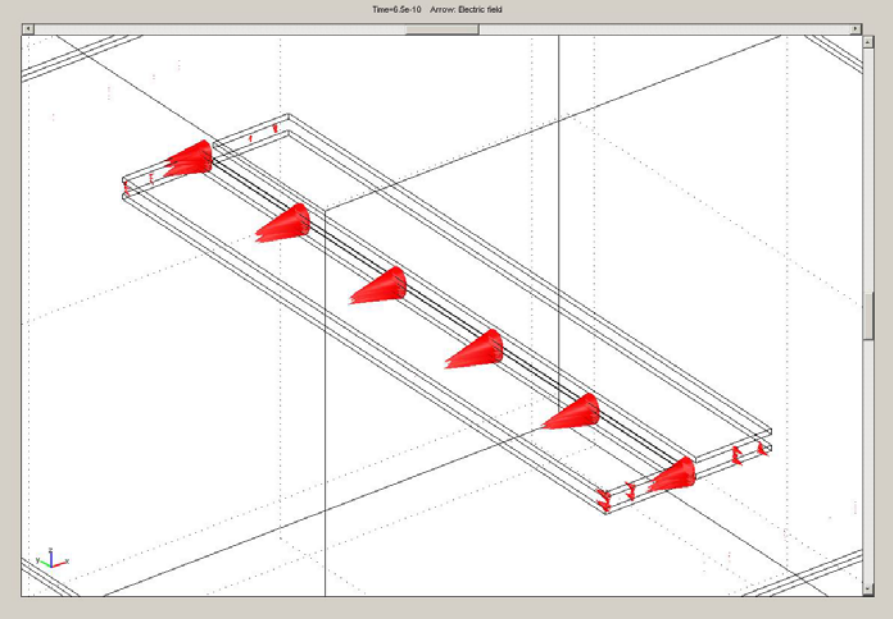

Figure 4.4 An arrow plot of the electric field orientation for double-sided rectangular electrodes on either side of a ZnO thin-film when top and bottom electrodes on left are held at ground and the electrodes on the right are held at a positive potential. The arrow size is related to the e-field strength and the direction of the arrow points in the direction of the e-field as determined at the center of the tail of the arrow.

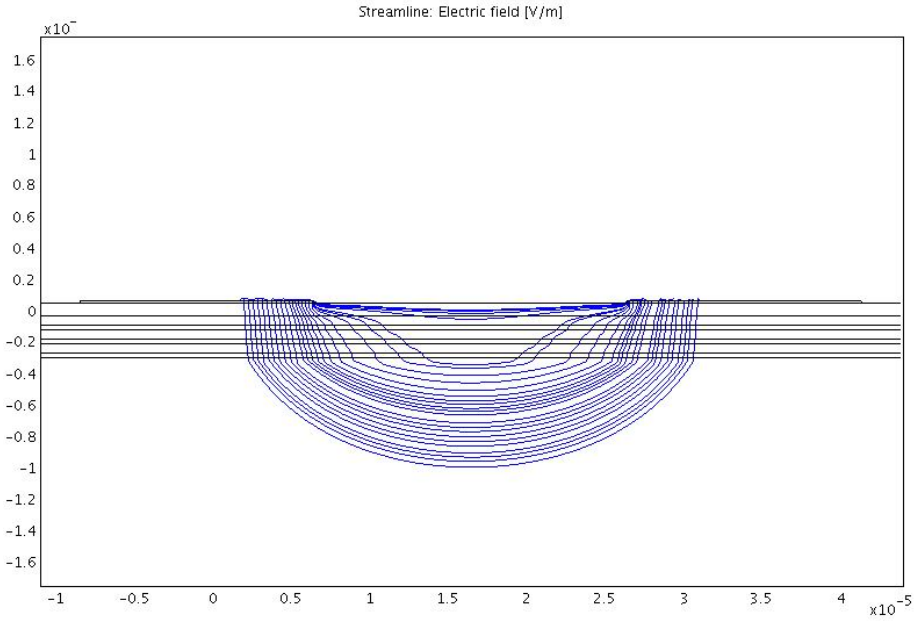

Figure 4.5 Finite element simulation plot illustrating the electric field streamlines resulting from a 20 µm electrode gap. The model consists of electrodes located at the surface of a ZnO thin-film. Below the ZnO is an acoustic mirror consisting of alternating layers of SiO_2 and W followed by the Si substrate.

To further explore the electric field as a result of various electrode configurations and gap sizes, 2-D models were developed. It is hypothesized that a larger gap width between the electrodes would tend to "pull" the electric field in a more horizontal orientation through the thickness of the ZnO leading to more efficient excitation of the thickness shear mode. Figure 4.5 shows a streamline plot of the electric field lines produced from the simple electrode geometry with a gap of 20 μm in 2-D. The top layer just below the electrodes is defined as ZnO, followed by alternating layers of SiO_2 and W. These layers are included in the model to simulate an acoustic mirror for visualization of the electric fields within these layers. As will be discussed in a later section, the acoustic mirror is a very important component of solidly mounted resonators. The e-field streamlines in the gap between the electrodes are mostly oriented horizontally through the ZnO thin-film. This visualization helps to confirm that planar electrodes located on the surface of the ZnO provide a laterally oriented field in-between the electrodes. While the streamlines visualize the orientation of the electric field lines, they offer no information about the strength of the vector field. Figure 4.6 provides an image of the electric field produced by the 20 μm gap depicted with an arrow plot which illustrates the direction (orientation of arrow) and relative intensity of the electric field (size of arrow) in the ZnO. The plots illustrate that the electric field is aligned parallel to the surface in the area between the gaps. However, in the area directly below the electrodes it is aligned primarily normal to the surface. The relative sizes of the arrows from Fig. 4.6 show that the strength of the electric field within the electrode gap is approximately twice that of the electric field directly beneath the electrodes. These plots indicate that the electric field generated by the proposed electrode configuration is laterally oriented in the active area

of the device which is a requisite for lateral field excitation. Further, the results indicate that a weak response due to thickness excitation of the longitudinal mode should be expected in a practical realization of this device.

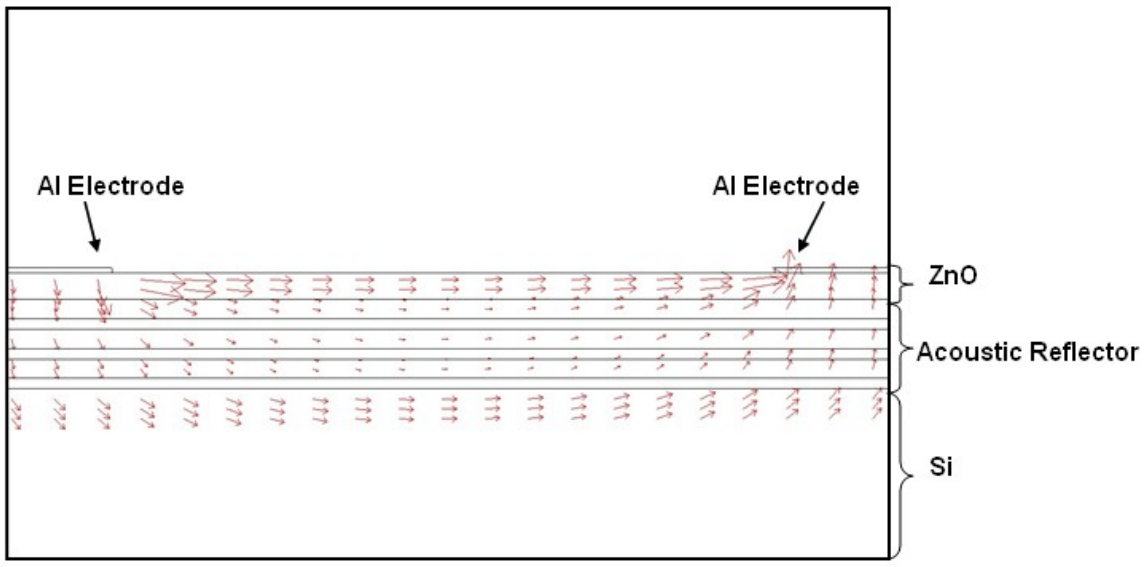

Figure 4.6 An arrow plot of the electrode configuration from Fig. 4.5 in which the electric field direction is indicated by the direction of the arrow and the relative strength of the electric field (C/m) is indicated by the size of the arrow.

In addition to investigating the electric fields generated by electrodes located at the boundaries above and below the ZnO thin-film, an entirely different configuration was also investigated. This configuration involves a ZnO "slab" which is a segment of crystalline ZnO onto which electrodes are deposited on the sidewalls. The configuration is similar to a parallel-plate capacitor in which the dielectric in between the electrodes is the ZnO slab. Applying a time varying-potential to the electrodes will generate an electric field through the width of the ZnO. With *c*-axis oriented ZnO, this laterally oriented electric field should generate a TSM wave.

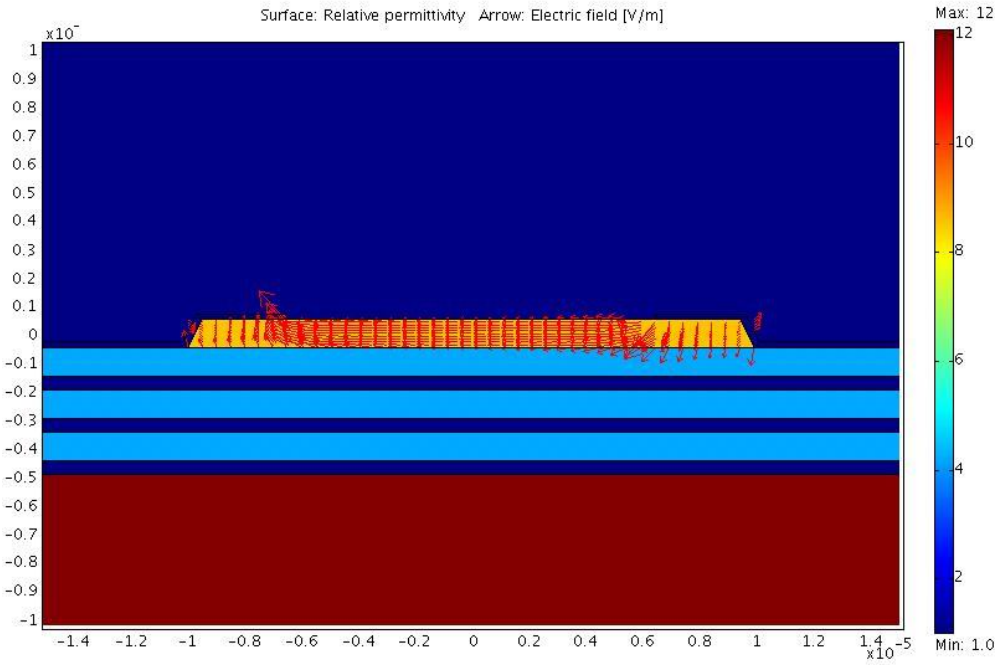

Figure 4.7 Arrow plot of the electric field generated by electrodes located on the sidewalls of the ZnO "slab"

Figure 4.7 provides insight into the electric field that would be generated by electrodes located on the sidewalls of a ZnO slab when one is held at ground while the other is held at an arbitrary potential. The colors in the image indicate the different relative permittivities of the materials used in the model. The acoustic mirror located below the ZnO slab (yellow) is comprised of alternating layers of SiO_2 (light blue) and W (dark blue). Aluminum electrodes (dark blue) are located on the angled walls of the ZnO, and the entire structure is set on a Si substrate (red). The arrows indicate that the electric field through the width of the ZnO is highly laterally oriented. However, near the edges of the electrodes, fringing effects cause the electric field to have a vertical component.

The results from performing static electric field modeling indicate that there are multiple different electrode configurations that are capable of adequately generating a

laterally oriented field through the ZnO. However, the modeling results presented here are nothing more than calculations made based on a mathematical model and are useful only for providing insight into the actual physical workings of a device. True understanding and exploration of a device can only be obtained through experimentation. For this reason, a variety of electrode configurations and gap sizes have been explored experimentally in order to find the best combination for generating a TSM resonant acoustic device. The results of the experimental device operation based on the various configurations are discussed in the subsequent section.

To confirm the results from the Christoffel equation calculations outlined in section 4.3 and explore the excitation of a TSM mode in ZnO, finite element analysis was performed. Similar to the model developed with the QCM, the analysis was performed using the Piezo_solid application mode. This application mode implements the principle of virtual work and allows the user to set all material properties including stiffness tensors, permittivity tensors, coupling tensors, and density. The multiphysics capability of the software allows the user to incorporate both the electromagnetics and the structural mechanics into the model. The resulting model is, physically, an accurate description of the piezoelectric ZnO. Excitation of this piezoelectric material with simulated electrode configurations such as those discussed previously should elicit the acoustic modes and particle displacements that result from an applied time-varying electric field.

The model was developed in 2-D because it drastically reduces the computation time required for solving the model. The model consists of a 1.2 μm-thick ZnO film with two pairs of electrodes located on the top and bottom surfaces of the ZnO. The electrodes are separated by a gap of 3 μm. The electrode material is aluminum, and the thickness of

each electrode is 120 nm which is a typical thickness for electrodes in standard piezoelectric resonators. In the QCM model discussed in Chapter 3, the electrodes were simulated without mass or volume in order to simplify the model and reduce the computation power required. However, the absence of mass in the locations where particle displacement exists is an oversimplification of the physical system. In an actual resonator, metallic electrodes provide damping of the system because of acoustic losses in the material. In this model, damping due to the presence of electrodes is accounted for which improves the accuracy of the model. Experimentally, the fabrication of the TSM devices is carried out through the SMR configuration. However, in the model, the areas above and below the ZnO thin-film are defined as free-space in order to approximate the ideal resonator case in which the boundaries are free. While this is an oversimplification of what will be experimentally fabricated, the purpose of the model is not to predict the resonant frequency of a particular device nor the maximum particle displacement. Rather, it is meant to simply confirm that a TSM wave can be excited in *c*-axis oriented ZnO through lateral field excitation.

The lateral field is generated by applying ground to the top and bottom electrodes located on one side of the gap, while a time varying voltage is applied to the top and bottom electrodes on the other side of the gap similar to the electrode configuration shown in Figure 4.4. The results were simulated with a time-dependent solver which allows the user to look at the parameter of interest such as x-displacement in a stepwise manner over the time interval of interest. Simple videos were assembled which visualize the parameter of interest as a function of time.

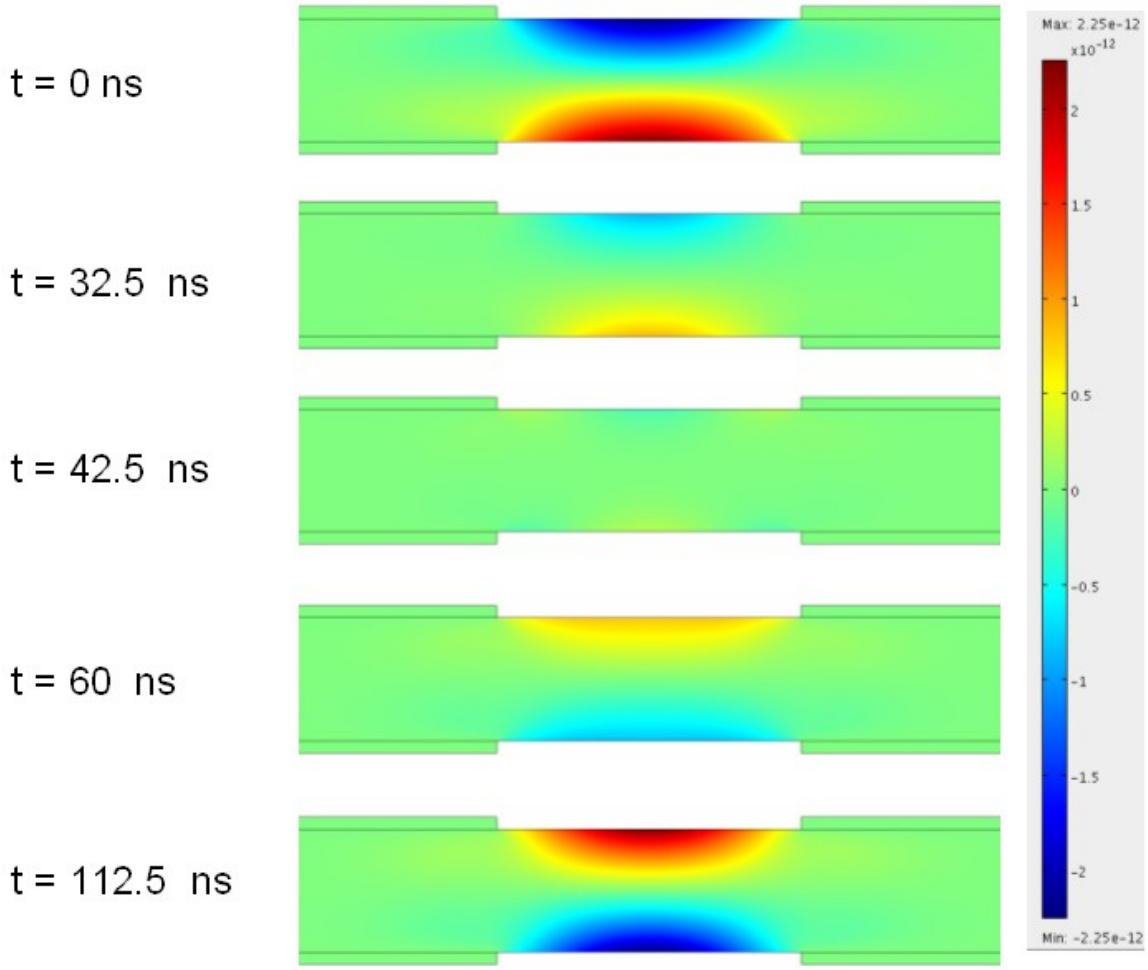

Figure 4.8 Visualization of the x-displacement (shear displacement) of ZnO particles when excited with a laterally oriented electric field. The sequence shows the system at various time steps throughout the period of the wave. The dark blue illustrates particle displacement to the left while the red illustrates particle displacement to the right. This is evidence of the fundamental harmonic of a thickness shear mode in ZnO.

Figure 4.8 is a sequence of images which illustrates the maximum particle displacement in the x-direction for an acoustic wave that is generated from a lateral electric field. The first image (t = 0 ns) shows that a shearing mode is excited - particles in the top half of the ZnO thin-film possess a displacement that is directed towards the left, while the particles in the lower-half possess a displacement that is directed towards the right. As time progresses and the phase of the excitation frequency changes, we see these particle displacements reduce in magnitude (t = 32.5 ns), and then switch direction

such that the particles in the top half of the ZnO thin-film possess an x-displacement vector directed towards the right, and the lower-half particles have an opposite polarization. This sequence repeats itself and seems to track the excitation frequency. This is evidence of a periodic thickness shear wave where the particle displacement vectors vary sinusoidally through the thickness of the ZnO film. This is precisely what the theoretical analysis of the Christoffel equation predicts.

The results obtained from the finite element analysis are useful mainly in two ways. First, they provide insight into the orientation of the electric field that is produced by a variety of electrode configurations and help to identify those that are capable of producing a laterally oriented field. Second, they help to confirm the results derived through analysis of the Christoffel equation that the thickness shear mode can be excited electrically through lateral field excitation in *c*-axis oriented ZnO. These results give confidence in moving forward in the development of novel acoustic sensors based on the excitation of the TSM mode in ZnO, and will help to guide electrode configuration choices to meet this goal.

4.4 Solidly Mounted Resonator Configuration

One of the challenges to developing a BAW resonator based on a piezoelectric thin-film lies in maximizing the Q of the device while still maintaining a physically robust sensor with a simple fabrication procedure. Mechanical resonance in a device requires isolation from absorption in the surrounding media so that a large standing wave can build in the piezoelectric film. As a result, the physical mounting or support of an acoustic resonator is an important consideration in the development of high Q resonators.

Excellent energy trapping can be achieved in resonators whose surfaces are open to air or vacuum because the zero or near-zero acoustic impedance of the air causes an incident acoustic wave to be reflected back into the piezoelectric substrate. The QCM is a BAW resonator which can achieve Q factors well in the tens of thousands. The QCM is made from a quartz plate which has completely free surfaces except for small wire electrodes contacting the edges of the crystal. This setup allows for very little acoustic absorption which translates into high Q. However, thin-film acoustic resonators cannot be mounted in this manner, and therefore require other techniques for achieving acoustic isolation.

Figure 4.9 illustrates three of the configurations through which acoustic isolation can be achieved with thin-film BAW resonators. The first configuration shown in Figure 4.9(a) is a membrane-type structure in which the piezoelectric thin-film is supported by the solid substrate, typically a Si wafer. The piezoelectric layer (piezo layer) is deposited onto the substrate which is then etched from the backside until the piezoelectric substrate is reached. This leaves a thin membrane of the piezo layer that spans a gap in the silicon substrate resulting in low impedance material interfaces of air. The electrodes can be deposited before or after etching the substrate to create the desired excitation field. This process requires that the piezo layer be semi-resistant to the etchant solution so that the etch can be stopped just before the piezo layer is degraded. This poses a considerable challenge with a material like ZnO which is extremely susceptible to etching even in weakly acidic solutions. Further, strain in the membrane can lead to breakage. As a result, this configuration is not ideal for applications that require rugged sensors.

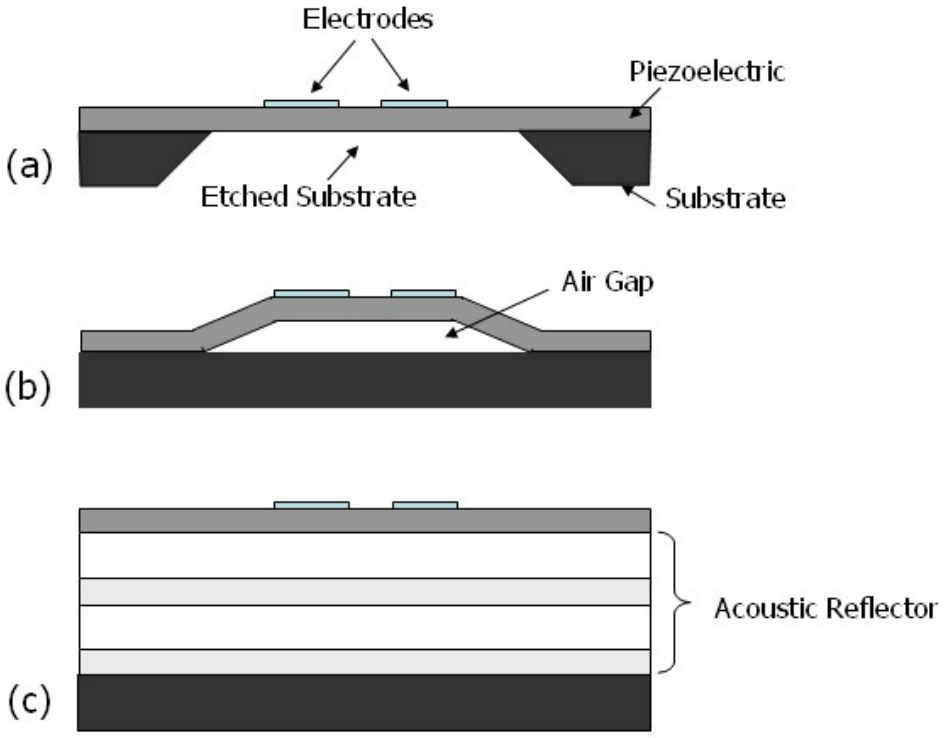

Figure 4.9 Thin-film resonator configurations. (a) A Membrane configuration, (b) an air gap resonator, and (c) a solidly mounted resonator implementing an acoustic reflector

The configuration shown in Figure 4.9(b) takes a different approach than the membrane configuration to accomplish the goal of having air interfaces on both sides of the piezo layer in order to trap the acoustic energy. This configuration is typically fabricated by depositing and patterning a sacrificial layer. Then, the piezo layer is deposited on top of the sacrificial layer along with the electrodes. Finally, the sacrificial layer is removed from the underside of the piezo layer leaving an air gap below. This method requires that the piezo layer form a continuous film so that the structure is supported after removal of the sacrificial layer. Strain in the piezo layer can cause the membrane to warp and rest upon the substrate or rupture giving rise to uncertain resonator performance [81].

In sensor applications where ruggedness is required, the membrane and air-gap configurations may not provide sufficient robustness - especially under fluidic flow conditions. An alternative to these configurations is the SMR which is illustrated in Figure 4.9(c). The SMR configuration was first described by Newel [82], and was later further developed by Lakin [81, 83]. This configuration allows the piezo film to be deposited directly onto a solid substrate while still providing acoustic isolation. This is accomplished through the use of an acoustic reflector which is composed of alternating quarter-wavelength high and low acoustic impedance materials. The acoustic reflector effectively transforms the acoustic impedance of the substrate (ie. a Si wafer) into a favorable value which approximates an air boundary and provides acoustic energy trapping within the piezo layer.

4.4.1 Basic SMR Theory

The theory behind the SMR configuration makes use of transmission line theory to describing an acoustic wave propagating in a solid medium. In order to explain the process of designing an acoustic mirror for the ZnO sensors, a brief treatment of the theory is provided to explore the conditions under which the alternating layers comprising the stack act as a reflector and when they act as an absorptive structure.

First, we consider the impedance seen by an acoustic wave arriving at a boundary beyond which is a layer or structure that will be modeled as a transmission line. The impedance seen by the acoustic wave (Z_{in}) looking into the transmission line of length d_n, with characteristic acoustic impedance Z_n when the other end of the transmission line is terminated by an impedance Z_{n-1} is given by [81]

$$Z_{in} = Z_n \frac{Z_{n-1}\cos(\frac{2\pi}{\lambda_n} d_n) + jZ_n \sin(\frac{2\pi}{\lambda_n} d_n)}{Z_n \cos(\frac{2\pi}{\lambda_n} d_n) + jZ_{n-1} \sin(\frac{2\pi}{\lambda_n} d_n)} \tag{4.11}$$

where λ_n is the acoustic wavelength in the material of interest and Z_n is given by the equation

$$Z_n = \sqrt{\rho_n c_n} \tag{4.12}$$

where ρ_n is the mass density and c_n is the stiffness constant in the material for the type of wave, either shear or longitudinal. At the frequency where the length of the transmission line is λ/4, Eq. 4.11 reduces to

$$Z_{in} = Z_n \left(\frac{Z_n}{Z_{n-1}} \right) \tag{4.13}$$

This result indicates that the acoustic impedance seen by an acoustic wave at one end of a λ/4-thick layer is related to the ratio of the acoustic impedance of the layer to the impedance at the other end of the layer. If a stack of alternating low and high impedance layers are deposited on a Si wafer in a manner similar to the drawing shown in Figure 4.10, the input impedance seen by the acoustic wave becomes:

$$Z_{in} = Z_L \cdot \frac{Z_L}{Z_H} \cdot \frac{Z_L}{Z_H} \cdot \frac{Z_L}{Z_H} \cdot \frac{Z_{Si}}{Z_H} \tag{4.14}$$

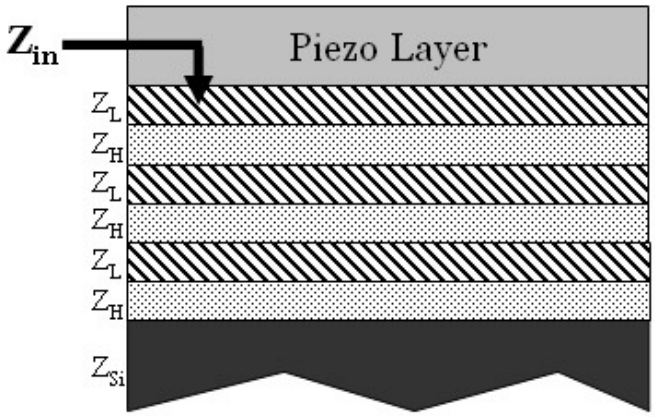

Figure 4.10 A 6-layer acoustic reflector stack with alternating layers of high and low impedance materials.

If Z_L is much less than Z_H, then the ratio of Z_L to Z_H is less than one and the input impedance seen by the acoustic wave will go towards zero as the number of pairs of high and low impedance layers is increased. As a result, the piezo layer becomes isolated from the Si substrate at the appropriate operating frequency (f_0), and the acoustic energy will be reflected back into the piezo layer. It is desirable to use materials for the acoustic reflector that have as high an acoustic impedance mismatch as possible. This will allow for fewer layers to be used to achieve the same desired impedance profile at f_0.

Equation 4.14 describes the impedance when the acoustic reflector film thicknesses are λ/4. The fabrication of a reflector stack for a specific resonance requires that the thickness of the layers in the reflector be fixed based upon f_0 and the acoustic velocity within the film. However, it is often the case that an acoustic resonator will not resonate exactly at the desired frequency, rather at a slightly shifted frequency due to slight inconsistencies in the fabrication process. This occurs most typically as a result of variation in the thickness of the layers deposited by RF sputtering.

Because of the often unavoidable difference between the desired operating frequency and the actual frequency of operation, it is important to know how the impedance of the acoustic reflector will behave over a wide range of frequencies. Ideally, the reflector will have an acoustic impedance that is nearly that of air over a wide frequency band so that variation in the resonant frequency will not have an affect on device performance. To assess the theoretical reflectance of an acoustic mirror, a script was written in Matlab to implement Equation 4.11 and provide a method for comparing various acoustic reflector configurations. One version of the script allows the user to define the material properties, the desired center frequency of operation, and the number of layers for the acoustic reflector. The code recursively implements the impedance calculation starting with the impedance of the substrate and then calculates the input impedance with each additional layer until the last is reached. The script outputs the suggested acoustic layer thicknesses to obtain the desired center frequency based on the material properties as well as the impedance characteristics over the range of frequencies defined by the user.

Another version of the script allows the user to define the acoustic reflector layer thicknesses and material properties. The output is the theoretical frequency response for the acoustic mirror. This script is useful for analyzing an experimentally fabricated acoustic reflector using actual layer thicknesses obtained through SEM imaging of the wafer cross-section.

The script was used to simulate the bandwidth for a variety of mirror materials in order to aid in the selection of materials for use in the acoustic reflector. SiO_2 was chosen

for the low impedance material because it has a low acoustic impedance ~ 1.2 x 10^7 kg/m^2s and we have the capability to deposit this material in our labs quite readily.

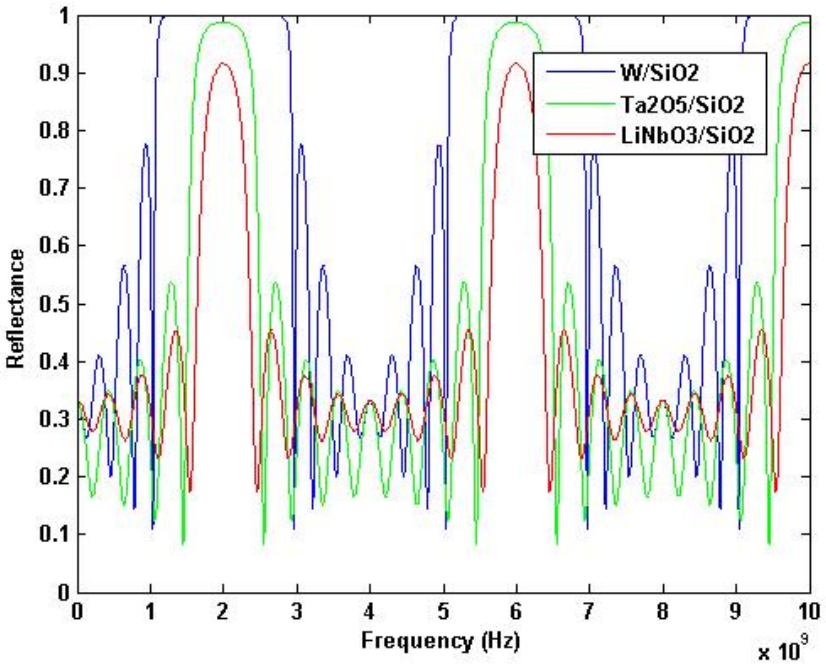

Figure 4.11 Simulated frequency response for acoustic mirrors comprised of $LiNbO_3/SiO_2$, W/SiO_2, and Ta_2O_5/SiO_2.

The simulation was performed to compare acoustic reflectors employing SiO_2 with another high acoustic impedance material. Figure 4.11 shows the theoretical responses of three different eight-layer mirrors: $LiNbO_3/SiO_2$ (Lithium Niobate and Silicon Dioxide), W/SiO_2 (Tungsten and Silicon Dioxide), and Ta_2O_5/SiO_2 (Tantalum Pentoxide and Silicon Dioxide). The results indicate that the acoustic mirror combination of W/SiO_2 provides a reflection coefficient that is 1, or nearly 1, over a much wider bandwidth than the other two mirror combinations. The W/SiO_2 acoustic reflector should approximate an air boundary over the approximate frequency range of 1.2 GHz to 2.8 GHz. The Ta_2O_5/SiO_2 mirror performs much more poorly offering a reflection coefficient nearing 1 only in the frequency range of 1.9 GHz to 2.1 GHz with an 8-layer mirror. The poorest

performer of the three mirror combinations is the $LiNbO_3/SiO_2$ which doesn't even approach a reflection coefficient of 1 throughout the frequency band with an 8-layer mirror.

These results can be partially explained by the ratio of the acoustic impedances of these mirror combinations. From Equation 4.14, we see that as the ratio of Z_H/Z_L increases, the equivalent impedance decreases. For a shear mode, the combination of W/SiO_2 has an impedance ratio of approximately 4.5 while the Ta_2O_5/SiO_2, and $LiNbO_3/SiO_2$ ratios are 1.72 and 1.35, respectively. The difference in the acoustic impedances between W and SiO_2 allows for the large reduction of the input impedance even over a wide range of frequencies.

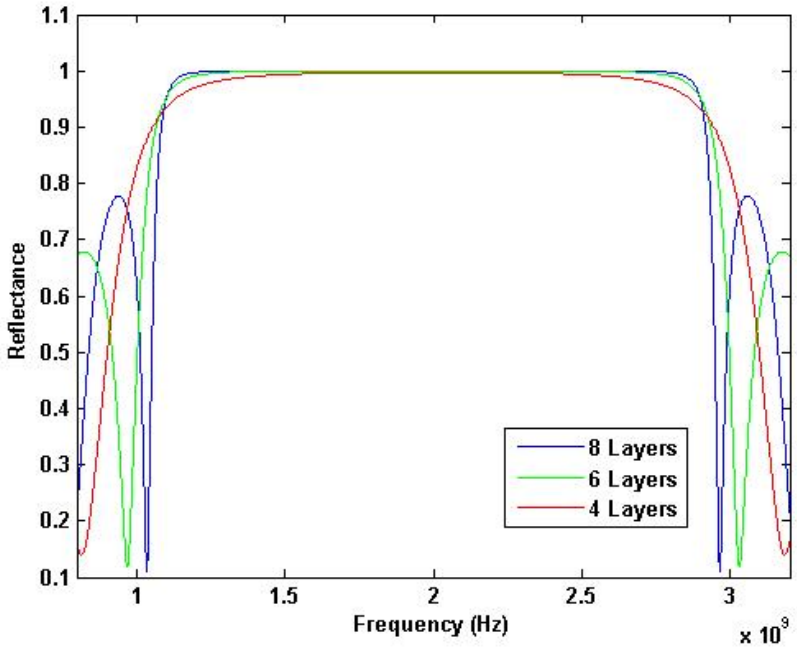

Figure 4.12 Acoustic reflector simulations of a W/SiO_2 stack illustrating the effects of increasing the number of layers on the frequency response surrounding the center frequency of 2 GHz

To better understand how the number of high and low impedance pairs in an acoustic reflector affects its frequency response, simulations were performed to

characterize reflectors with an increasing number of W/SiO_2 pairs. Figure 4.12 shows the results from such a simulation focusing on the frequency band immediately surrounding the center frequency. As the number of layers increases, the bandwidth of reflectance increases. However, the drop-off in reflectance also becomes more drastic. This means that with an 8-layer mirror there is a wider range of frequencies over which the reflector approximates air, however just outside that frequency band, the mirror becomes absorptive rather abruptly. With 6 layers, the acoustic mirror approximates air over a smaller bandwidth than the 8-layer mirror, but the transition from maximum reflectance to minimum reflectance is larger.

The difference between 4, 6, and 8 layer mirrors becomes much more significant with acoustic reflectors comprised of materials with lower impedance ratios such as Ta_2O_5. However, for the sake of brevity, the simulations will not be included here. Suffice it to say, an 8-layer mirror of Ta_2O_5/SiO_2 performs much better than a 6-layer mirror which, in turn, performs much better than a 4-layer mirror. However, the combination of W/SiO_2 is so effective for acoustic reflectance that even with just 4 layers, an acoustic reflector of W/SiO_2 has a wider bandwith of reflectance than an 8-layer mirror of Ta_2O_5/SiO_2. This result is illustrated in Figure 4.13.

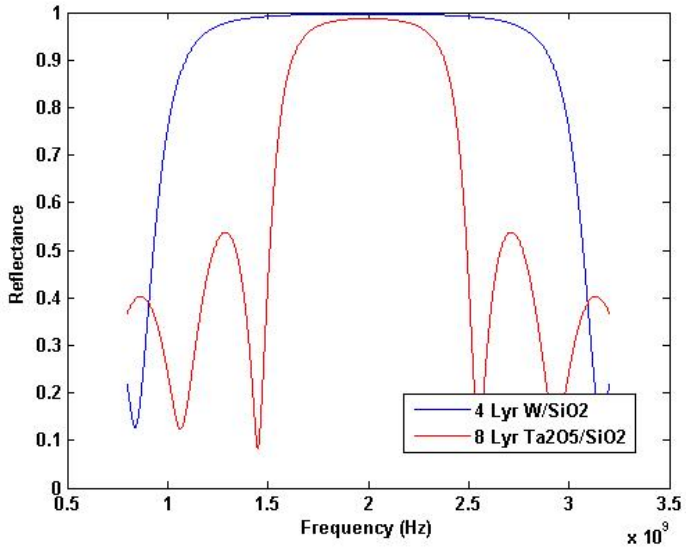

Figure 4.13 Comparison of 8-layer acoustic reflectors with W/SiO_2 and Ta_2O_5/SiO_2

The results of the calculations and simulations are useful for determining the optimal choice of acoustic reflector materials. For a thickness shear mode acoustic wave, it is concluded that the combination of tungsten and silicon dioxide performs extremely well. Further, this combination can be easily deposited with RF/DC sputtering which is an important feature for selection in the acoustic reflector design process. The choice of the number of acoustic reflector layers is not of great importance with W/SiO_2 because of the high performance of reflectors made from very few layers. However, because of the ease and simplicity of depositing a multi-layer stack, 6- and 8-layer mirrors are implemented throughout the research detailed in the subsequent chapters.

4.5 Device Fabrication Procedures & Results

Results obtained from the finite element modeling and acoustic mirror simulations helped to provide confidence that functional TSM devices could be produced

through the lateral field excitation of ZnO. The next step was to design and fabricate working devices.

The generalized single device design is illustrated in Figure 4.14. The devices consist of an acoustic reflector of alternating W and SiO_2 layers on top of a Si wafer. The ZnO is then deposited on top of the acoustic reflector and electrodes are patterned on the surface of the ZnO. Tungsten and SiO_2 are deposited by DC/RF magnetron sputtering using a Unifilm PVD-300 sputtering system. SEM analysis of the deposition layers demonstrated that we could achieve greater than 90% uniformity of deposition thickness across a 3-inch wafer. All sputtering parameters used for the fabrication of these devices are provided in Table 4.1.

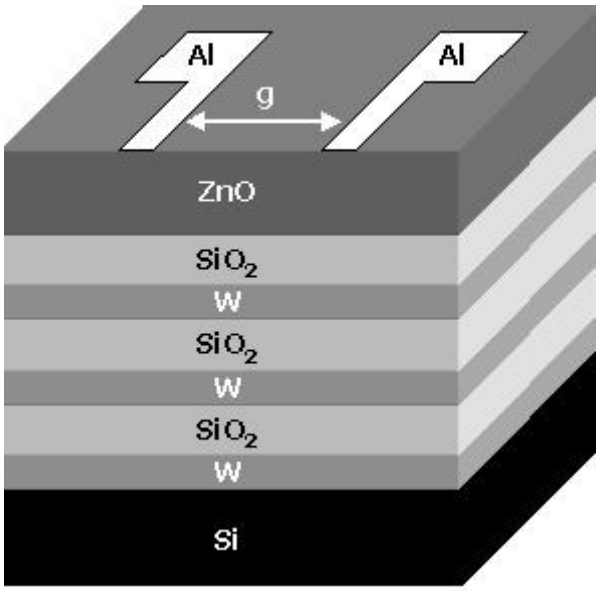

Figure 4.14 General electrode and acoustic reflector configuration

Table 4.1. Sputtering parameters for a Unifilm PVD-300 Sputterer

	W	**SiO_2**	**ZnO**
Power (Watts)	0.86 DC	281 RF	142 RF
O_2	NA	2.5%	3%
Ar	100%	97.5%	97%
Temperature (ºC)	Not heated	Not heated	325
Deposition Time (min)	84	139	115
Pressure (torr)	5.00×10^{-3}	5.02×10^{-3}	5.10×10^{-3}

The process for developing the experimentally functional acoustic mirror began with running the calculations outlined in the previous section to obtain a starting point for the layer thicknesses. The layer thicknesses were then tweaked and new devices were fabricated and tested. This cycle was repeated many times until a suitable combination was obtained. After many iterations, W and SiO_2 thicknesses of 640 nm and 1000 nm, respectively, were found to function well for the desired resonance frequency of approximately 2 GHz. The results of a Matlab simulation based on actual thickness values (measured with the SEM) for each of the layers of the fabricated device are shown in Figure 4.15. The plot illustrates that over the frequency range 1.8-2.3 GHz, the reflection coefficient approaches unity.

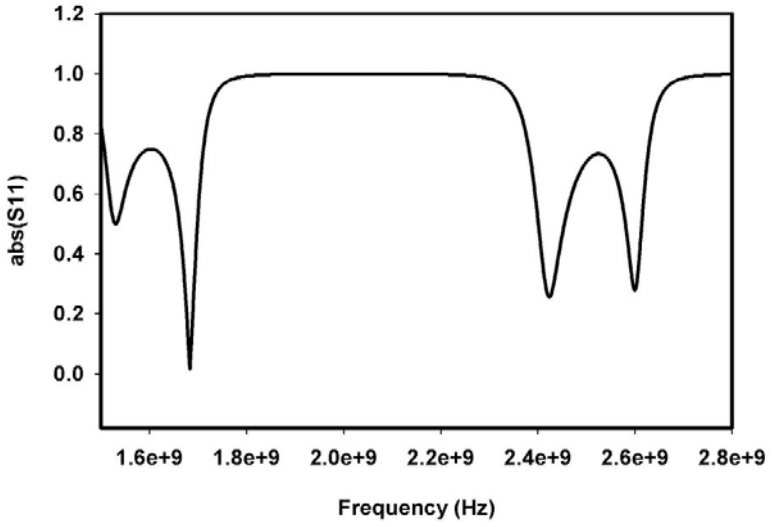

Figure 4.15 Simulated reflection coefficient frequency response calculated using actual acoustic reflector layer thicknesses in a W/SiO_2 stack.

Following deposition of the stack, a ZnO thin film is then sputter deposited on top. The thickness of the ZnO layer determines the operating frequency of the resonating device. The ZnO deposition thickness is controlled using the Unifilm PVD-300 sputtering system. Since the theoretical basis for the generation of a thickness shear mode in ZnO assumes a *c*-axis oriented crystal lattice, it was very important to verify that the orientation of the crystalline ZnO deposited with our system matches this orientation. The crystalline orientation was measured using x-ray diffraction (XRD). The XRD data were taken on a Philips X'Pert Materials Research Diffractometer™ using a hybrid mirror/monochromator incident optics and a ¼-degree receiving slit in the diffracted optics beam path. A 2θ-Ω rocking-curve scan of the film indicated a strong peak at approximately 34.26°, indicating a (0 0 2) ZnO hexagonal crystal orientation shown in Figure 4.16. The peak has a full width half maximum of 0.35°, indicating a highly oriented *c*-axis crystal film. Figure 4.16 also shows a tight peak at 40.1° which corresponds to the (1 1 0) orientation of the tungsten layers in the acoustic stack. As

expected, no peaks were observed for the SiO_2 layers in the stack because they are amorphous.

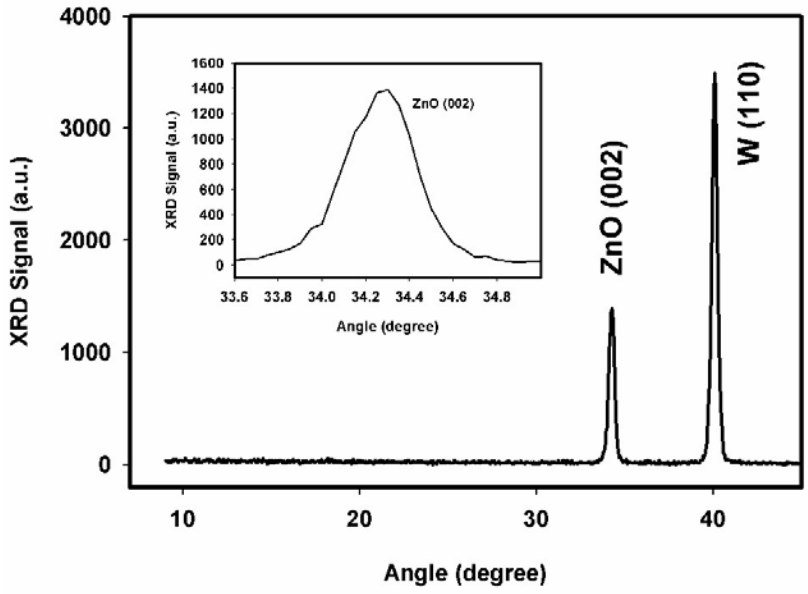

Figure 4.16 2θ-ω rocking-curve scan of the ZnO film sputtered on the 6-layer W/SiO_2 acoustic mirror. The inset is a zoomed image of the ZnO peak.

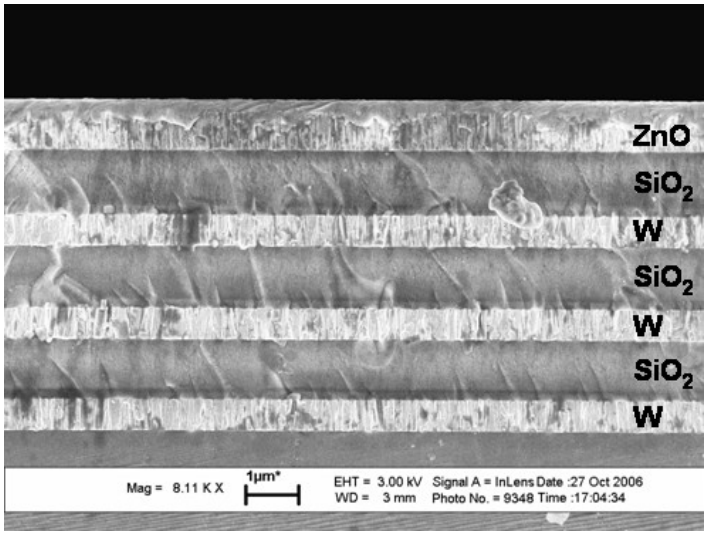

Figure 4.17 SEM image of the acoustic mirror and ZnO thin films on a Si substrate

During the development process, the thicknesses of the thin film layers deposited were periodically measured and verified by imaging a cross section of the fabricated wafer using a LEO 1530 Thermally-Assisted Field Emission (TFE) Scanning Electron Microscope (SEM). An SEM image showing a 6-layer acoustic mirror of W/SiO_2 with ZnO and can be seen in Figure 4.17.

Following deposition of the ZnO, approximately 120 nm of Al is deposited on top of a 30 nm seeding layer of Cr to create the electrodes using a CVC E-beam evaporator and a standard photolithography lift-off process to complete the device fabrication. A variety of electrode configurations were designed and tested to determine the configuration that resulted in the highest performance while still maintaining a simple fabrication procedure with high yield.

4.5.1 Device Characterization

A common way to characterize acoustic resonators is through analysis of the impedance characteristics across a frequency range. This information can be used to evaluate many parameters of a resonator such as the resonant frequency, Q factor, electromechanical coupling, and the capacitive/inductive nature of the resonator. A common method for evaluating the impedance response of a system is by measuring the scattering parameters, or the manner in which input power is reflected or transmitted. The scattering parameter measurements (S_{11}) of the fabricated resonators were obtained using a Cascade Microtech 9000 probe station with Cascade Microtech ACP probes and analyzed using a HP 8753C Network Analyzer equipped with an 85047A S Parameter Test Set. RF probing of individual devices yielded thickness shear mode activity in the

ZnO devices over a range of ZnO thin film thicknesses. Testing the acoustic response by fabricating wafers with multiple thicknesses of ZnO is important for verifying that the resonance characterized by a "notch" in the S_{11} response is due to an acoustic phenomenon rather than some electromagnetic resonance. This can be done by verifying that as the film thickness changes, the resonant frequency changes accordingly. A typical impedance response from resonators with plane-parallel electrodes separated by a gap ranging in size from 3 μm to 50 μm is shown in Figure 4.18. As can be seen from the Smith chart in Figure 4.18(b), a clear loop pattern, indicative of resonant activity, is present.

An average unloaded Q of these resonators is approximately 200 and the K^2 is approximately 0.75%, with peak values of 550 and 0.88%, respectively. The calculations used to assess Q and K^2 are: [17, 84]

$$Q = \left(\frac{f}{2}\right)\frac{d\angle Z}{df} \tag{4.19}$$

$$K^2 = \left(\frac{\pi}{2}\right)^2 \frac{f_p - f_s}{f_p}. \tag{4.20}$$

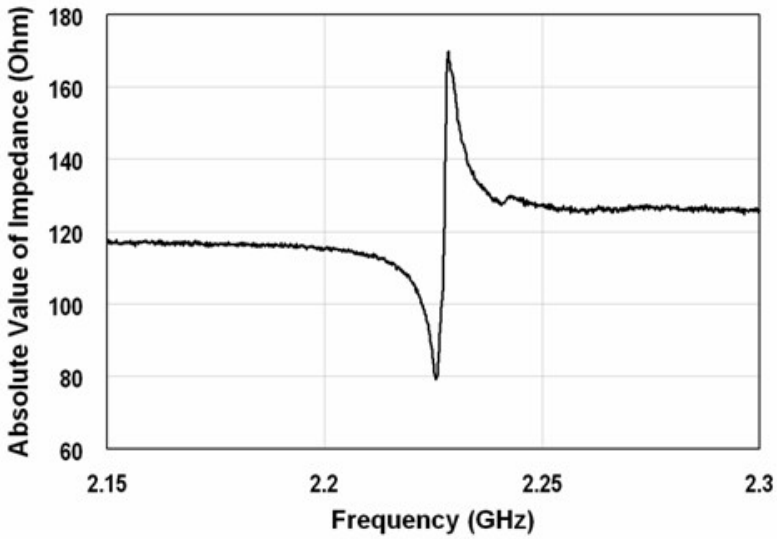

(a)

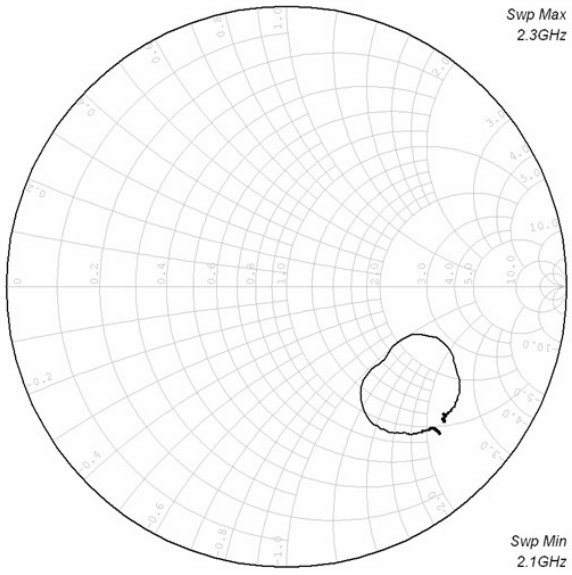

(b)

Figure 4.18 Network analyzer probe measurements of the resonators showing (a) magnitude of the impedance response as a function of frequency (b) S11 Smith chart plot

The acoustic velocity was empirically determined to be on average 3,130 m/s. This is somewhat close to the theoretical value of 2,841 m/s, but much closer to the experimental value of 3,280 m/s as calculated from the results of Woo Wai, *et al*.[85] The theoretical longitudinal velocity for ZnO is approximately 6,300 m/s. This value is much higher than the experimentally obtained acoustic velocity, and is therefore a good indicator that it is

the shear mode that is being excited, and not the longitudinal. To further confirm acoustic wave resonance, we altered the thickness of the ZnO to demonstrate that increasing the film thickness resulted in a corresponding decrease in resonant frequency. The results of these tests are summarized in Table 4.2. It is believed that the resonance may be further improved through optimization of the electrode configuration to enhance piezoelectric coupling of the electric field energy to the crystal and provide energy trapping for the acoustic wave.

Table 4.2 Effect of changing ZnO thickness on resonator response.

Measured ZnO Thickness (nm)	f_0 (GHz)	Exctracted Acoustic Velocity (m/s)
790	2.0	3,160
710	2.2	3,130
660	2.35	3,100

Aside from comparing the experimentally obtained acoustic velocity to the TSM and longitudinal velocities, another way to further establish the existence of a thickness shear mode is to expose the resonators to water at the surface. If the acoustic activity were longitudinal, application of de-ionized water at the surface would decimate the acoustic resonance observed in the device since water can support a longitudinal wave, but not a shear wave. Figure 4.19 shows the response before (squares) and after (triangles) application of deionized water to the surface. As can be seen, the water had only small effects on the suppression seen in the S_{11} magnitude response and a negative frequency shift occurred after water was applied to the device of approximately 1.1 MHz. According to the Sauerbrey equation, it is reasonable to assume that the observed frequency shift indicates a mass loading on the surface of the device by the entrapped liquid layer of the deionized water. This would also confirm the prediction made by

analysis of the Christoffel matrix that the wave is a thickness shear mode (TSM) wave. The response to the water test was shown to be repeatable across different devices in various locations about the wafer.

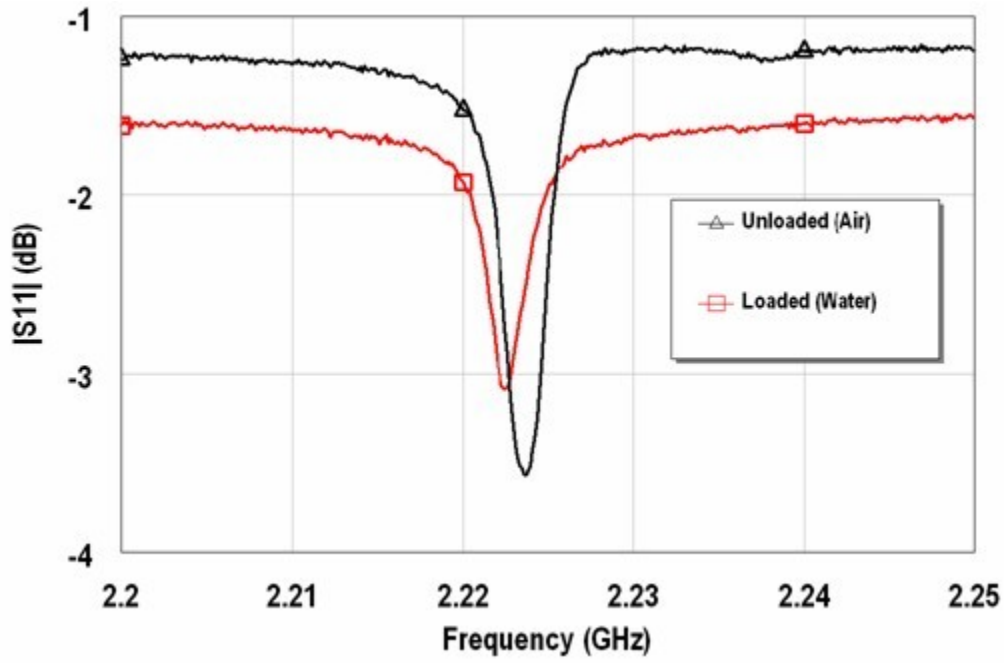

Figure 4.19 Frequency shift observed in S_{11} measurement in response to loading the surface of the resonator with deionized H_2O. Some deterioration of the resonance was observed resulting in a lower Q factor.

In order to assess the effect of the electrode configuration on device performance, a total of eight different electrode configurations were tested using two different electrode shapes – a circular pattern and a straight pattern with three electrodes situated in a ground-signal-ground formation. Pictures of these two electrode configurations are shown in figure 4.20. Among these electrode shapes, the electrode width and the gap between electrodes were varied in an effort to determine the optimal electrode configuration. Average Q and K^2 values were calculated for each of the electrode

configurations from at least 25 devices. The results are shown in Table 4.3 and summarized in [86].

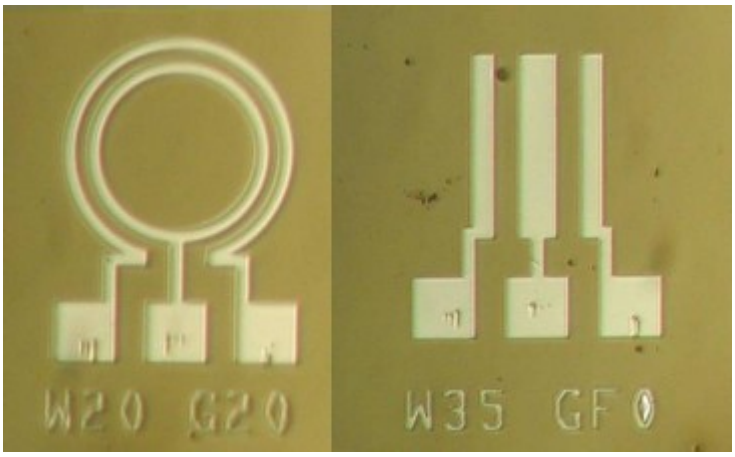

Figure 4.20 Two different electrode shapes: circular (left) and straight (right).

Table 4.3. Effects of electrode geometry on device performance

Device	Shape	Electrode Width (μm)	Electrode Gap (μm)	# Tested	Average Q	Average K^2
A	Circular	20	10	92	198	0.86%
B	Circular	20	20	72	195	0.87%
C	Circular	20	40	70	192	0.86%
D	Straight	20	10	69	198	0.84%
E	Straight	35	20	74	217	0.78%
F	Straight	35	40	98	206	0.77%
G	Straight	20	50	25	220	0.74%
H	Straight	35	50	44	221	0.73%

.

Results obtained from ANOVA analysis of these results demonstrate that a statistically significant gap ($p < 0.01$) emerges between the performance of the circular shaped devices and the straight electrode devices when analyzing their K^2 and Q results. It is evident that the average Q is higher for the straight electrode configuration while the effective K^2 is lower. One possible explanation for this is that the circular electrode configuration has a larger surface area over which excitation of the crystal occurs.

Therefore, the coupling of the electric field to the crystal over grain boundaries and crystal non-uniformities is more efficient overall while the added mass of the larger electrodes acts to reduce the Q.

It was hypothesized that the electrode width would play a role in determining device performance because of the relationship between electrode width and volume of ZnO excitation. We postulated that a wider electrode would excite a larger volume of ZnO which would translate into greater coupling of the electrical energy into mechanical strain. This result was not substantiated by the data, however, as the size of the gap between electrodes had no clear functional relationship with the device performance. This result can potentially be explained by the fact that the electrical field vector is laterally oriented primarily in the gap between the electrodes, while it is primarily oriented normal to the surface in the volume below the electrodes. This means that widening the electrode would have no affect on the excitation of a shear mode but should play a role in the excitation of a longitudinal mode. Gap size did prove have some impact, however, as can be seen from device D in Table 4.3. Compared with the other straight electrode configurations, the 10 μm gap exhibits a significantly lower Q and higher K^2, on average. It appears that beyond a particular threshold between 10 μm and 20 μm between straight electrodes, there was a notable improvement in Q. No clear pattern emerges beyond this, however. Rosenbaum asserts that effective implementation of a LFE resonator requires that the gap width between electrodes must be many times greater than the thickness of the film [17]. It could be that this requirement is met somewhere between 12 and 24 times the thin-film thickness.

Having determined that the straight electrode configuration yielded higher Q devices, which has been identified as the desired parameter, 8-element arrays of these devices were fabricated in order to verify that the resonator designs performed as well in the array configuration as individual devices. The goal was to confirm that the array structure did not bear any beneficial nor detrimental effects on the resonator's performance. Sampling 88 arrayed devices similar to those seen in Figure 4.21 showed that there in fact was a statistically significant difference in device performance. A 30% decrease in Q and a 15% decrease in K^2 was observed for devices with a 20 μm gap fabricated in the array configuration versus the isolated configuration. For devices fabricated with a 50 μm gap, again a decrease of 30% was observed in Q but only a 5% decrease in K^2. One explanation for the decrease in performance is the addition of a significant amount of conductor material surrounding the active devices for bonding pads and ground-bus connections. The added mass from the electrodes provide a lossy material at the surface boundary which can act to scatter the acoustic energy.

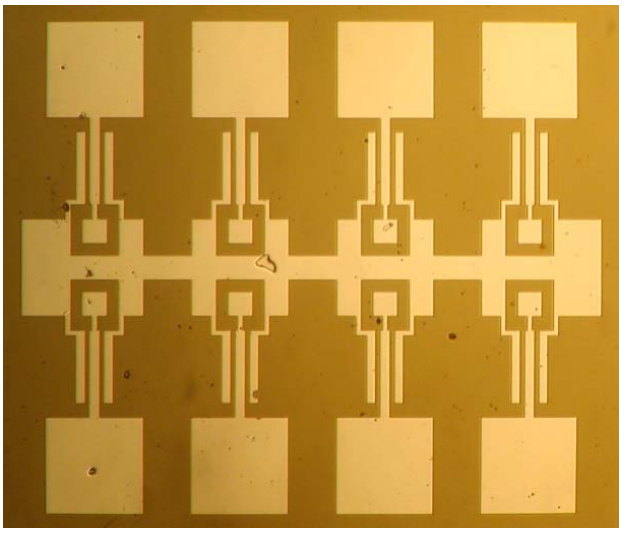

Figure 4.21 8-Device Array configuration

Despite the slight reduction in device performance due to the array configuration, the resulting device performance was found to be sufficient for use in sensor testing. The advantages gained with the array configuration outweigh the losses associated with the device performance. One of the most important advantages of the array configuration is that it allows for multiple sensor testing and for redundancy in measurements.

4.6 Off-Axis Excitation

Crystalline *c*-axis oriented Zinc Oxide is widely used in acoustic filters operating in the longitudinal mode. The TE electrode configuration used to excite the longitudinal mode typically consists of plane-parallel electrodes fabricated on either side of the ZnO thin-film. This permits the direction of the electric field generated by the electrodes to be normal to the surface. For *c*-axis oriented ZnO, this field orientation excites the longitudinal bulk mode. However, in an electrode configuration consisting of a bottom electrode that is larger than the top, a portion of the electric field is oriented in such a way that coupling to the shear mode will also exist due to a lateral electric field component [14]. When an acoustic reflector configuration is implemented, the acoustic mirror can be tuned to reflect the shear mode while suppressing the longitudinal mode. The result is a resonant device that exhibits a significant thickness shear mode resonance produced by a thickness excitation electrode configuration. Another method that has been explored in the literature for exciting the TSM resonance with a thickness excitation electrode configuration involves deposition of *c*-axis inclined ZnO [77, 78]. Excellent results have been obtained; however, the standard RF-sputtering process must be modified in one of a

variety of ways in order for an inclined film to be grown. These methods complicate the sputtering process and may introduce unwanted variation in the deposition uniformity.

As previously discussed, the thickness shear mode response is ideal for liquid sensing applications because the particle displacement is not supported by liquid which results in minimal damping of the thickness shear mode. The reduction in resonant frequency by a fluid film can be attributed to a coupled interfacial fluid layer. To describe the operation in liquid, Kanazawa and Gordon [54] derived an equation that relates the frequency shift Δf to the effective mass loading of the fluid layer. The effective mass is related to the shear wave penetration depth, which is a function of viscosity of the liquid, η_l, operating frequency, f_o, and density of the liquid ρ_l. The Kanazawa-Gordon relation is then:

$$\Delta f = -f_o^{3/2}\sqrt{\frac{\eta_l \rho_l}{\pi \mu_Q \rho_Q}} \tag{4.21}$$

where μ_Q is the stiffness of the quartz crystal, and ρ_Q is the density of the quartz. It is evident from Equation 4.21 that a TSM-sensor based on viscosity-density changes of the contacting liquid can be developed [55]. That is not to say that mass, density, and viscosity of the contacting film are the only determinants of the resonant frequency of the device. Surface roughness, fluidic pressure, surface hydrophobicity, and film viscoelasticity are just a few of the other parameters that can effect a change in the resonance condition.

While virtually all liquid-phase studies with TSM resonators have been performed on QCM devices, the analyses that have been performed can be related to TSM resonators comprised of a piezoelectric material other than quartz. The physics described by the equations presented in the literature are not unique to a quartz TSM device. For

this reason, we have explored the application of TSM ZnO thin-film resonators as highly sensitive liquid sensors. In this section, we present a study that exhibits a thin-film TSM resonator responsive to changes in the density-viscosity product as predicted by the Kanazawa-Gordon equation.

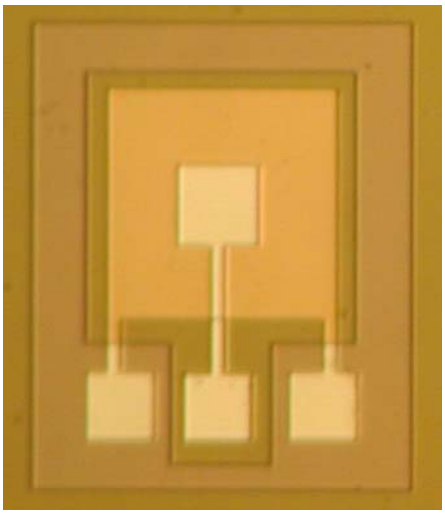

Figure 4.22 Top view of the fabricated acoustic resonator

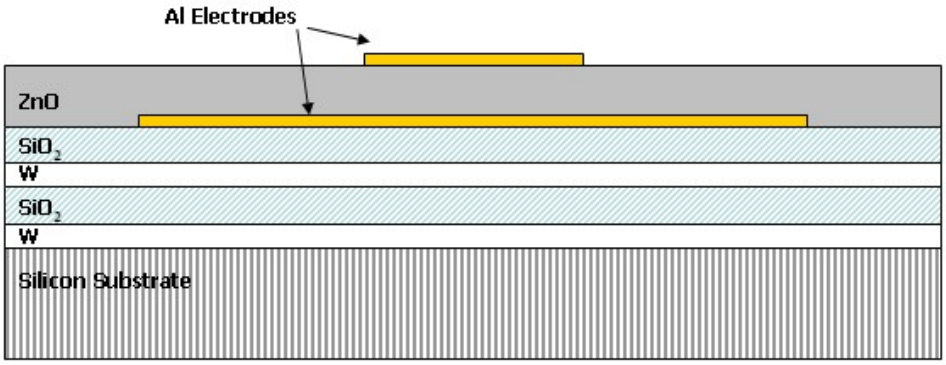

Figure 4.23 Schematic cross-section of the acoustic resonator

4.6.1 Experimental Methods

The fabrication process for the TSM resonators is essentially the same as that of a standard solidly mounted ZnO FBAR. The resonator is comprised of a four-layer acoustic mirror deposited onto a Si wafer. A 150 nm bottom aluminum electrode was DC-

sputtered on top of the acoustic mirror. The ZnO thin-film is then RF-sputtered onto the stack followed by a smaller, top electrode. A photograph and a cross-sectional schematic of the fabricated device is shown in Figure 4.22. The mirror layers consist of alternating pairs of W and SiO_2 deposited using DC and RF sputter-deposition. The desired thicknesses of the mirror layers were deposited in line with those discussed in the previous section. There are many combinations of layer thicknesses that will provide a reflection coefficient close to unity over a single desired frequency range. However, by judiciously selecting the thicknesses of the acoustic mirror layers, it is possible to find a configuration in which the longitudinal mode is nearly suppressed while the thickness-shear mode is reflected. This is made possible by the fact that the acoustic velocity for the longitudinal mode is slightly more than twice that of the shear mode which results in a good separation between the resonant frequencies for a given ZnO thickness.

The theory behind a TSM resonator operating with the electrode geometry shown in Figure 4.22 requires that some portion of the electric field be laterally oriented. If the electric field was solely oriented through the thickness of the ZnO, a resonant TSM mode could not be electrically excited because there is no coupling to a shear mode from this field orientation as predicted by the piezoelectric coupling tensor. In order to verify that a portion of the field was laterally oriented, finite element modeling simulations using Comsol Multiphysics finite element software were performed. Using a static electromagnetic model, the orientation of the electric field in the region of ZnO at the periphery of the top electrode was calculated.

Tests were performed to verify that the resonance observed in the frequency response was the result of a thickness shear mode acoustic response and not due to

electromagnetic resonance or some other acoustic mode. First, the experimentally achieved acoustic velocity was calculated and compared to the acoustic velocities reported for the ZnO thickness shear mode in the previous section ~ 3,170 m/s. Additionally, water was dropped onto the surface of the device, covering it completely. The test was performed to rule out the existence of a longitudinal mode since liquid loading will greatly diminish the resonance of a longitudinal mode. Once the thickness shear mode was verified, it was necessary to test the sensitivity of the device to a change in the density-viscosity product. Glycerol solutions of 0, 5, and 10% by volume in water were prepared and pipetted onto the resonator surface such that that it was entirely covered in the solution. The frequency response was obtained every 3 seconds from an HP8753 network analyzer. A Labview software program recorded the data from the network analyzer and plotted the resonant frequency in real-time as the trials took place.

4.6.2 Results

The results of the finite element modeling are shown in Figure 4.23. The figure shows a streamline plot which helps to visualize the direction of the electric field lines but gives no real indication about the strength of the field. Figure 4.23 indicates that the electric field is oriented at an angle of approximately 60-40 degrees from the *c*-axis through most of the ZnO just at the periphery of the top electrode. This phenomenon occurs within about 1 wavelength from the edge of the top electrode while the electric field is oriented normal to the surface in-between the electrodes and further than 1 wavelength from the edge of the top electrode. These results explain why a shear mode can be excited with this electrode orientation. An electric field oriented at such an angle has both a thickness component and a lateral component. It is the lateral component that

is coupled to the thickness shear mode. Because of the existence of a thickness component of the field which couples to a longitudinal mode, it is important for the design of a solely thickness shear resonator to use an acoustic mirror that suppresses the longitudinal mode.

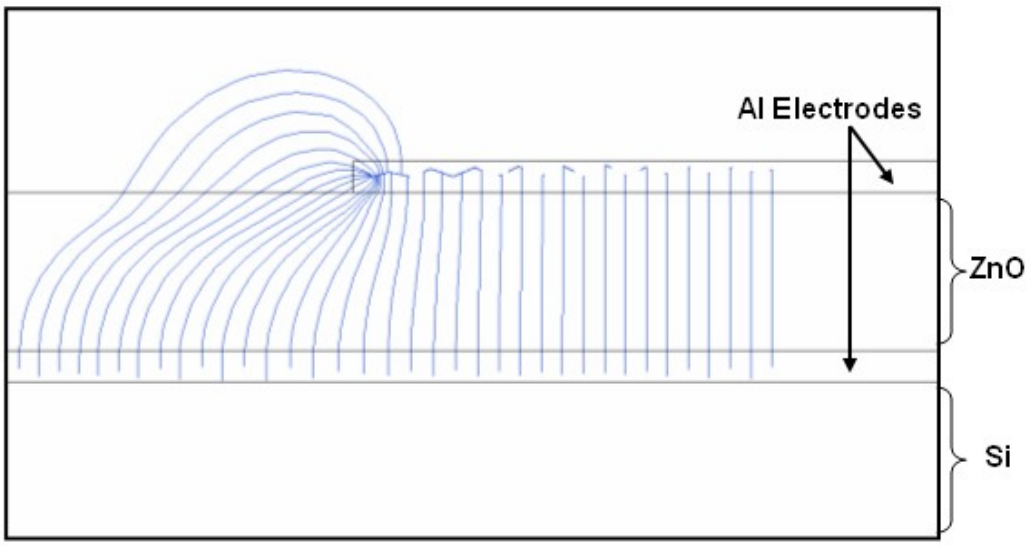

Figure 4.24 FEM plot of electric field streamlines showing the slanted "off-axis" electric field

Evaluation of device performance was carried out using an HP8753 with an S-parameter test set. A Matlab script was written to calculate the theoretical piezoelectric coupling factor (K^2) for the shear and longitudinal modes as a function of angle between the electric field and the *c*-axis similar to the plot derived by Krishnaswamy et. al [76]. The results shown in Figure 4.24 illustrate that at 60 degrees, the coupling is ~5.2% for the shear mode and 2.5% for the longitudinal. Devices were fabricated with a ZnO thickness of roughly 780 nm and an operating frequency of 1.988 GHz. On average, the devices exhibited a Q of approximately 80 for the thickness shear mode. The acoustic velocity was calculated to be approximately 3,086 m/s, which is in-line with previously reported values [14]. However, because the acoustic mirror is tuned to accentuate the

shear resonance and not the longitudinal resonance, the longitudinal mode observed at 6,287 m/s exhibits an average Q of only 18.

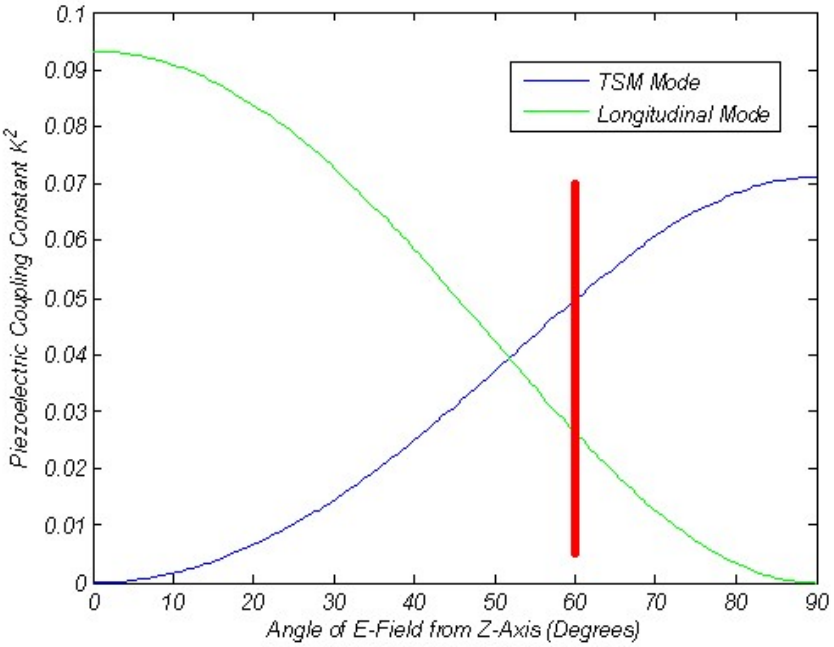

Figure 4.25 Plot of electromechanical coupling Vs. e-field angle for excitation of the TSM mode and the longitudinal mode in ZnO

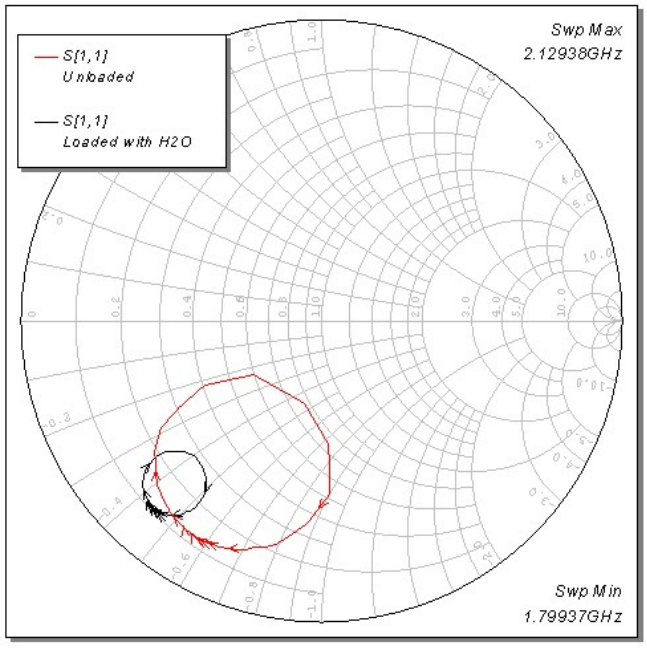

Figure 4.26 Smith chart showing resonance before and after H_2O loading

Figure 4.25 illustrates the effect of dropping 3 µl of water onto the device to cover it completely. The Smith chart shows a reduction in the overall radius of the acoustic loop as well as a slight increase in inductance. The water-loaded average Q for the shear mode is reduced from 80 to 20. If the acoustic activity were longitudinal, the application of water to the surface would decimate the signal because liquid supports a longitudinal mode and therefore the modal energy is dissipated into the adjacent liquid medium. The water does have some effect the on suppression of the signal, but this is to be expected with any TSM mode, including that of the QCM. We have observed a reduction in Q by about 75% after loading the surface of the QCM with water.

Glycerol/H_2O solutions of 0%, 5%, and 10% by volume were prepared and dropped onto the resonators to test the sensitivity to increasing density-viscosity of solution [71]. The tests were performed in real-time and the resonant frequency transient response was recorded. Figure 4.26 illustrates a typical normalized transient response to the application of a 5% glycerol/H_2O solution. The initial sensor response at t = 0 sec shows the initial stabilization period of the sensor. At t = 180 sec, the glycerol solution was applied to the sensor surface. The normalized data was obtained by subtracting the sensor frequency when the experiment began from the frequency at each time point. The final frequency shift was calculated as the average of the noisy signal response after the liquid loading occurred.

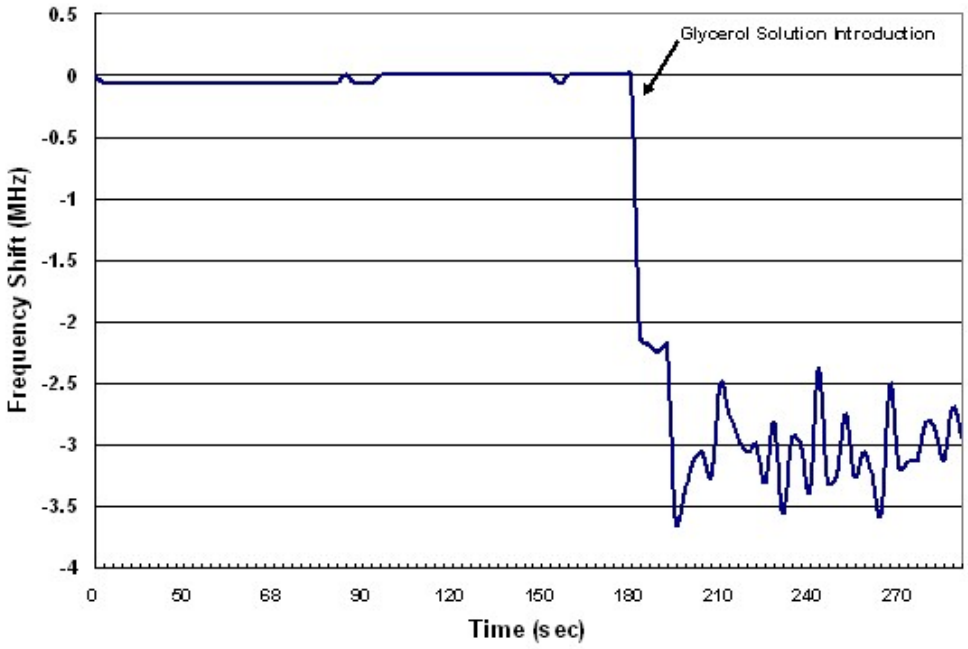

Figure 4.27 Transient response of a sensor with introduction of glycerol solution at t = 180 sec.

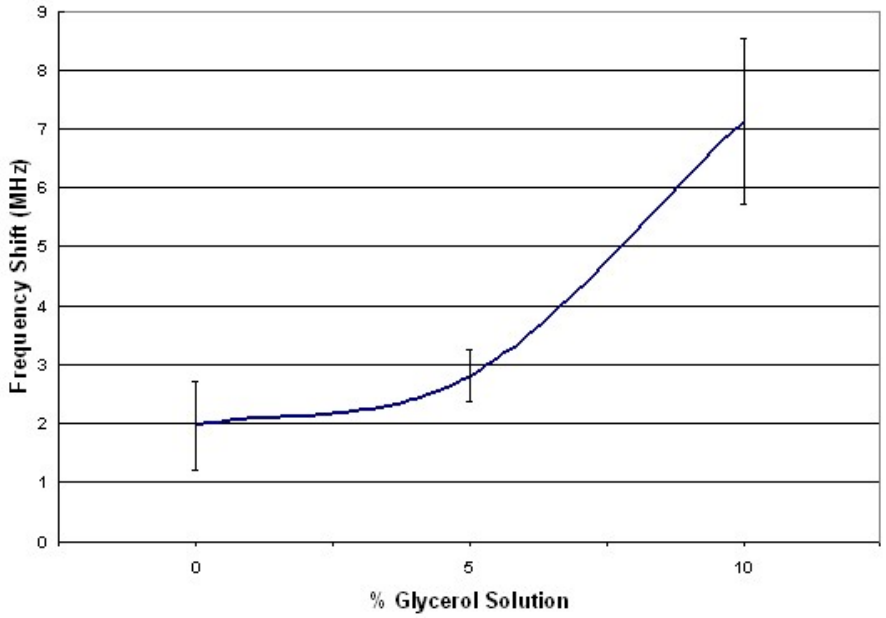

Figure 4.28 Average frequency shifts of the sensors as a function of glycerol concentration in water (Error Bars = S.D.)

The final frequency shift from multiple trials at each concentration was calculated and the averages are shown in Figure 4.27. The plot shows that the magnitude of

frequency shift increased as the density-viscosity product of the solution was increased. The sensors were tested for their sensitivity to the density-viscosity product through frequency monitoring in response to varying concentration solutions of glycerol in water. The results indicate that the sensors are significantly sensitive to the density-viscosity product. Further research must be completed in optimizing the electrode geometry to accentuate the TSM and to improve sensitivity and frequency stability.

4.7 Chapter 4 Conclusions

Theoretical analysis of the Christoffel equation has shown that a TSM wave can be excited in c-axis oriented ZnO with an in-plane excitation field oriented in any direction on the wafer. Further, it has been shown that the shear particle displacement will be parallel to the excitation field, assuming an entirely lateral field.

A solidly mounted resonator consisting of alternating layers of W and SiO_2 was grown on Si substrates with ZnO as the active piezoelectric layer at the surface. The acoustic mirror was designed to have a reflection coefficient closest to unity near the frequency of operation. The acoustic mirror frequency response was simulated to provide assurance of the frequency range coverage given a fixed number of alternating pairs of W and SiO_2. Finite element modeling was also performed to predict the electric field of an electrode configuration consisting of two long electrodes positioned on the top of the ZnO with a gap between them. Simulations showed that the electric field within the gap between the electrodes was primarily laterally oriented while the electric field directly beneath the electrodes was shown to be reduced in magnitude with an orientation normal to the surface of the ZnO.

To verify the thickness shear mode operation of the devices, we investigated the experimentally extracted acoustic velocity and the effects of water loading on the resonance. Without these tests it is difficult to adequately determine that a resonance is necessarily TSM. We have presented evidence of a TSM wave through exposure of the device to deionized water, comparison of extracted acoustic velocity with theoretical acoustic velocity, and varying the piezoelectric film thickness to yield respective changes in the frequency response.

On the basis of these results, it is expected that with an appropriate chemical surface preparation, these devices could be used as a platform for biosensor applications. The simple fabrication and small device size make this an appropriate candidate for fabrication of sensor arrays. The results of our investigation indicate that the lateral excitation of a thickness shear mode in solidly mounted ZnO FBARs is realizable both theoretically and experimentally.

CHAPTER 5

ANTIBODY IMMOBILIZATION ON ZnO

5.1 Introduction

The previous chapters have outlined the development of a ZnO-based acoustic resonator operating in the TSM mode. However, a TSM acoustic resonator by itself is not capable of functioning as a biosensor. It can be transformed into a biosensor by adding a molecularly specific capture layer to bind target molecules of interest. Typically this consists of monoclonal antibodies but may also involve other proteins, enzymes, or aptamers. This chapter describes the development of surface chemistry protocols capable of functionalizing planar ZnO surfaces with antibodies – an area of research that had previously not been explored in the literature.

Acoustic biosensors such as QCMs and other thickness excitation resonators have electrode configurations which lie in the path of the acoustic wave. This can be both an advantage and a disadvantage for sensors, especially when the electrodes are made of gold. The lossy gold electrodes will absorb some of the acoustic energy, leading to a lower quality factor. However, gold has also been the subject of much surface immobilization chemistry research, and well defined methods of linking antibodies to Au surfaces have been developed [87, 88]. One issue that arises with a LFE ZnO sensor is that there are no electrodes located in the active area of the device. Therefore, immobilization techniques other than those employing alkane thiols must be developed to immobilize antibodies directly on the ZnO substrate in the absence of a gold surface.

A requirement for high precision biosensors is that the output signal, or response, be repeatable given multiple identical samples and on different sensor elements prepared in the same manner. Therefore controlled, reproducible immobilization of appropriate capture molecules to form a molecularly-specific coating on the ZnO is necessary to preclude device to device signal variations.

Attachment of antibodies to the surface of oxides can be achieved through simple adsorption. However, for biosensor applications, formation of a covalent bond between the antibody and the oxide surface via a chemical crosslinker is the preferred method over adsorption for several reasons. First, the stable bonds that are formed yield a more robust sensor due to the relative strength of covalent bonds. The resulting immobilization of target molecules allows for potentially harsher experimental conditions and expanded use. Further, biosensor experiments often require that the sensor be subjected to fluidic flow. The covalent immobilization of antibodies may prevent detachment of the antibodies from the surface under fluid flow, which would erroneously affect the sensor's output signal.

To date, the literature pertaining to functionalizing oxides through covalent methods has largely been focused on SiO_2. Hydroxyl groups at the surface of an oxide provide sites for reaction with cross-linking molecules to form covalent bonds [89]. One of the more common methods for functionalizing SiO_2 surfaces involves the use of organosilanes. Organosilanes react at room temperature with surface hydroxides to link the silane molecules to the oxide surface. Success with immobilizing antibodies on silica surfaces has been shown using amine- and thiol-terminal silanes such as 3-Mercaptopropyltrimethoxysilane (MTS) with a variety of heterobifunctional crosslinkers

including N-γ-maleimidobutyryloxy succinimide ester (GMBS) [89, 90]. Heterobifunctional crosslinkers serve the purpose of transforming the end group of the silane into a group that will bind covalently with functional groups on an antibody. Bhatia *et al.* reported that antibody immobilization with a number of different organosilanes yielded a comparable amount of antibodies immobilized from one silane to the next and that the resulting covalently bound biofilm maintained similar overall antigen binding capacity. They also found that there was minimal loss of antibody function after immobilizing the antibodies to the silica surface [89, 90].

Other work in modifying SiO_2 surfaces has focused on forming self-assembled monolayers using expoxysilanes [91, 92]. One advantage of using an expoysilane such as (3-glycidoxypropyl)trimethoxysilane (GPS) for forming self-assembled monolayers (SAMs) on oxide surfaces is that it eliminates the need for a heterobifunctional crosslinker between the silane molecule and target antibodies since the exposed epoxy groups react readily with amine groups on lysine residues of the antibody. The usefulness of this antibody immobilization technique has been illustrated on indium-tin oxide (ITO) substrates for the development of *Escherichia coli* O157:H7 sensors [93, 94]. However, one of the issues that has been reported with modifying surface oxides using organosilanes is that the quality of surface modification may be sensitive to the amount of water present during the modification reaction [95]. In anhydrous conditions, a partial monolayer of organosilane molecules forms resulting in incomplete coverage of the substrate. In excess H_2O, self-condensation can occur between the silane molecules and a multilayer can form, often accompanied by gelling of the silane.

An alternative to organosilanes for surface modification of oxides is the use of phosphonic acids. Phosphonic acids theoretically do not suffer from the same susceptibility to hydration levels that organosilanes do and do not easily self-condense. They have been used for the functionalization of ITO electrodes for development of electrochemical sensors [96] and for modifying TiO_2, $BaTiO_3$, and ZnO particles [97-99]. In another study, phosphonic acids were used to pattern ITO and Indium Zinc Oxide (IZnO) through microcontact printing and subsequent wet etching [100].

Despite the amount of research that has been performed on various oxides, including SiO_2, there have been relatively few studies involving surface functionalization of ZnO. One such study reports the use of an amine-terminated silane, 3-aminopropyltriethoxysilane (APS) and glutaraldehyde as a crosslinker to bind a protein, Interleukin-6, to the ZnO surface [101]. One drawback to the use of glutaraldehyde, however, is that it is known to form large polymers which may bind many residues and form multiprotein complexes. Studies by Thomsen and Watts *et al.* highlight issues to consider regarding the adsorption of amine-terminated silanes to oxidized Zn sheet surfaces (as opposed to deposited crystalline ZnO) [102, 103]. It is shown that the degree to which each moiety of the SAM (the silane or the amine) binds to the ZnO surface is largely dependent upon the pH of the solution. A molecular dynamics study confirms that silane molecules with polar head groups, such as amines, prefer a more stable conformation parallel to the surface rather than aligned perpendicular to the surface [104]. These studies tend to indicate that amine-terminated silanes may not be the optimal surface treatments when further conjugation steps such as linking antibodies to the surface are required.

Apart from surface treatment with silanes, there have been very few other reports of surface modification studies performed on ZnO. In a study by Sadik *et al.*, adsorption of alkane-thiols to Zn- and O-terminated ZnO surfaces to form SAMs was investigated, but the study did not involve further functionalization with antibodies or any other type of protein [105]. Other studies have described methods for functionalizing ZnO nanostructures, however they are of limited use for translation to planar ZnO surface chemistry because of the morphological and crystalline differences between RF sputtered ZnO surfaces and single crystal nano-structures. In a study by Liu *et al.*, ZnO nanorods were functionalized using dimercaptosuccinic acid followed by EDC to bind amine groups located on the antibody [106]. Another study outlined the use of a pH 5 solution of 11-triethoxysilylundecanal to coat ZnO nanoparticles leaving an amine-reactive aldehyde group for subsequent conjugation with antibodies [107].

The focus of this chapter is to investigate antibody immobilization protocols on device-quality sputtered ZnO surfaces with three different primary crosslinking molecules. The results will provide a foundation for further research in developing highly uniform antibody immobilization protocols for planar ZnO surfaces. MTS, GPS and 10-Mercaptodecanylphosphonic Acid (MPA) were deposited onto the ZnO surface using a conventional wet method. Subsequent secondary crosslinking with GMBS was performed for ZnO surfaces coated with MTS and MPA. To provide visual confirmation of the density and uniformity of antibody immobilization, fluorescently labeled antibodies were incubated with the surface. The results were investigated using water contact angle measurements, atomic force microscopy, and confocal microscopy. A protocol involving APS was also explored, but was found to form large glutaraldehyde conglomerates on the

surface, as previously reported, which is undesirable for sensor applications. As a result, experimentation with this protocol was ceased.

5.2 Surface Immobilization Methodology

ZnO samples were prepared by depositing 500 nm of ZnO onto 3" (100) silicon wafers (University Wafer) by RF magnetron sputtering using the Unifilm PVD-300 sputtering system. The wafers were diced into 1 cm × 1 cm squares for surface functionalization experiments. Prior to surface functionalization, the ZnO samples were sonicated in acetone for 5 minutes in an ultrasonic bath before being cleaned using an ion beam mill. The samples were etched in a 20% oxygen / 80% argon atmosphere for 5.5 minutes. This was done to remove any adsorbed chemical species from the surface and to provide a reactive surface for the primary crosslinker to bind.

The three primary crosslinker solutions for treating the ZnO samples were prepared under a nitrogen atmosphere: a 4% solution by volume of MTS (Fluka) in dry toluene (Sigma); a 4% solution of GPS (Sigma) in dry toluene; and a 1 mM solution of MPA in 95% ethanol (Sigma). MPA was synthesized by Peter Hotchkiss, a graduate student under Dr. Seth Marder at Georgia Tech, in accordance with the procedures from the literature [108].

Immediately following the ion etching procedure to clean the ZnO surface, samples were placed in vials containing 2 mL of either the silane or phosphonic acid solution, sealed, and placed in a nitrogen environment for 24 hours. The samples were then removed from the vials and rinsed with ethanol followed by sonication for 5 minutes in ethanol. The samples were then dried with a stream of N_2. Samples treated with either

the 4% MTS or the 1 mM MPA were then placed in vials containing 2 mL of 2 mM GMBS (Fluka) in ethanol and sealed for 24 hours. The GPS-treated samples do not require treatment with a secondary crosslinker because the terminal epoxy groups react directly with the antibody. Following sonication in ethanol, GPS coated samples were immediately treated with the antibody solution as described below. The MTS+GMBS and MPA+GMBS treated samples were removed from the solution and sonicated in ethanol for 5 minutes. The activated ZnO surfaces were then used for covalent attachment of antibodies.

The activated surfaces were treated with 548 nm Alexa-Fluor labeled Goat anti-rabbit IgG antibodies (Invitrogen). 25 µl of a 200 µg/mL solution of the fluorescently labeled antibodies in PBS buffer (pH 7.4) was pipetted onto the surface of the samples. The antibody solution was incubated for 2 hours in an opaque container in a nitrogen environment at room temperature, after which the substrate was rinsed with aliquots of PBS buffer followed by ultra-pure water to remove any unbound antibodies from the surface. Control samples for testing simple antibody adsorption were prepared by incubating ion etched ZnO samples with the antibody solution for 2 hours

5.3 Characterization Methodology

5.3.1 Water Contact Angle Measurements

Water contact angle measurements were performed using an SEO Phoenix 150 Contact Angle Analyzer. The contact angles for each of the 3 surface treatments were evaluated by averaging the contact angles from at least five separate measurements for

each surface treatment following reaction with the primary crosslinker. Silane and phosphonic acid-treated samples were measured and compared to a control sample consisting of ZnO with no surface treatments other than ion etching to clean the surface of any adsorbed species and sonication in ethanol to simulate the rinse process. The measurements were used as a semi-quantitative method of determining the film quality and reproducibility as well as to confirm that the surface was being chemically modified.

5.3.2 AFM Measurements

Samples were measured using a Digital Instruments (DI) 3000 AFM in tapping mode after treatment with the primary crosslinker, secondary crosslinker (in the case of MTS and MPA treated samples) and after incubation with the antibody solution. AFM probe tips were obtained from Veeco Instruments (FESP). Multiple scans of each sample were taken to ensure uniformity in the measurements across each 1 cm × 1 cm sample. The scans were evaluated for surface roughness and overall average particle height and diameter using the DI Nanoscope software. Both 5 μm × 5 μm and 1 μm × 1 μm scans were taken at each location on all samples and used for the calculation of the surface morphology metrics.

5.3.3 Confocal Microscopy

Following the antibody conjugation reaction, the devices were dried with a stream of N_2 and fixed to a glass slide in preparation for confocal microscopy analysis. A Zeiss Laser Scanning Microscope (LSM) 510 equipped with a HeNe laser (543 nm excitation) was used to visualize the distribution and intensity of the fluorescently labeled antibodies. Each sample was viewed at 10× and 40× magnification and images were taken at random

locations throughout the area of antibody deposition. Control samples were prepared and analyzed for comparison between fluorescence due to antibody coverage and fluorescence to due background noise. Rather than incubation with the 200 μg/mL antibody in PBS, the control samples were treated with the full crosslinking protocol then incubated with 25 uL of 5 mM azide in PBS to replicate the solution containing the Alexa-Fluor labeled antibodies. Therefore, the only difference between the treatment protocols for the control and target samples is the presence of antibodies. To quantify the fluorescence for each surface treatment, the detector gain was fixed at a constant value and images were taken for all of the samples. The RGB luminance intensity signal was measured for each pixel in 0.03 mm^2 areas across the samples. The average fluorescence intensity was calculated by taking the mean pixel luminance intensity for ~ 9300 pixels within a 0.03 mm^2 area over at least 25 separate measurements.

5.4 Results & Discussion

Based on previously described mechanisms [89, 94, 101], a summary of the reactions for covalently attaching antibodies to the ZnO surface is shown in Figure 5.1. Deposition of the silanes and phosphonic acid are achieved through reaction of the head groups with hydroxyl groups at the ZnO surface to link the molecules to the ZnO leaving functional tail groups available for further conjugation reactions. The GPS surface treatment (Fig. 5.1 (a)) makes use of epoxy ring tail groups which are capable of reacting with amine groups on the antibody. For surface treatments involving the MTS and MPA reactions (Fig 5.1 (b)), the thiol group on the MTS and MPA molecules react with the maleimide region of the secondary crosslinker GMBS in organic solvent. This reaction

leaves the succinimide residue of the GMBS available for antibody attachment. The succinimide residue then binds to an available amino group of the antibody to form a covalent bond between the antibody and the ZnO surface. It is important to note, however, that targeting amine-groups on the antibodies does not promote any specific orientation of the antibodies since amine-containing residues such as lysine can be located on many parts of the antibody. Despite this, it has been shown that antibodies immobilized using this approach still maintain a significant amount of activity, albeit less than with oriented immobilization techniques such as those that target the carbohydrate group on the F_c region of the IgG antibody.[90] Additionally, the ease and simplicity of the immobilization protocols studied here make them more suitable for biosensor applications than oriented immobilization techniques which often require numerous steps, harsh experimental conditions, and high antibody losses prior to immobilization.

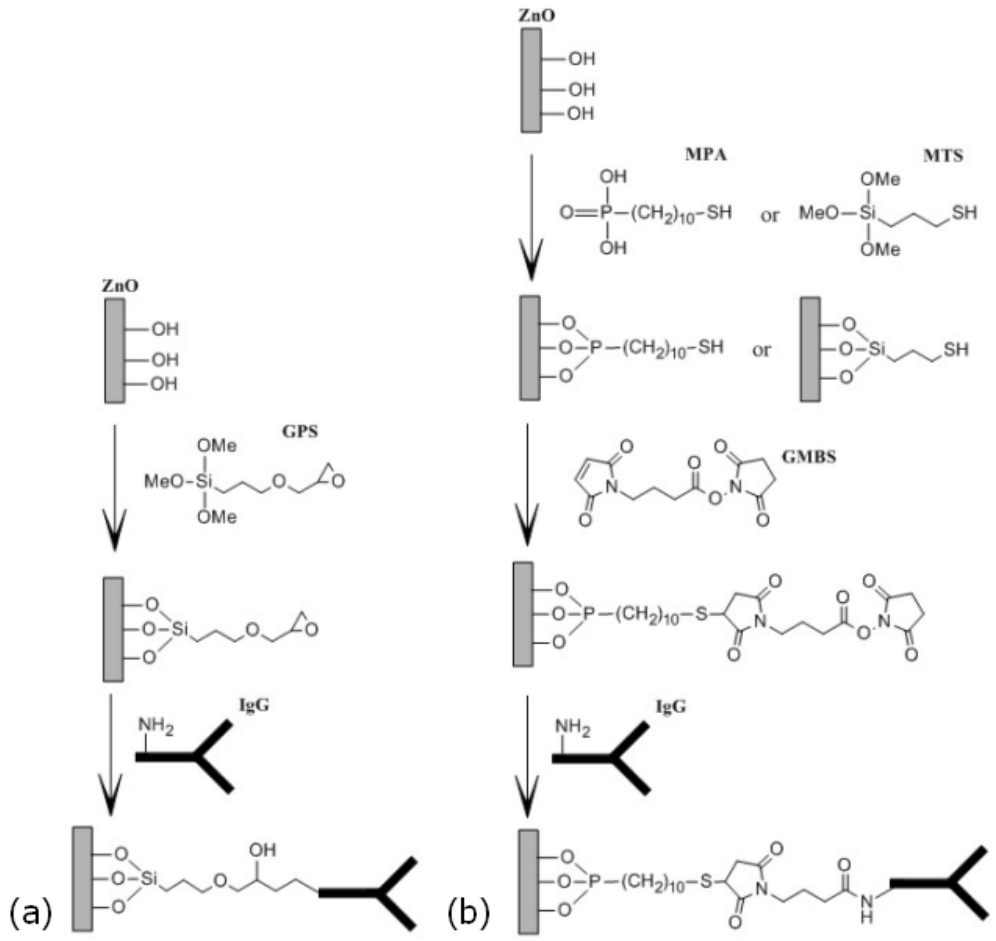

Figure 5.1 The immobilization procedure for covalent attachment of IgG antibodies to the ZnO surface by three primary crosslinkers. The hydroxylized ZnO surface is treated with (a) (3-glycidoxypropyl)trimethoxysilane (GPS), (b) 10-Mercaptodecanylphosphonic acid (MPA) or (3-Mercaptopropyl)trimethoxysilane (MTS) followed by the secondary crosslinker N-γ-maleimidobutyryloxy succinimid ester (GMBS).

The results from the water contact angle (WCA) measurements after the samples were coated with the primary crosslinkers MTS, GPS, and MPA for 24 hours are provided in Table 5.1. The data shows that the average WCA for each of the crosslinkers deposited were greater than the WCA of the control, indicating an increase in surface hydrophobicity. Samples coated with MTS had an average water contact angle of 77° ± 1 which were statistically different than the untreated ZnO (control) case which exhibited a water contact angle of 72° ± 1 ($p = 0.002$). The contact angle results for surfaces coated

with MTS seem to agree well with previous WCA investigations of dithiol self-assembled monolayers on gold which were reported to be approximately 83° on average [109].

Table 5.1. Water Contact Angle Measurements for Surface Treatments

Surface Treatment	Avg. WC Angle (degrees)
Untreated ZnO	72 ± 2
GPS	80 ± 5
MTS	77 ± 1
MPA	83 ± 5

The WCA measurements performed with the 4% GPS solutions also suggest that the surface is being chemically modified. The samples coated with GPS yielded a significant increase in average WCA of 80º ± 5. An interesting phenomenon was observed for samples coated with GPS, however. Immediately after the water droplet is placed onto the sample surface, it was observed that the WCA is much higher than the control case indicating that the surface is hydrophobic. However, the WCA changes as a function of time in a manner that seems to be unrelated to evaporation phenomena. The WCA value of 80º was averaged from measurements taken immediately after the drop was placed on the surface. Over the time period of 20 to 30 seconds the water contact angle is reduced anywhere by about 5-10 degrees and then stabilizes. This phenomenon was only observed on samples treated with the GPS solution and was not observed for surface treatments with MTS or MPA. Water droplets on ZnO surfaces treated with MTS or MPA formed stable water droplets with WCA that changed very little, if at all, over a 30 second time period. This potentially points to an unstable surface with the GPS film

that is disrupted by H_2O. One possible explanation for this phenomenon is that the water droplets react with the exposed epoxy groups, hydrolyzing the ring to form surface hydroxyl groups which would result in a more hydrophilic surface. Due to the relative smoothness of the GPS surface as indicated by AFM measurements, it is unlikely that this phenomenon is due to surface roughness.

Similar to the samples treated with GPS, the samples treated with MPA exhibit a WCA on average to be approximately 83° ± 3. This indicates that the surface has become more hydrophobic and implies that the surface is being modified with the chemical treatment. The same conclusion can be drawn for the GPS and MTS surface treatments as well.

AFM was used for monitoring the morphological changes at the surface that result from coating the surface with the crosslinkers and subsequent immobilization of antibodies. Table 5.2 shows the mean surface roughness, mean particle height and mean particle diameter for the surfaces after treatment with each of each of the immobilization protocols. For the untreated ZnO control case, the mean surface roughness was found to be approximately 2.8 (± 0.4) nm while the particle heights and diameters are 3.0 (± 0.5) nm and 24.7 (± 7.8) nm, respectively.

Table 5.2. AFM Surface Analysis for 24 hr Wet Method Surface Treatments

Surface Treatment	Roughness (nm)	Avg. Particle Height (nm)	Avg. Particle Diameter (nm)
Untreated ZnO	2.8 ± 0.4	3.0 ± 0.5	24.7 ± 7.8
GPS	1.2 ± 0.3	2.3 ± 0.6	20.5 ± 11.3
GPS + Ab	2.0 ± 0.1	3.3 ± 0.8	24.1 ± 10.4
MTS	2.4 ± 0.1	3.4 ± 0.4	22.9 ± 5.8
MTS + GMBS	3.7 ± 0.8	6.8 ± 0.7	26.9 ± 8.4
MTS + GMBS + Ab	7.0 ± 1.5	13.7 ± 0.3	33.2 ± 6.9
MPA	3.1 ± 0.2	3.8 ± 0.5	31.5 ± 13.5
MPA + GMBS	2.9 ± 0.3	3.9 ± 0.3	25.4 ± 7.7
MPA + GMBS + Ab	6.3 ± 2.0	9.2 ± 1.8	31.4 ± 12.8

The control scan of the untreated ZnO sample shown in Figure 5.2(a) shows the characteristic cobblestone appearance with round grains that have fairly well defined boundaries. The characteristic AFM scan shown in Figure 5.2(b) of the surface after silanization with GPS shows a surface that is morphologically different from that of the controlled case. The surface roughness decreases on average by 42% to 1.2 (± 0.3) nm. This implies an overall smoothening of the surface which is similarly suggested by the appearance of the scan. One likely explanation is that the GPS molecules have been deposited into the gaps in-between the grains to fill some of the grain boundaries. The results were observed at many locations across any single chip, and from chip to chip. After incubation with the antibody solution, the GPS+Ab treated surface has an increased surface roughness on average to 2.0 (± 0.1) nm with an average particle height of 3.3 (± 0.8) nm which indicates that the surface is being modified after treatment with the antibody solution. A typical scan of the Ab-treated surface is shown in Figure 5.2(c).

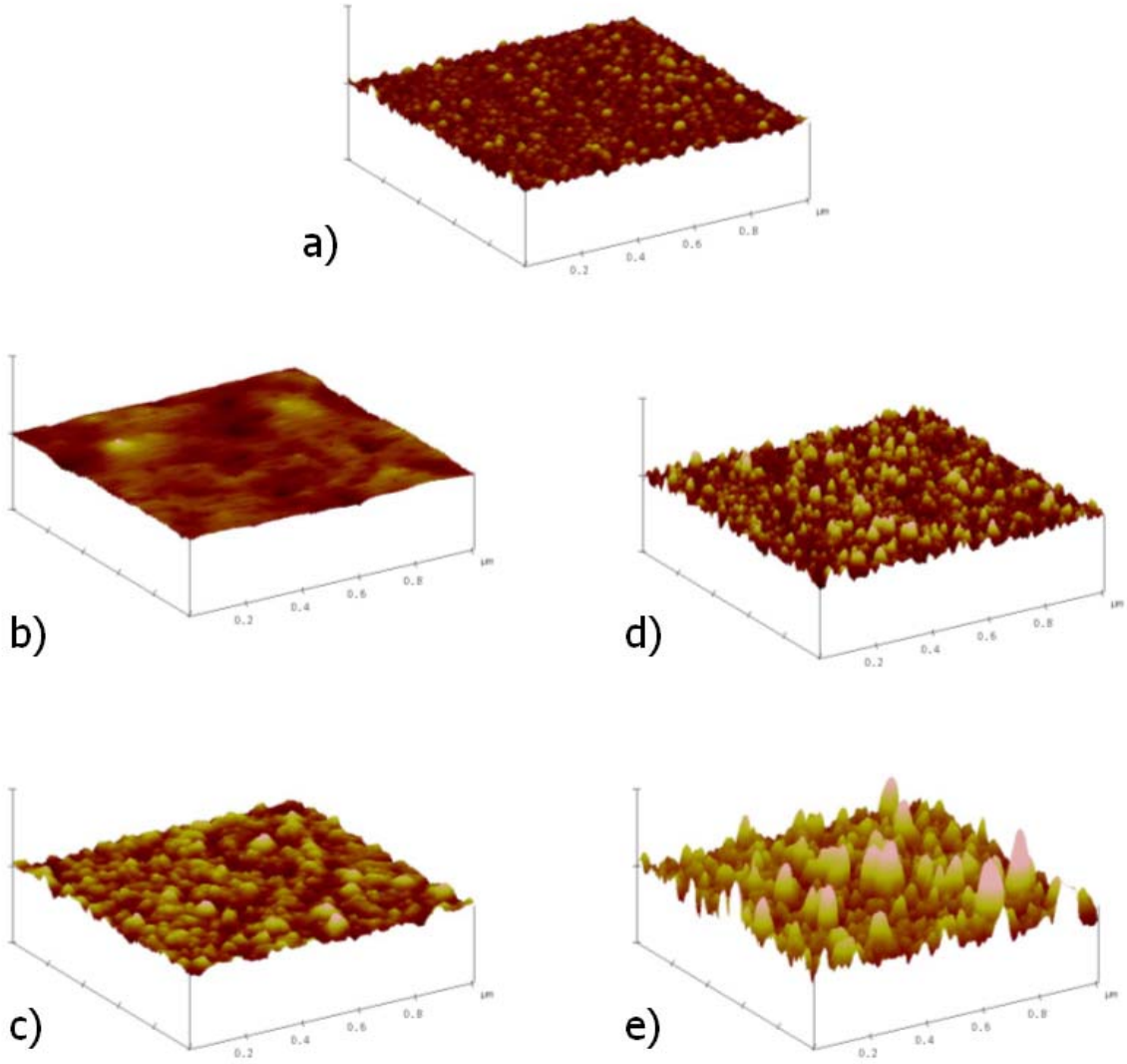

Figure 5.2 Atomic Force Microscope topographical scans of (a) the untreated ZnO surface and samples treated with (b) GPS, (c) GPS+Ab, (d) MTS+GMBS, and (e) MTS+GMBS+Ab. The scan sizes are 1 μm × 1 μm with a vertical scale of 65.0 nm.

The AFM scans of the samples treated with MTS+GMBS in Figure 5.2(d) show significant differences in the surface morphology as compared to the GPS and the untreated control. Rather than a decrease in surface roughness, we see an increase in surface roughness to 3.7 (± 0.7) after treatment with MTS+GMBS. The average particle height for the MTS+GMBS treated samples was increased to 6.8 (± 0.4) nm indicating an increase in particle size due to deposition of the MTS+GMBS. Figure 5.2(e) clearly

shows that subsequent treatment with the antibody solution yields particles on the surface that have a significantly larger average height 13.7 (± 0.3) nm which is indicative of the immobilization of the antibodies to the surface. The data from these scans along with the WCA measurements provide confidence that the surface is being chemically modified with the silanes and that the surfaces are morphologically modified after treatment with the antibody solution.

Representative AFM scans of the samples treated with MPA+GMBS and MPA+GMBS+Ab are shown in Figures 5.3(b) and 5.3(c), respectively. The surface shown in Figure 5.3(b) exhibits increased particle height, on average from the control case. These notions are supported by the increased average particle height of 3.9 (± 0.3) nm which is a 30% increase. Statistically, the morphology metrics are not much different when comparing the surface treated with MPA only and the surface treated with MPA+GMBS. This is unexpected, given the evidence of increasing roughness and overall particle size for the MTS+GMBS samples over the MTS-only treated samples. One explanation is that the GMBS treatment is forming a more uniform coating on the surface of MPA rather than forming clumps as may be the result in the MTS+GMBS scans. After treatment with the antibody solution, the ZnO surface seems to undergo a morphological change with much larger particles observed on the surface. The average roughness and particle height are increased significantly which is in accordance with what was observed with the MTS treatment.

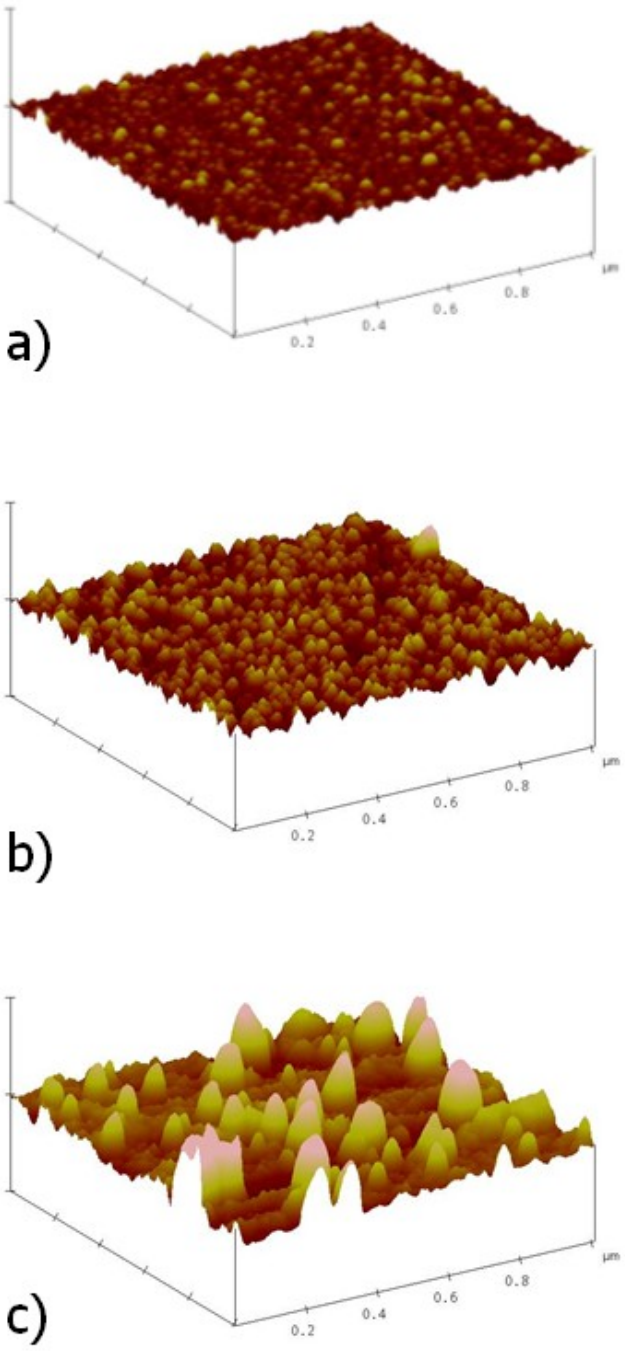

Figure 5.3 Atomic Force Microscope topographical scans of (a) the untreated ZnO surface and samples treated with (b) MPA+GMBS and (c) MPA+GMBS+Ab. The scan sizes are 1 µm × 1 µm with a vertical scale of 65.0 nm.

While the AFM scans tend to indicate that the surfaces are being modified with the surface treatment, fluorescence microscopy was employed to confirm these results and provide more information about antibody surface coverage density and uniformity.

Prior studies characterizing antibody immobilization techniques have generated a variety of methods for analyzing the amount of antibodies bound to the surface of a material [89, 90, 94]. As acoustic biosensors become increasingly more compact, the antibody immobilization surface coverage becomes increasingly more important. It is necessary to compare the surface treatments quantitatively, which is demonstrated in this study through an analysis of the fluorescence. Figure 5.4 shows a comparison of the average fluorescence intensity (luminescence) for the three immobilization methods vs. the untreated bare ZnO sample. Included are the average fluorescent intensities for the control samples which serve as an estimation of the combined background fluorescence from the ZnO, the crosslinkers (for the GPS, MTS, and MPA treated chips), and the PBS buffer.

The fluorescence of the bare ZnO sample treated with antibodies above the level of fluorescence exhibited by the control can be attributed to a small amount of antibody adsorption to the surface of the ZnO in the absence of crosslinking molecules. The average intensity was found to be highest for the MTS as compared to the MPA, GPS, and ZnO. Statistically, the fluorescence of the samples treated with the MTS were on average about 26% higher than the samples treated with MPA and about 40% higher than the samples treated with GPS ($p < 0.001$). Since level of the fluorescence within a region of constant size is related to the amount of fluorophor present, these results indicate increased antibody surface coverage with the MTS over the other surface treatments. The MTS fluorescence as compared to the untreated ZnO case indicates roughly a three-fold increase of average fluorescent intensity ($p < 0.001$). The uniformity of the antibody coverage can be correlated to the standard deviation in pixel luminance for each of the

samples. We found a lower standard deviation for surfaces treated with MTS as compared to both MPA and GPS which indicates an overall higher uniformity over 25 separate measurements across multiple samples which include ~9500 pixels each. The increased fluorescence observed in samples treated with MTS over those treated with GPS was repeatable from sample to sample which also indicates robustness in the protocol with each of these surface treatments.

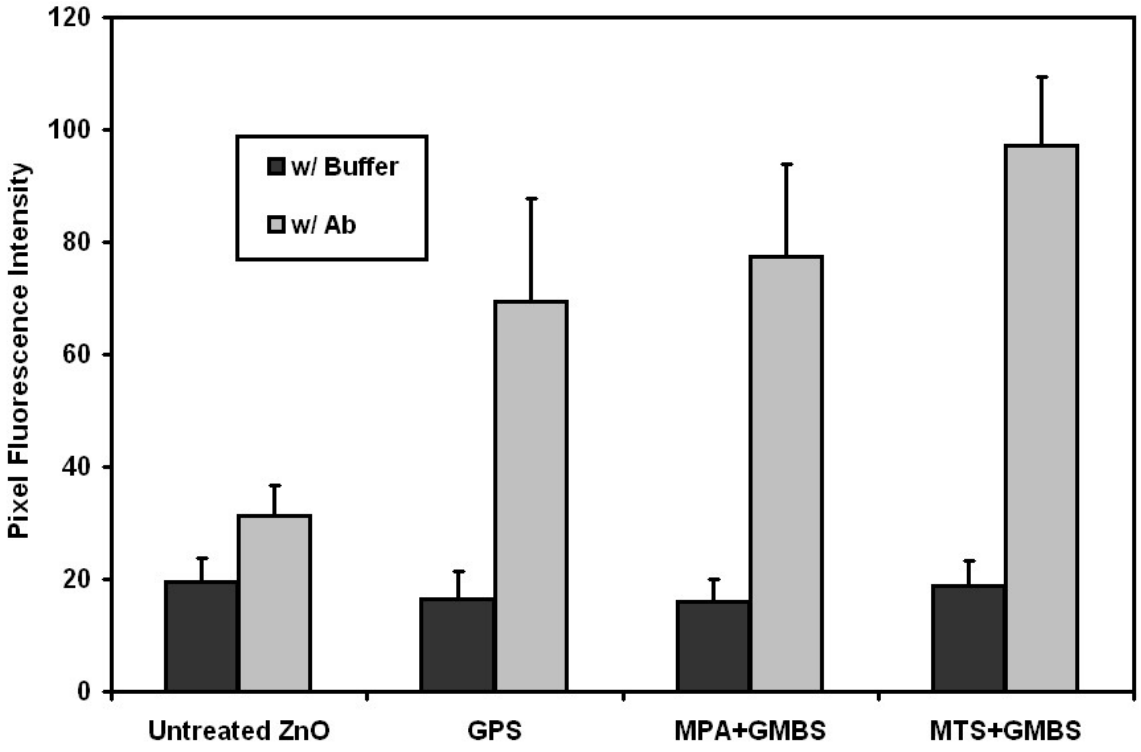

Figure 5.4 The average fluorescence intensity for each surface treatment after incubation with antibodies vs. incubation with buffer (Error bars = standard deviation).

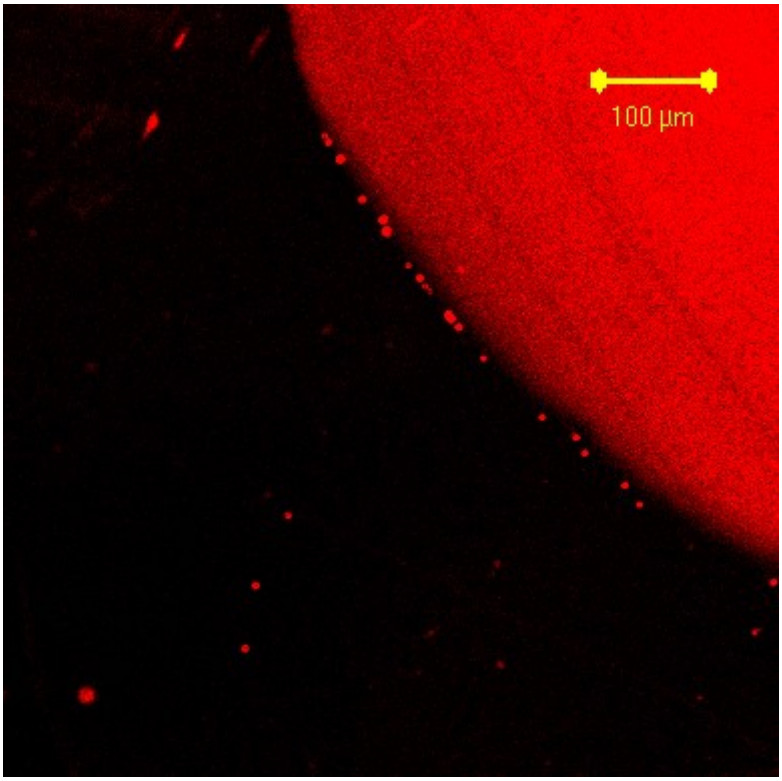

Figure 5.5 Fluorescence microscopy image showing the edge of the region of antibody deposition on a sample treated with MTS+GMBS. The bright region illustrates the fluorescence due to antibodies.

Figure 5.5 shows a fluorescence image taken at the edge of the spot where antibodies were deposited on a sample treated with MTS+GMBS after washing in PBS and HPLC grade water. The image is provided to illustrate the contrast in pixel intensity from the untreated region versus the region treated with antibodies. The image also helps to visualize the density of antibody coverage. To put things in perspective, the electrodes of the LFE sensors are roughly 200 µm in length with a gap size of approximately 20 µm. Based on the size bar shown in Figure 5.5, the fluorescence is fairly dense in this region which illustrates high coverage on the scale that we are interested in. It is expected then, that devices treated with antibodies through this method will have a significant number of

antibodies located within the active region of resonance which lies in-between the electrodes in the gap.

5.5 Chapter 5 Conclusions

This chapter has outlined an investigation of antibody immobilization techniques using three different primary crosslinkers on planar ZnO surfaces. The surfaces were analyzed using water contact angle measurements, atomic force microscopy, and fluorescence microscopy to determine the surface characteristics and overall antibody surface coverage. Relatively high antibody coverage on the ZnO surface was achieved through the use of both silanes and a thiol-terminated phosphonic acid with GMBS. It was discovered that the MTS surface treatment provided the highest density of antibody immobilization and the greatest uniformity. Theoretically, the primary advantage of using phosphonic acids over silanes lies in the stability of the chemical surface coating to hydration levels. This is important for biosensor applications, where an ideal antibody immobilization technique would be unaffected by varying hydration levels in biological samples under test. However, we found that the protocol employing MTS was not highly susceptible to variations in hydration after the coating had been applied. It has been demonstrated in the past with alkane-thiol SAMs that as the chain length decreases, the monolayer becomes increasingly disordered with lower packing density and coverage [110]. Since the MPA chain length is longer than those of MTS and GPS, the surface coverage obtained with MPA may in part, be elevated above GPS due to the larger chain length. Studies performed with a propyl phosphonic acid would be a more appropriate method for determining whether the increased surface coverage is due to the phosphonic

acid or the chain length. However, this was not the aim of the study described here and will be left for subsequent studies.

This study is offered as an initial study for immobilization of antibodies on planar ZnO surfaces. Functionalization of crystalline ZnO surfaces is becoming an increasingly important topic as new biosensor platforms are being developed with this material and current investigations are underway for studying the formation and properties of phosphonic acid coatings on ZnO. Further work should build upon the studies detailed here for optimizing immobilization times to maximize the density and uniformity of covalent antibody immobilization procedures. It is concluded that MTS is the best choice for moving forward in functionalizing the ZnO LFE sensors due to the fact that it provides the highest surface coverage with the best uniformity. Further, it is a commercially available chemical while the phosphonic acid is not.

CHAPTER 6

LFE SENSOR TESTING

6.1 Introduction

The previous chapters have detailed the development of a LFE TSM resonator and the surface functionalization protocols for transforming the resonator into a biosensor. This chapter focuses on describing initial testing of the sensors with biological materials in an effort to characterize the detection capabilities of the sensors. The aim here is not to provide an exhaustive study for a wide variety of molecular targets in patient samples. Rather, it is to focus on providing an initial assessment of the detection capabilities of the sensors to clinically relevant biomarkers. The results of the testing will provide insight into the advantages and disadvantages of the current configuration so that improvements can be made to further generations of the devices.

In this chapter, we look at the detection of two different biological markers using the shear mode resonators described in Chapter 4. The first marker of interest is mesothelin, a molecule that was used in proof-of-concept testing with QCMs in Chapter 3. Mesothelin is a protein that is highly expressed in several cancers including mesotheliomas, ovarian and pancreatic cancers, and some squamous cell carcinomas [6, 7, 111, 112]. The normal biological function of cell-membrane bound mesothelin is not known and knockout mice have no apparent phenotype. One of the forefronts in research pertaining to mesothelin involves targeting the cell-bound protein with immunotoxins for the treatment of cancers overexpressing mesothelin [113]. Despite being a cell surface protein, mesothelin can be shed like many other surface proteins. This enables the

measurement of mesothelin in serum. One study detailed the development of a sandwich ELISA test for measuring mesothelin levels in the serum of healthy volunteers, patients with advanced stage mesothelioma, and patients with ovarian cancer [114]. The study found that all healthy patients had mesothelin levels below 9 ng/mL with 87% having levels below 5 ng/mL. However, the median serum mesothelin level found in patients with mesothelioma was 26.2 ng/mL. Patients with stage III and stage IV ovarian cancer exhibited a median serum mesothelin level of 16.6 ng/mL. This study was the first to illustrate that mesothelin is shed into the serum in detectable levels. However, the study focused on quantifying mesothelin in the serum of patients with advanced stage cancers for monitoring efficacy of surgical tumor debulking – not on quantifying mesothelin for early detection of early stage cancers.

Another group of studies examined the levels of mesothelin in pleural effusions and serum of mesothelioma patients for diagnostic purposes [115, 116]. They found mesothelin serum levels to be elevated in patients with confirmed cases of mesothelin, however their methodology rendered them unable to quantify the concentrations. The study also showed that the detection of mesothelin in pleural effusions may aid in the differential diagnosis of mesothelioma in patients presenting with effusions. In this chapter, a dose-response curve is developed for examining the sensitivity of the sensors to purified mesothelin. By exposing the sensors to known concentrations of mesothelin in solution, we can get a good estimate of the sensitivity and detection limit for this particular molecule of interest.

The other biological marker we focus on for illustrating the detection capabilities of the sensors is PSA, or prostate specific antigen. A PSA test is commonly used for

aiding in the detection and diagnosis of prostate cancer. It is one of the only FDA approved biomarker tests for the diagnosis of any type of cancer. The current-PSA test is performed using one of a few different commercially available tests on a patient's blood sample. This is typically a sandwich assay similar to a standard ELISA test. PSA levels below 4 ng/mL are considered to be normal. PSA levels in the range of 4 ng/mL to 10 ng/mL are considered to be elevated and levels of PSA above 10 ng/mL are significantly elevated. In this chapter, we explore the capability of the sensor system to detect PSA in prostate cancer cell line conditioned media. Testing the sensors in complex media such as conditioned media is an important step in establishing the potential effectiveness of these sensors for diagnostic testing.

6.2 Sensor Testing

6.2.1 Methods

The acoustic sensor devices were fabricated using the protocol outlined in Chapter 4. An acoustic mirror of 8 alternating layers of 640 nm of W and 1000 nm of SiO_2 were deposited on a Si wafer. ZnO was sputtered to a thickness of 750 nm to produce devices that operate in the 2 GHz frequency range. Electrodes were patterned on the surface of the ZnO consistent with previously described methods.

Functionalization of the resonators was performed using the MTS silanization surface chemistry described in the previous chapter. Wafers were diced into 1 cm x 1 cm dies which were cleaned using the ion mill and subsequently immersed in a 4% MTS solution in toluene for 24 hours to sufficiently silanize the ZnO surface. The dies were then removed, rinsed, and sonicated in ethanol for five minutes. They were then immersed in a solution of 2 mM GMBS in ethanol for another 24 hours to expose the

surface to the crosslinker molecule. Following the reaction, the dies were again rinsed and sonicated in ethanol for 5 minutes to remove any excess chemicals from the surface. After being rinsed, samples were dried with N_2 and 25 µl of the antibody solution was pipetted onto the devices. The antibody solution was allowed to incubate for 2-3 hours and was subsequently washed with buffer followed by purified H_2O.

6.2.1.1 Mesothelin Testing

For the mesothelin tests, the target sensors were coated with 20 µg/mL of an MB antibody solution. The mouse monoclonal MB antibodies were developed in the laboratory of Ira Pastan at the National Cancer institute. They have been shown to detect mesothelin by immunohistochemistry, fluorescence-activated cell sorting, and ELISA and have a K_d of 1 nmol/L [117]. The reference sensors were coated with a 20 µg/mL solution of Anti-fitc monoclonal IgG antibodies (sc-69871 – Santa Cruz) because fitc is a synthetic molecule that is not present in the samples of interest.

A series of tests were performed to independently analyze the sensor response to buffer solutions spiked with varying concentrations of purified mesothelin-rfc. Mesothelin-rfc is a recombinant fusion protein also developed in the laboratory of Dr. Ira Pastan at the NCI which consists of the 40 kDa COOH-terminal mesothelin protein fused to rabbit Fc [117]. There are no known commercially available sources of purified mesothelin protein. However, this mesothelin-fc fusion protein has been used for developing ELISA calibration standard curves in the past and contains the entire extracellular portion of mesothelin.

Following functionalization of the acoustic sensors, the devices were placed in shallow dishes of pH 7.4 PBS buffer to keep the antibody coating hydrated for subsequent antigen binding. The sensors were then tested using an HP8753 network analyzer to record the impedance measurement of the devices and to establish the initial resonance frequency of each device. The sensors were then incubated with 25 μL of the mesothelin-rfc buffer solution for 25 minutes. Sensor tests were performed on samples of mesothelin-rfc in PBS buffer with concentrations of 1 ng/mL, 10 ng/mL, 100 ng/mL, 10 μg/mL, and 50 μg/mL. After the incubation period, the sensors were rinsed with buffer and water to remove any unbound protein, dried with N_2 and were then re-tested using the network analyzer to record the post-exposure impedance response. The data from each sensor experiment was analyzed and the center parallel frequency was measured from the impedance responses before and after exposure to the sample. The frequency shifts were calculated by subtracting the perturbed frequency from the unperturbed frequency. Average frequency shifts across multiple sensors for each sample concentration were calculated and plotted. In very specific cases, noisy signals were not included in the measurement. One-way ANOVA was used to evaluate the statistical significance between the frequency shifts and the concentration of sample solution.

6.2.1.1 PSA Testing

The PSA tests were performed on a complex sample with an unknown concentration of PSA. However, to give a reference for the results obtained from the PSA tests, positive control and negative control sensors were tested. The negative control sensors were coated with a 20 μg/mL Anti-FITC antibody solution (sc-69871 Santa Cruz) because FITC is a synthetic molecule and should not be found in any biological

sample. The positive control sensors were coated with anti-Alkaline phosphatase antibodies (sc-80678 – Santa Cruz). Alkaline phosphatase is an enzyme that is present in all human tissues and should be present concentrations at a detectable level in this type of sample. The target sensors were coated with anti-PSA antibodies (sc-52170 – Santa Cruz) which are capable of binding both free and conjugated PSA.

The detection experiments were performed in a similar fashion to the mesothelin experiments. After functionalization of the acoustic sensors, the devices were placed in shallow dishes of pH 7.4 PBS buffer to keep the antibody coating hydrated for subsequent antigen binding. The sensors were tested using an HP8753 network analyzer to record the impedance measurement of the devices and to establish the initial resonance frequency of each device. The sensors were incubated with 25 μL of LNCaP prostate cancer cell line conditioned medium for 25 minutes. After the incubation period, the sensors were rinsed with buffer and water to remove any non-specifically bound molecules and were then tested again using the network analyzer to record the post-exposure impedance response. In very specific cases, noisy signals in which the actual frequency shift was difficult to determine based on the peak finding method were excluded for these preliminary tests. The impedance responses of the remaining sensors were plotted and frequency shifts were calculated based on the difference in the center parallel frequency from before and after exposure to the sample.

6.3 Sensor Test Results

The sensor tests performed with increasing concentrations of purified mesothelin solutions resulted in increasing shifts, on average, for the target sensors. The sensors targeting mesothelin tested at 1 ng/mL had an average frequency shift of 12 kHz. This

was about a third of the shift observed for target sensors in response to solutions with a mesothelin concentration of 10 ng/mL which was on average 86 kHz and found to be significantly different from the response at 1 ng/mL ($p = 0.003$). A slightly increased average frequency shift (91 kHz) was observed for sensors tested with a concentration of 100 ng/mL. A plot of the average frequency shift for sensors (n=8) exposed to 10 ug/mL of the mesothelin-rfc protein is shown in Figure 6.1 which illustrates frequency shifts of 174 kHz for MB-coated sensors and 5 kHz for the reference sensors (p-value < 0.001). For sensors tested with sample concentrations of 50 µg/mL, an average frequency shift of 195 kHz was observed. 50 µg/mL was the highest concentrations for which we could obtain the mesothelin-rfc and therefore was the top-end limit that we were able to test. The sensor testing results from the mesothelin experiments are summarized in Figure 6.2 in the form of a dose-response curve.

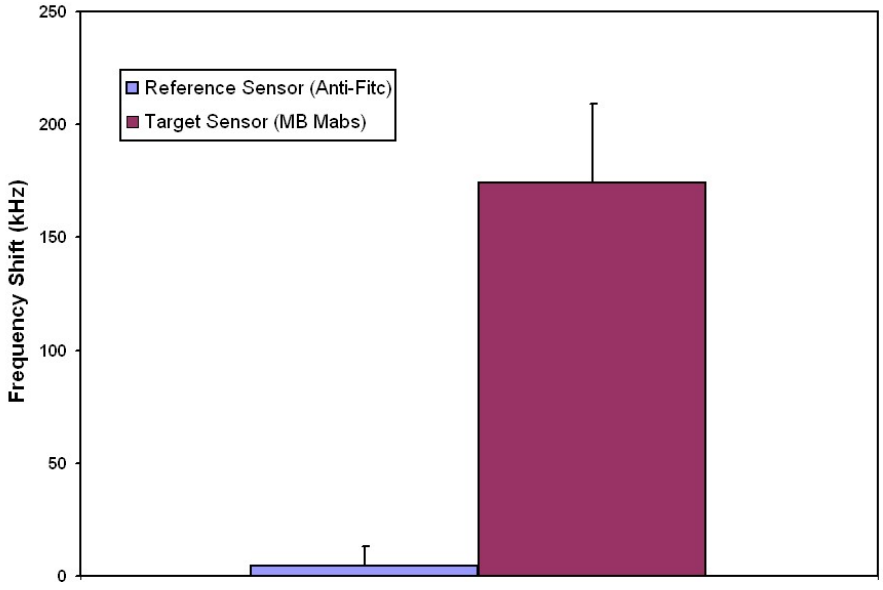

Figure 6.1 The average frequency shift for target and reference sensors exposed to 10 µg/mL mesothelin-rFc in PBS buffer. (Error bars = S.E.)

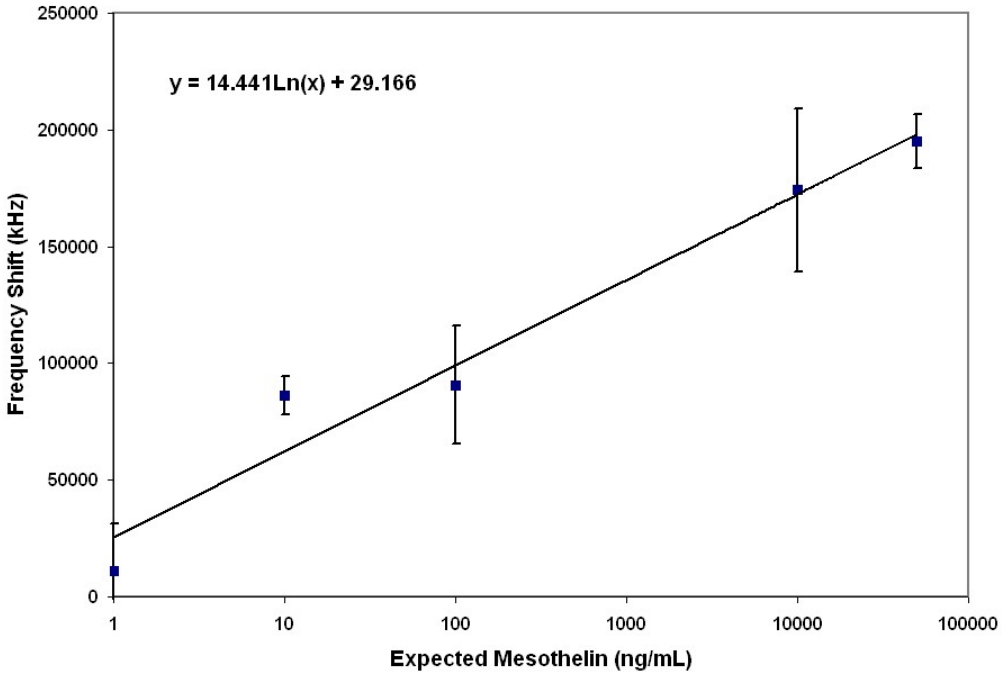

Figure 6.2 The dose response curve developed for the TSM acoustic resonators functionalized with MB antibodies and exposed to varying concentrations of mesothelin-rFc protein in PBS buffer. (Error bars = S.E.)

We found that statistically, there was no difference between the frequency shift observed with the MB-coated devices exposed to the 1 ng/mL solution and that of the reference Anti-fitc coated devices (p-value = 0.769). Therefore, we can conclude that the concentration of 1 ng/mL is the lowest estimate for the detection limit of these sensors for the mesothelin protein. A dose-response curve such as the one developed here could be used for estimating a quantity of mesothelin present in a serum sample similar to the methodology used in the widely-accepted ELISA. The average measured frequency shift after a device or array of devices is exposed to the sample of unknown concentration can then be correlated to an approximate concentration using the graph.

Figure 6.3 shows the average frequency response when sensor arrays were exposed to the LNCaP conditioned medium. The average frequency shift of the Anti-fitc coated sensors was the lowest at 49 kHz. This frequency shift represents the amount of

non-specifically bound protein that may have adsorbed to the surface of the device during the incubation time which was not washed off with the buffer wash. This is the baseline from which to judge the other frequency shifts from since there were theoretically no molecules in the conditioned media that should be bound by the Anti-fitc antibodies. The average frequency shift due to total PSA in the sample was observed to be 84 kHz. To find the true frequency shift due to PSA, we should subtract out the shift observed in the reference sensors to remove the background. This leaves us with an effective shift of roughly 34 kHz above the background reference. This frequency shift can be attributed to the specific binding of PSA molecules to the antibodies immobilized on the surface of the devices.

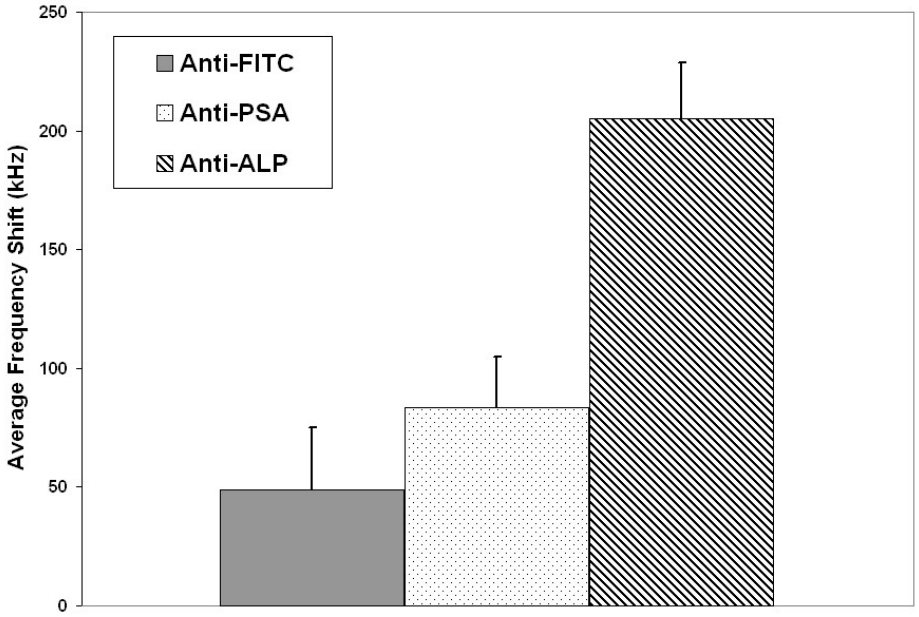

Figure 6.3 The average measured frequency shifts for sensors exposed to LNCaP conditioned medium. (Error Bars = S.E.)

The sensors coated with Anti-alkaline phosphatase antibodies showed a significantly higher shift than the other sensors to be on average 205 kHz (p-value = 0.002). It was expected that the levels of alkaline phosphatase in the conditioned medium would be

elevated as a positive control – an expectation that was supported through experimental results. An example of the impedance response illustrating a parallel resonant frequency shift due to sensor exposure with LNCaP conditioned medium is shown in Figure 6.4. The parallel resonant frequency is the frequency at which the magnitude of the impedance response is at a maximum. A resonant frequency shift can be measured by tracking the location of this peak in the frequency domain either in real-time, or as a before/after measurement.

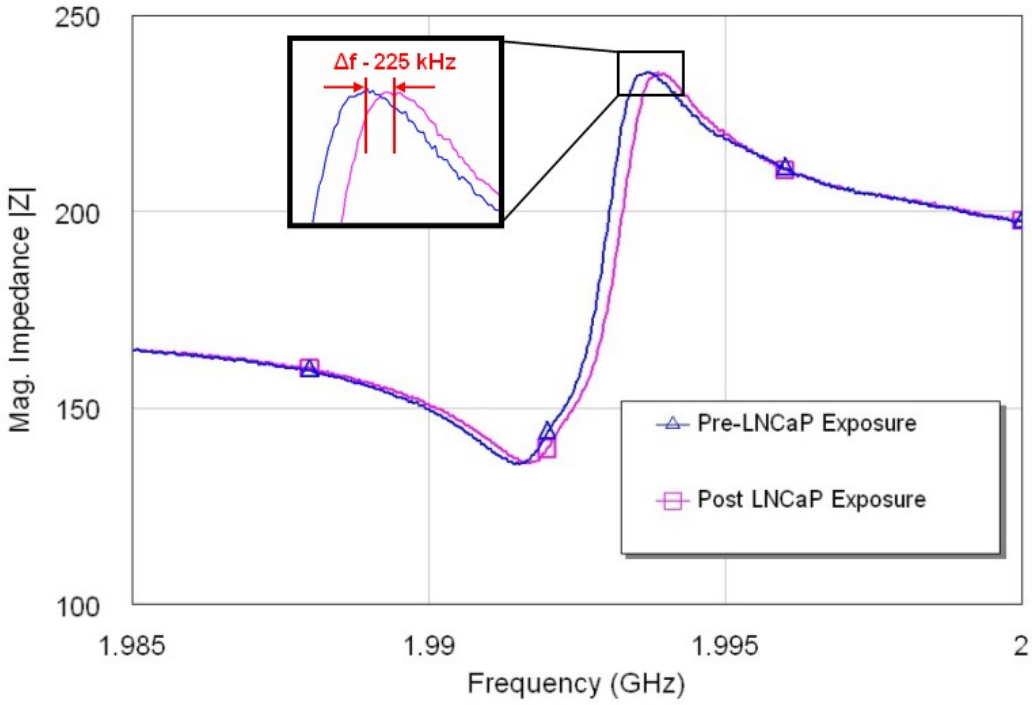

Figure 6.4 The magnitude of the impedance response showing the frequency shift of 225 kHz in the parallel resonance after exposure to the LNCaP conditioned medium.

6.4 Discussion

The results of the sensor experiments indicate that the TSM acoustic resonators are capable of functioning as biosensors for the detection of biological molecules. Testing with known concentrations of purified mesothelin aided the development of a dose-response curve which can be used to estimate the amount of mesothelin present in a sample of unknown quantity given a frequency shift from the sensor array. The development of dose-response curves are a common practice for the development of ELISA tests. The dose-response curve developed here illustrates the sensitivity of the sensors to varied concentrations of mesothelin in liquid-phase samples. The limit of detection for the devices is estimated to be above 1 ng/mL because of the statistical insignificance between the frequency shifts observed at this concentration versus those observed with the reference sensors. This detection limit is likely within the physiological range for mesothelin in the serum of healthy patients and is likely below the range of mesothelin for advanced stage mesotheliomas and ovarian cancers [114]. This is important for the potential usefulness of these sensors for the clinical detection of cancer biomarkers. One key advantage of these sensors is that the magnitude of the frequency shift for a given input quantity is much higher when compared to the QCM experiments, which is attributed to the much higher fundamental operating frequency of the TSM resonators. Average frequency shifts in the range of 50-100 Hz are very common for QCM sensor detection events. However, we observed frequency shifts in the 10s and 100s of kHz when the sensors were exposed to the target sample. However, in order for the sensor arrays to be useful for clinical applications, the sensitivity resolution needs to be improved through further experimentation. Specifically, the average frequency shifts measured for 10 ng/mL and 100 ng/mL concentrations were not shown to be statistically

different (p-value = 0.858). The estimated detection limit seems to indicate that the sensors are sensitive enough for clinical detection of mesothelin, but the resolution must be improved to be on-par with ELISA such that samples with a concentration of 8 ng/mL can be consistently differentiated with samples that have a concentration of say, 15 ng/mL.

While the mesothelin tests were aimed at characterizing the sensitivity and resolution of the TSM resonators, the PSA tests were performed to look at the specificity of the devices by comparing sensor responses for three different targets from a single sample. Additionally, an important aspect of these tests was to illustrate the capability of the sensors to operate in complex media. The results of the tests indicate that alkaline phosphatase and PSA are both present in concentrations that are detectable by the sensors. Additionally, the sensors showed the capability to differentiate between detection of PSA molecules versus Alkaline Phosphatase. This tells us that the antibody immobilization technique is adequate and that the specificity is imparted to the sensor through the antibody.

One of the shortcomings of the study presented here is that we were unable to test the sensor responses in real-time due to the lack of a suitable flow-cell and testing apparatus which is currently being developed. The real-time sensor responses are useful because they provide a time-signature which illustrates the transient response of the sensor to the target solution. This helps to give information about the rate of interaction of the sample with the sensor and can also provide additional data about the stability of the resonance after the shift has taken place. However, the experiments described in this

chapter have shown that even in the absence of real-time sensor monitoring, the devices are quite capable of functioning as highly sensitive and specific biosensors.

6.5 Chapter 6 Conclusions

This chapter has outlined the initial biosensor testing and characterization that has been performed with the TSM acoustic resonators. The sensors were shown to be capable of detecting clinically relevant levels of cancer biomarkers both in pure form as well as in complex media. An estimate of the detection limit for the sensors was provided, and the sensors were shown to react to increasing concentration with increasing resonant frequency shifts. It is concluded that the sensitivity of these devices to molecular recognition is sufficient for general detection. However, we believe that the sensor platform has the potential to be sensitive enough to differentiate between samples containing two similar, but discrete concentrations of the target biomarker. In order to realize this goal, more work still needs to be done to further increase the quality factor of the resonators and control all of the potential sources of error. In future studies, the technology that is currently being developed will aid in improving the sensor studies and will provide more useful data for analyzing the response of multiple sensors in real-time. This will ultimately move the sensor platform towards a clinically useful diagnostic tool.

CHAPTER 7

FILTER NETWORK CONFIGURATION-BASED MULTI-ELEMENT SENSOR

7.1 Introduction

This chapter focuses on describing an innovative sensor system which utilizes acoustic wave device elements in a passive ladder or lattice filter network configuration. The sensor does not require the use of an oscillator for driving the acoustic resonance. The series or shunt elements comprising the ladder structure respond to gravimetric mass deposition events which alter the frequency response of the overall structure. The resulting frequency response can be analyzed to predict the magnitude and the spatial location of the perturbation. Simulations were performed based on a Butterworth-Van Dyke circuit model. The results indicate that perturbations of the shunt and series resonator elements affect the overall frequency response, thereby making the filter network useful as a multi-element sensor. The simulation results are corroborated through initial experimental testing on ZnO-based ladder filters. The shunt resonator elements of the filters are loaded with known mass quantities and the resulting frequency responses are measured and compared.

7.2 Sensor System Description

One problem with the traditional approach to acoustic resonator sensor system design is that an oscillator circuit is required to drive the acoustic device at its resonant frequency. Because of the fixed operating bandwidth of an oscillator circuit, devices operating at radically different non-harmonic frequencies cannot be driven by the same oscillator circuit. This is a significant restriction during the design and testing stage of acoustic sensor development. Further, one of the forefronts of acoustic sensors research is exploration into the use of multi-device arrays [118, 119]. For example, an array of multiple sensors, each designed to sense a different biological marker, could be highly effective in screening for diseases like cancer or sepsis where the expression level of a single biomarker is often not conclusive for diagnosis. As discussed in Chapter 6, through the use of a multi-element array the expression level of multiple biomarkers could be measured resulting in a much more robust and reliable screening test.

Oscillator-based sensor detection systems implementing acoustic wave devices as part of the feedback element present four significant concerns in their operating characteristics, especially if more than one acoustic wave device is used. The first concern involves the stability of the oscillator due to the thermal drift and load pulling of the amplifier portion of the circuit. The second concern is the instability due to possible coupling of modes between adjacent acoustic wave devices that would introduce injection-locking phenomena from stray coupling within the oscillators. An oscillator "averages" any frequency or time related anomaly associated with a sensed substance. Further, the transient and settling times associated with oscillators make high speed

switching between devices difficult and a separate oscillator for each device in an array is not cost-effective nor does it lend itself to system miniaturization.

This chapter describes a novel sensor system that improves on previous efforts of implementing multiple arrays of sensors by introducing a new type of arrangement that incorporates multiple narrow-band devices within its own structure. This structure is passive to eliminate any instabilities and transients found in active circuits, eliminates averaging effects found in oscillator sensor circuits, introduces a means to include sensed information obtained over a swept frequency range, and can be readily adapted for multiple array sensor applications. The composition of this structure involves cascading individual resonant structures, which could in general include micro-electrical-mechanical-systems (MEMS) such as thin film bulk acoustic resonators (FBARs), surface acoustic wave resonators and other acoustic wave resonators such as bulk acoustic wave (BAW), leaky surface acoustic wave (LSAW) and other known acoustic modes of propagation. A system such as the one presented here provides the utility of acoustic biosensor arrays without the problems associated with oscillator-based systems. Simulated results show that the narrow-band resonant elements comprising the array structure respond to perturbations placed upon each element. The location of the perturbation in the multi-element array determines the overall wider-band frequency response. By monitoring frequency shifts among characteristic peaks in the overall response, the location of any individual element response can be determined.

Communication systems including digital radios have implemented ladder and lattice type structures as filters for some time now [120, 121]. These filters consist of interconnected series and shunt resonators that form a monolithic structure on a single

die. High performance band-pass filters using both FBAR and SAW devices have already been demonstrated with insertion losses below 3 dB [122, 123]. Numerous publications describe how these acoustic wave ladder and lattice structures have benefited the communications industry [124, 125]. One advantage of implementing acoustic wave ladder and lattice structures is the reduction of coupling between individual series and shunt resonators. Unlike inductor based or cavity type of ladder or lattice filters where stray electromagnetic coupling would influence the frequency response, the acoustic coupling is kept to a minimum when proper layout procedures are followed. A similar approach is now taken with this multi-element acoustic wave resonator network for application within the sensor industry. Fig. 7.1 illustrates a typical ladder structure equivalent circuit constructed from several separate narrow-band resonator elements. The circuit consists of both series and shunt resonators. Each of the series resonator elements are individual narrow-band resonators fashioned such that they operate at resonant frequency f_o. Similarly, each of the shunt resonator elements are individual narrow-band resonators designed for resonance at a frequency f_1, which is offset slightly from frequency f_o. When combined into a filter network, series and shunt resonator elements operating at offset frequencies result in a much wider passband response rather than a narrow-band notch response that would be expected for a single resonator.

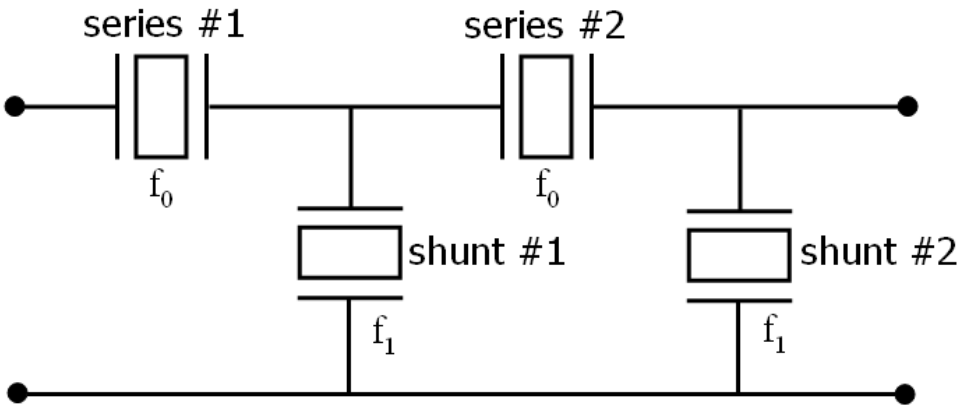

Figure 7.1. Typical ladder structure configuration. The series elements resonate at a frequency of f_o while the shunt elements resonate at a frequency of f_1

While the depicted network includes only four elements, practical implementation of a ladder network could involve many more series-shunt pairs depending on the application. The series or shunt elements of the ladder sensor structure can be configured to independently measure a chemical or biological effect by coating each individual element with a different molecular recognition element (MRE) such as an antibody. By increasing the number of series-shunt pairs, more individual resonators are available for use as sensors for detecting different biological targets of interest, or for providing redundancy in the measurement of a single target. This could be of use for the detection of a disease such as sepsis where the presence of multiple biological targets in the breath is of interest to physicians.

Sepsis is a cascading failure of organ systems, usually initiated by infection of the blood, then exacerbated by a massive, injurious inflammatory response. A sensor system that can detect multiple biomarkers simultaneously from the subject's breath could be of great use for providing physicians with enough information to prevent disease progression. The signaling biomarkers that indicate the onset of sepsis include

endothelin-1 (ET-1), erythropoietin (EPO) and tumor necrosis factor-alpha (TNF-alpha) as well as lipopolysaccharide (LPS), a bacterial wall component. The series and shunt resonators that comprise the ladder or lattice structure can be configured to collectively measure multiple physical, chemical and biological effects simultaneously in order to identify or characterize a specific event or condition of the presented sample.

A common design requirement for filters in the communications industry is a smooth passband, in which all signals within the desired frequency band are passed with approximately the same attenuation. In a typical communications ladder filter design, the zero of the series resonator must be directly aligned with the pole of the shunt resonator along with other matching techniques to ensure a flat passband. The tolerance for the resonant frequencies of the components is typically very stringent, which reduces overall manufacturing yield. For sensor applications, however, a smooth passband should not be required. In fact, a novel feature of the proposed sensor system is that a smooth passband is actually less desirable due to the fact that the ripples in the passband are perturbed during the sensing events and provide additional information in the detection process. This implies that fabrication tolerances can be relaxed and overall production costs could be reduced in mass production.

As previously mentioned, each narrow-band resonator element in the ladder structure is sensitive to perturbations that will result in an operating frequency shift of the device. When a ladder network is exposed to a sample under test, resonator devices in that structure will be perturbed based on the presence of the molecules for which each device is specifically targeted. Specifically, this would occur through the highly specific binding activity of immobilized antibodies. This will cause the operating frequency of the

specific element resonator in the network structure to shift. Since the overall frequency response of the ladder network is dependent upon the operating frequency of each of the resonator components, a shift in the operating frequency of any or all of the resonators will result in an overall filter response that will be comprised of new features (ie. peaks and valleys) that will be different from the original unperturbed frequency response. When probed over a span of frequencies, the new perturbed frequency response can be measured. This response can be used in identifying sensor detection events when compared to the original unperturbed response.

7.3 Equivalent Circuit Modeling

To illustrate the effects of series or shunt resonator mass loading on the overall frequency response, ladder filter networks were modeled using the software program Microwave Office (Applied Wave Research, Inc). Butterworth-Van Dyke (BVD) circuit models shown in Fig. 7.2 were used to simulate each resonator element in the ladder structure. The BVD model is one of many electronic circuit representations of a resonator. It has been widely used in a variety of forms throughout the literature as a representation for an acoustic resonator [126, 127]. In the simplest form, the BVD model contains a constant clamped capacitance, C_0, which represents the inherent capacitance of the structure. The clamped capacitance is in parallel with a motional arm consisting of a motional inductance, L_m and motional capacitance, C_m. The motional components in this model represent the electromechanical response of a piezoelectric material. The BVD model shown in Fig. 7.2 represents a lossy resonator because it makes use of a motional

resistance, $R_{m,}$ which provides for energy absorption in the device as a result of acoustic attenuation.

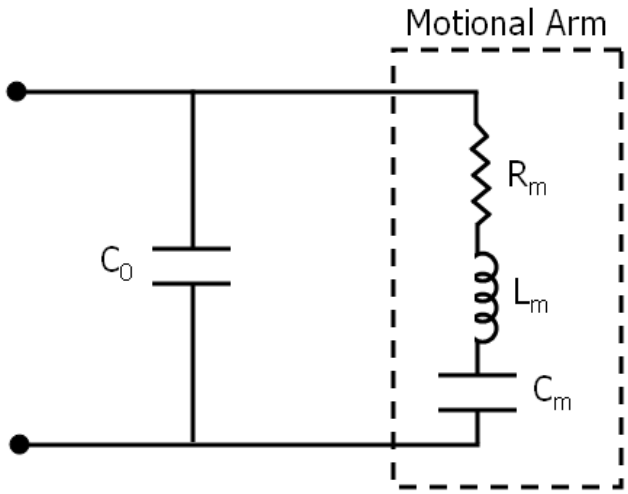

Figure 7.2 Butterworth Van-Dyke equivalent circuit for a resonator with acoustic attenuation represented by the motional resistance element (R_m).

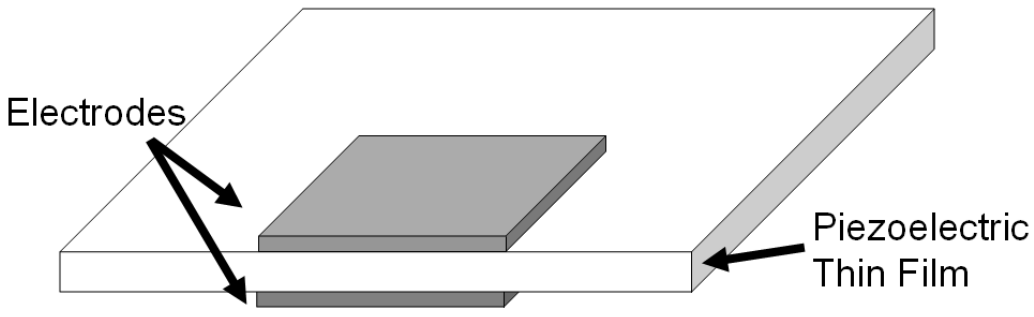

Figure 7.3 Device configuration of the resonator devices simulated using the BVD model. The schematic illustrates the thickness excitation electrode configuration on the surface of a planar ZnO thin film.

The individual resonator structure chosen to simulate using the BVD model is a thin-film FBAR resonator operating in the longitudinal mode with a thickness excitation electrode configuration shown in Fig. 7.3. However, the network configuration described in this chapter is not limited to BAW devices and can be configured to accommodate a variety of narrow-band acoustic resonators, including SAW devices, and other MEMS devices. The devices that are simulated using the BVD model consist of a thin-film modeled as piezoelectric *c*-axis oriented ZnO with electrodes placed on either surface of the film. The value for C_0 in the BVD model represents the clamped capacitance of the device configuration. For an FBAR configuration, this is simply defined by the equation for a parallel plate capacitor [17] :

$$C_0 = \frac{\varepsilon_r \varepsilon_0 A}{d} \tag{1}$$

where A is the area of the electrodes, d is the thickness of the thin-film, and ε_r is the relative permittivity of the film. For a bulk acoustic wave resonator, the thickness of the ZnO film is related by the frequency through the relation:

$$d = \frac{v_a}{2 f_0} \tag{2}$$

where v_a is the acoustic wave velocity. From the calculation of C_0, we can obtain C_m for the fundamental harmonic through the relation

$$C_m = \frac{8 C_0 K^2}{\pi^2} \tag{3}$$

where K^2 is the coupling constant. From this value of C_m we can determine the value of the motional inductance from the resonant frequency which is determined according to the thin-film thickness and the acoustic wave velocity:

$$f_0 = \frac{1}{2\pi\sqrt{L_m C_m}} \tag{4}$$

The motional resistance, R_m is related to L_m through the quality factor (Q) at a specified frequency:

$$R_m = \frac{2\pi f_0 L_m}{Q} \tag{5}$$

where the Q of a resonator is a measure of the energy stored over the energy dissipated per cycle.

A ladder filter network similar to the one shown in Fig. 7.1 was developed using BVD circuit representations for each of the resonator elements. The circuit was comprised of three shunt elements and nine series resonators resulting in eight total elements as compared to the ladder structure depicted in Fig. 7.1 which consists of only four total elements. In a typical pass-band filter network, the resonators would be designed such that the parallel frequency of the shunt resonators align with the series frequency of the series resonators. However, in the model developed here, the parallel and series frequencies of the resonators were intentionally misaligned resulting in passband ripple to illustrate its utility in aiding detection. The physical parameters of the devices used to calculate the circuit components for the shunt and series resonators are shown in Table 7.1. The acoustic velocity v_a is based on extracted values from *c*-axis oriented ZnO longitudinal devices [14]. The Q value of 700 is an estimated value for a device with the parameters in Table 7.1 based on experimentally measured Q values of

similar devices. The coupling value for K^2 (8%) is based on theoretical calculations for the thickness excited longitudinal ZnO resonator as described by Rosenbaum [17].

Table 7.1 Parameters of the simulated longitudinal ZnO resonator devices

Parameter	Value
Electrode Area (A)	1.76×10^{-8} m^2
Quality Factor (Q)	700
Coupling Constant (K^2)	0.08
Acoustic velocity (v_a)	6,300 m/s
Relative permittivity (ε_r)	10

A series of simulations were performed to explore the effects of loading various series and shunt elements of the ladder structure and to observe the change in the frequency response of an 9-element ladder filter. The unperterbed series and shunt resonators were modeled with series frequencies of 1.8 GHz (f_0) and 1.71 GHz (f_1), respectively. In the circuit model, this perturbation was simulated by increasing the ZnO thickness value which results in modification of the BVD circuit element values to correspond to a shifted frequency below the initial operating frequency of the series and shunt resonators resonators. S_{21} responses were simulated for the perturbed and unperturbed cases and the responses were plotted.

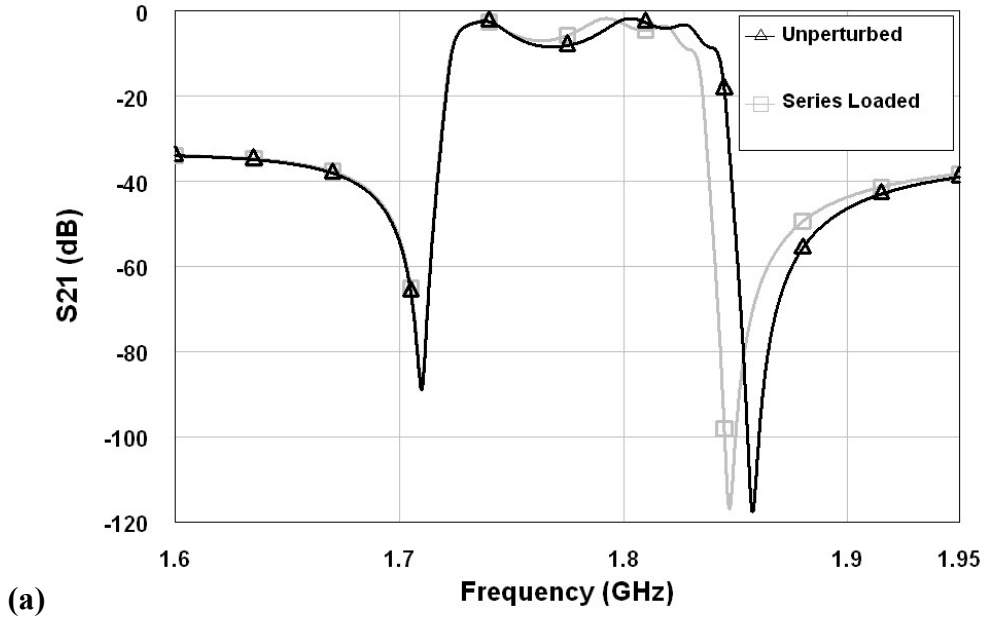

(a)

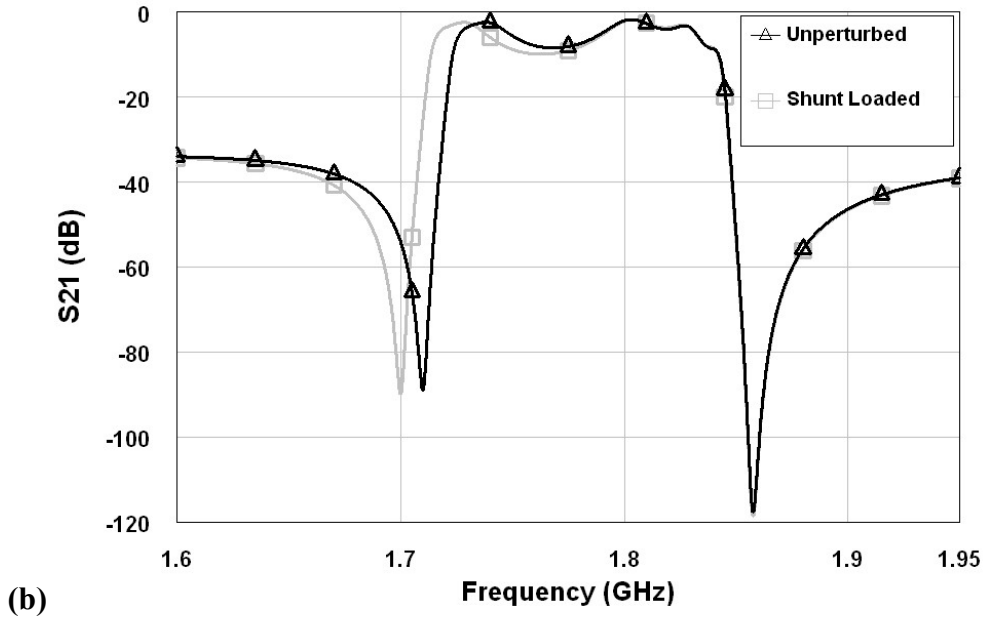

(b)

Figure 7.4. The effects of perturbing the (a) series and (b) shunt resonators on the overall frequency response as compared to the unperturbed network

The results of modeling series and shunt perturbations on the multi-element ladder frequency response are illustrated in Fig. 7.4. The curve denoted with triangles in Fig. 7.4a and b is the frequency response from the unperturbed circuit. This is the basis from which to compare the perturbed response from. The curve denoted by diamonds in Fig.

7.4a represents the frequency response (S_{21}) when only the narrow-band series resonators are perturbed. In the circuit model, the perturbation was simulated by increasing the ZnO thickness value which results in modification of the BVD circuit element values to correspond to a shifted frequency (f_0) 10 MHz below the initial operating frequency of the series resonators. Similarly, Fig. 7.4b represents the frequency response when only the shunt narrow-band resonators are perturbed. The perturbation was also simulated by modifying the ZnO thickness value resulting in modification to the BVD circuit elements to correspond to a shifted frequency 10 MHz below the initial operating frequency (f_1) of the shunt resonators. While a typical acoustic resonator operating at 1.8 GHz may not actually shift by as much as 10 MHz as a result of molecular binding, this large shift was used to illustrate the effects of mass loading on the overall response. The exaggerated frequency shifts were implemented to illustrate to the reader how the overall filter response can be affected by differential loading of each of the ladder structure elements. The series-element response in Fig. 7.4a illustrates that perturbation of the series devices (diamonds) will affect the overall response by decreasing the upper cutoff frequency of the passband relative to the unperturbed case (triangles) by approximately 10 MHz, thereby decreasing the overall passband width.

Similarly, when shunt resonator loading was simulated by a 10 MHz resonance shift, the response shown in Fig. 7.4b illustrated a different shift in the response relative to that of the unperturbed case. The upper cut-off frequency region remains relatively unchanged while the response below the upper passband edge begins to show a difference between the unperturbed response (triangles) and the perturbed response (squares). The lower cut-off frequency is shifted downwards by approximately 10 MHz corresponding to the

simulated perturbation thereby increasing the overall passband width. The frequency responses of Figs. 7.4a and 7.4b follows with ladder filter design theory where the low-frequency side notch is determined by the series resonance of the shunt resonator(s) and the high frequency notch is determined by the parallel resonance of the series resonator(s) [128]. In Fig. 7.4b, the upper cut-off frequency for the perturbed case matches that of the unperturbed case because only the shunt resonators have undergone a simulated loading. By looking at differences in the location of the upper and lower passband cutoff frequencies, it is possible to determine whether shunt or series elements have been perturbed. A measurement of the difference between the perturbed response and the unperturbed reference response would correlate to the amount of perturbation that took place on the elements of the perturbed 9-element ladder structure and could be quantified using appropriate methods such as the Gordon-Kanazawa equation for thickness shear mode resonators [129].

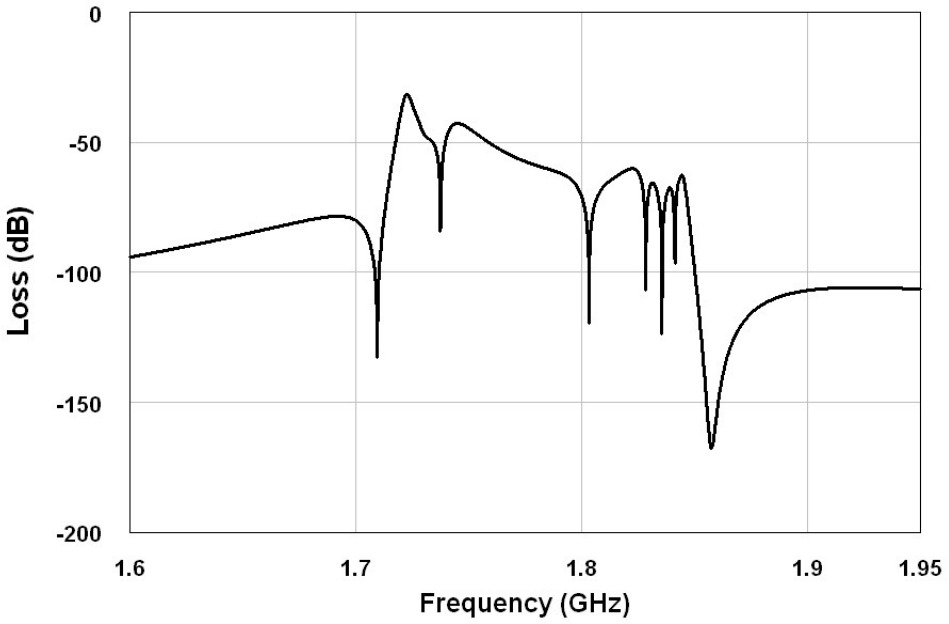

Figure 7.5. Calculated difference between the unperturbed and loaded shunt resonator response with 274 kHz shift simulating mass loading

To illustrate a more realistic frequency shift for mass sensing experiments performed with an acoustic resonator, a shunt loading simulation to reduce the frequency of the shunt resonator by only 274 kHz (0.016% of f_1) was performed, as opposed to 10 MHz (0.58%) in the previous example. Fig. 7.5 illustrates the difference between the response of the 9-element ladder structure with shunt loading and that of the unperturbed reference ladder structure. This difference response was calculated by subtracting the magnitude of the unperturbed S_{21} frequency response from the magnitude of the perturbed frequency response. Even with a very slight shift in frequency in the two-shunt element resonator structures, very distinct peaks can be observed in the resulting response. The difference response of Fig. 7.5 illustrates that the high-side frequencies remain about the same when the shunt elements are perturbed therefore resulting in a virtual zero (-150 dB) values. The signal associated with the passband frequencies varies in magnitude from –40 dB to about –100 dB which are detectable numbers using digital radio receiver techniques.

Simulations were also performed with four-device networks similar to the one shown in Fig. 7.1. However, rather than configuring the shunt resonators to operate at f_1 and the series resonators to operate at f_0, if we configure Series #1 to operate at f_1 and Shunt #2 to operate at f_0, the frequency response is drastically different and shows 4 separate "notches" which each corresponding to the series or parallel resonant frequency of an individual resonator within the structure. Figs. 7.6a and 7.6b illustrate the effects of individually perturbing the two series resonators and two shunt resonators, respectively. Simulations indicate that we can design a frequency response so that the frequency of 4 separate sensors can be individually monitored simultaneously in a passive network

configuration. In a practical biosensor implementation, each resonator can be individually functionalized to detect a different biomarker in a complex sample. With the proper circuitry, the resulting frequency response can be measured in real-time during sensor experiments and the response of multiple sensors can be read simultaneously without the need for complicated switching schemes or oscillators.

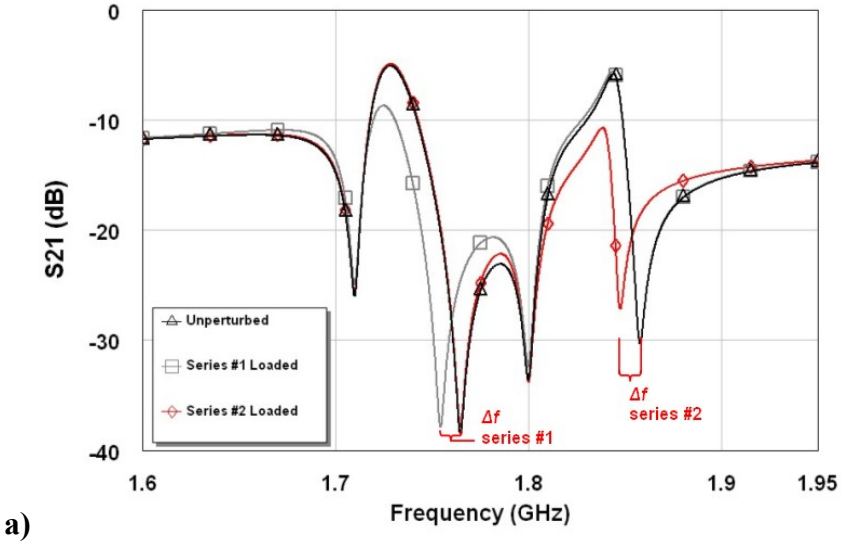

a)

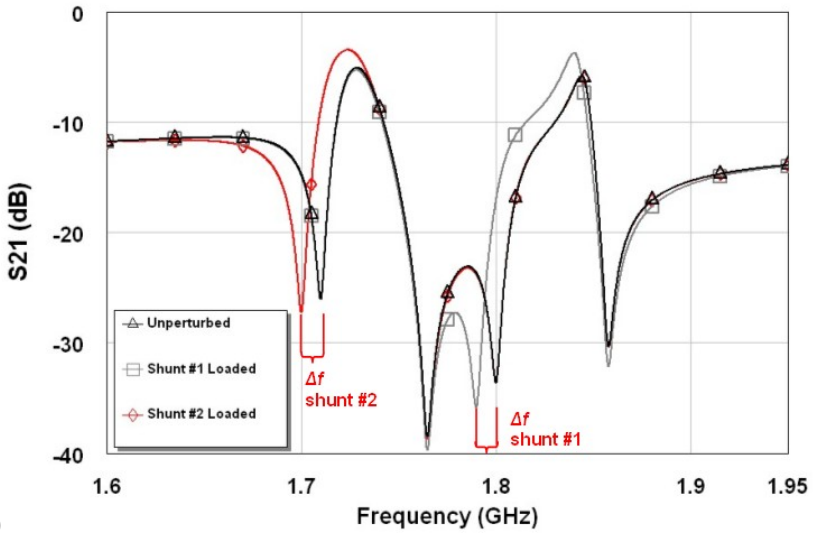

b)

Figure 7.6 Simulation results of the modified ladder network showing the frequency shift resulting from (a) perturbation of series #1 (f_1) and #2 (f_0) resonators independently and, (b) perturbation of the shunt #1 (f_0) and #2 (f_1) resonators independently

7.4 Experimentation

In order to test the simulation results experimentally, solidly mounted resonator ladder filters were fabricated using a standard photolithographic process. Metallic thin-film deposition was chosen as the method for perturbing the resonators experimentally because the CVC system allows for a known amount of mass to be deposited in a controlled manner. This method, as opposed to testing with biological molecules is more suitable for initial characterization because it can be more easily controlled and monitored.

The fabricated devices consist of an acoustic reflector of alternating layers of quarter-wavelength Ta_2O_5 and SiO_2 thin-films on top of a Si wafer. Ta_2O_5 and SiO_2 were deposited by RF magnetron sputtering using a Unifilm PVD-300 sputtering system. The acoustic reflector was implemented to provide isolation of the acoustic wave from the silicon substrate and improve device Q.

Following deposition of the acoustic reflector, the bottom electrodes were patterned and a 200 nm seeding layer of Cr followed by 1300 nm of Au was deposited using a CVC e-beam evaporator. After liftoff, c-axis oriented ZnO was deposited using RF magnetron sputtering in the Unifilm system. Following ZnO deposition, the top electrode layer (also 200 nm Cr and 1300 nm Au) was deposited on the surface. In order to create a wide bandpass response, an additional 200 nm of Cr and 600 nm of Au were deposited on the shunt resonators.

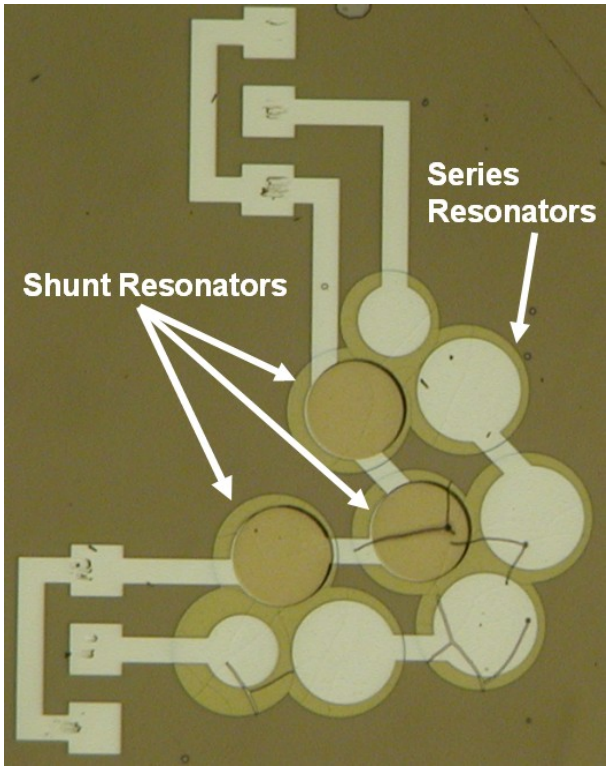

Figure 7.7 A digital image of the 9-element ladder filter

The ZnO-based ladder filters were comprised of 9 separate devices operating in the longitudinal mode. A picture of the ladder network electrode configuration is shown in Figure 7.7. All S_{21} measurements were made using an HP8753C vector network analyzer equipped with an S-parameter test set. The filter responses were collected initially in order to establish the unperturbed frequency response. Then, the shunt resonators were masked using photolithography so that only the shunt resonators were exposed, and metal of varying thickness was deposited onto the resonators using e-beam evaporation. Following a lift-off procedure which left the deposited metal only on the shunt resonators, the S_{21} response of the devices was again collected. The resulting S_{21} responses were analyzed and compared.

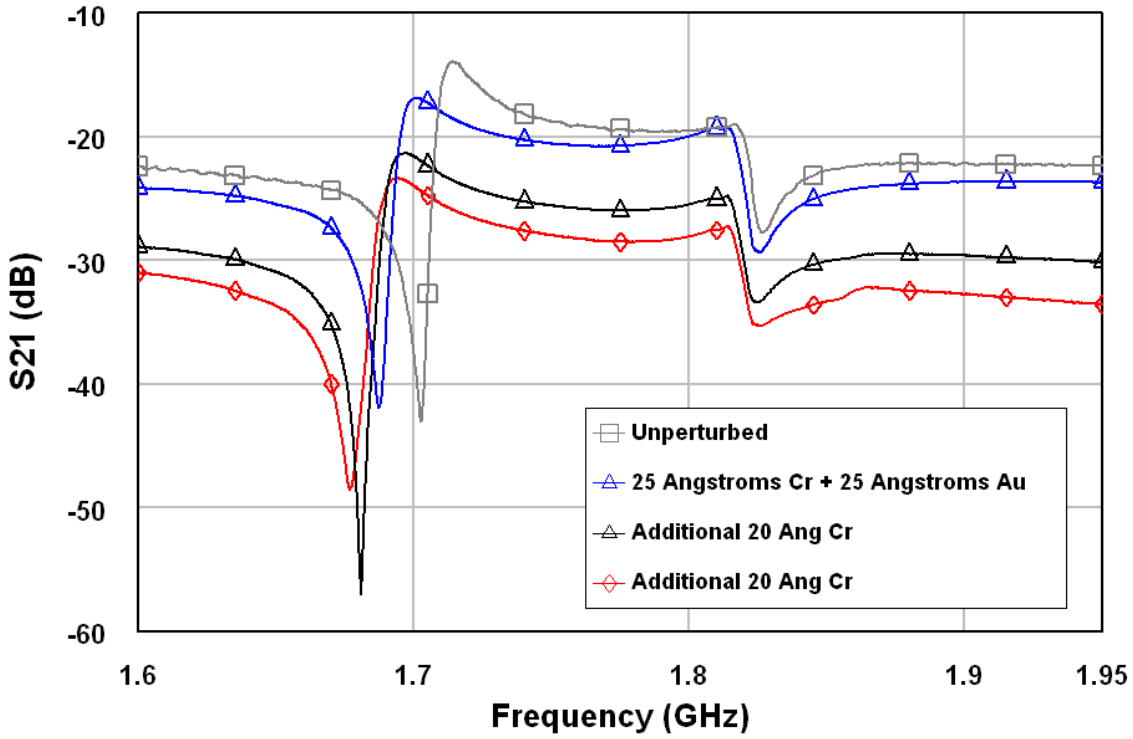

Figure 7.8 The S_{21} responses of a fabricated ladder filter illustrating the effects of stepwise mass loading of the shunt resonators on the overall passband response.

Results from the experimental investigations are provided in Figure 7.8. The plot shows the frequency response of a ladder filter network as it changes with step-wise mass deposition on the shunt resonators. The measured filter responses are depicted before and after the deposition of 25 Å of Cr and 25 Å of Au as well as after two subsequent depositions of 20 Å of Cr. We observe that the high frequency side of the passband stays relatively the same. However, after each deposition of mass, significant frequency shifts can be observed in the location of the lower cut-off frequency notch. This agrees well with the results from the simulations depicted in Fig. 7.4b. The upper and lower passband cutoffs as well as the features of the passband response depend upon the frequencies at which the resonators comprising the network operate. As a result, it is possible to make inferences based on the frequency shift of these features about the amount of mass

deposited and the spatial locations of the mass deposition. By tracking the locations of the upper and lower passband cutoff frequencies as well as the peak/notch features in the passband, it is possible to determine both the magnitude of the shift, and whether or not the perturbation occurred in the series or shunt resonators.

In the sensor experiments, the deposition of 20 Å of Cr amounted to a shift in the lower passband frequency on average, of approximately 5 MHz. The diameter of the shunt resonators is roughly 150 μm. If we assume that the density of Cr is 7.2 g/cc we can approximate the amount of mass that was deposited onto each of the resonators which works out to be roughly 0.25 ng of metal deposited per resonator. With three shunt resonators, we have roughly 0.75 ng of metal deposited per ladder network. A rough estimate of sensitivity of this structure to mass loading on the shunt resonators is then approximately 6.5 kHz/pg.

7.5 Discussion

One of the most important aspects of detection verification for acoustic sensors is the use of a reference sensor. Acoustic resonators used in biosensor applications are susceptible to changes in temperature, pressure, viscosity, and electrical conductivity among other factors in the fluid or vapor sample. The use of a reference sensor allows for subtracting out non-specific factors from the overall response leaving only the signal resulting from the various specific detection events. The ladder system can easily be modified to include a reference network located in proximity to the targeting network. A set of two separate multi-element structure configurations could be coated with antibodies specific to one or more different molecular targets. The shunt resonators would be coated with antibodies specific to target 1, while typically, the series resonators

would be coated with antibodies specific to target 2. The second, lower, ME network would then have the purpose of providing a reference signal.

The implementation of this sensor network was carried out experimentally by stimulating the multi-element structure configuration with a frequency sweep from a network analyzer. However, another method of providing this frequency stimulus is to construct a SAW frequency modulated (FM) chirp generator [130], where the output of the multi-element structure configuration functions as the input to a mixer. The mixer utilizes another signal input from a voltage controlled oscillator (VCO) to produce a modified down-converted signal at a lower frequency range than the resonant frequencies, f_o and f_1, of the multi-element structure configuration. This down-converted signal is then suitably conditioned, sampled and digitized within the sampling and digitizing system. The binary equivalent of the down-converted signal then acts as the input to a digital processor. This processor can then implement a suitable algorithm to detect the magnitude and phase features of the frequency response characteristics of the multi-element structure configuration or any subsequent changes to this response. The frequency response of each network (if multiple are implemented) could be compared to its unperturbed initial frequency response that would be digitally stored at prior to exposure to any fluid or vapor samples. The switching system would be controlled to continuously switch between the multi-element structures to record changes in the frequency response as the molecular recognition events occur. With the proper implementation of display and processing algorithms, a near real-time detection system could be implemented.

7.6 Chapter 7 Conclusions

In this chapter, we have proposed the basis for a multi-element acoustic sensor system that is not oscillator-based, but rather employs ladder and lattice type structures. It offers an alternative to traditional oscillator-based sensor systems by eliminating the commonly associated problems such as oscillator stability, extended settling times and loss of information due to averaging within the oscillator loop. By interrogating such structures with a swept frequency stimulus, the identification and characterization of certain physical, chemical and biological effects can be made. This system also minimizes the use of active components and can sense the physical, chemical and biological effects over a broader frequency range. Through BVD circuit modeling, it was illustrated that the operating frequency variation within the individual narrow-band resonator elements will affect the overall wider frequency response of the ladder structure. By comparing the difference between the perturbed frequency response with that of a reference frequency response, changes between the responses can be easily monitored which indicate perturbations of the individual targeting components. The sensitivity of a ZnO-based 9-device ladder structure was tested with the deposition of small amounts of mass on the surface. The experimental results corroborate the theoretical findings indicating that the effects of mass loading on the individual resonators that comprise the network manifests itself in the passband response of the entire network.

CHAPTER 8

CONCLUSIONS

This research was aimed at developing and exploring a ZnO-based acoustic sensor platform for molecular detection. Through the use of standard photolithography and microelectronic fabrication techniques, the goal was to produce a sensor capable of molecular detection on the order of the QCM or even greater while introducing an array configuration. The standard fabrication techniques employed here provide a low cost per-chip solution that has implications for disposable sensor testing. Original contributions made by the author include:

- Development of finite element models capable of predicting particle displacement for the QCM and ZnO LFE TSM resonators. [1]
- Theoretical analysis of the conditions for excitation of a TSM in *c*-axis oriented ZnO. [1]
- Theoretical and experimental evaluation of an acoustic reflector structure for a TSM resonator. [1]
- Experimental development and testing of a lateral field excitation TSM ZnO resonator. [2]

---

[1] [14] C. D. Corso, A. Dickherber, and W. D. Hunt, "Lateral field excitation of thickness shear mode waves in a thin film ZnO solidly mounted resonator," *Journal of Applied Physics,* vol. 101, pp. 54514-1, 2007.

[2] [131] C. D. Corso, A. Dickherber, and W. D. Hunt, "A thickness shear mode zinc oxide liquid sensor with off-axis excitation," Atlanta, GA, USA: IEEE, 2007, pp. 931-3.

- Exploration of typical longitudinal electrode configurations for exciting the thickness-shear mode in ZnO. [3]
- Development and investigation of surface chemistry protocols for immobilizing antibodies to the surface of the ZnO. [4]
- Testing the resonators as biosensors for the detection of mesothelin and PSA in complex media. [4, 5]
- Modeling and experimental investigation of a new type of passive sensor network structure based on ladder/lattice filter networks. [6]

8.1 Summary of Results

Before the development of a new sensor platform commenced, a series of proof-of-concept experiments were performed to investigate the application of thickness shear mode resonators to cancer biomarker detection in complex media. Tests were carried out with QCMs in pancreatic cancer cell line supernatant for the detection of mesothelin. The results indicate that the QCMs were capable of detecting mesothelin in the supernatant even in highly dilute solutions. A dose-response curve was developed which related the

---

[3] [14] C. D. Corso, A. Dickherber, and W. D. Hunt, "Lateral field excitation of thickness shear mode waves in a thin film ZnO solidly mounted resonator," *Journal of Applied Physics,* vol. 101, pp. 54514-1, 2007, [131] C. D. Corso, A. Dickherber, and W. D. Hunt, "A thickness shear mode zinc oxide liquid sensor with off-axis excitation," Atlanta, GA, USA: IEEE, 2007, pp. 931-3.

[4] [132] C. D. Corso, A. Dickherber, and W. D. Hunt, "An investigation of antibody immobilization methods employing organosilanes on planar ZnO surfaces for biosensor applications," *Biosensors & Bioelectronics,* 2008.

[5] [12] C. D. Corso, D. D. Stubbs, S. H. Lee, M. Goggins, R. H. Hruban, and W. D. Hunt, "Real-time detection of mesothelin in pancreatic cancer cell line supernatant using an acoustic wave immunosensor," *Cancer Detect Prev,* vol. 30, pp. 180-7, 2006.

[6] [133] C. D. Corso, P. J. Edmonson, A. Dickherber, and W. Hunt, "A multi-element acoustic wave device sensor based on a filter network configuration," *Sensors & Actuators A,* 2008.

net frequency shift of the sensors to the concentration of the supernatant in the sample under test.

To validate the use of an FEM software package for modeling piezoelectrically driven acoustic resonators, a model of the well-studied QCM resonator was developed. The modeling results indicate that an accurate model of the QCM was developed using the Comsol multiphysics FEM software package which took into account the stiffness, piezoelectric, and permittivity tensors of the AT-cut quartz material. The thickness shear mode particle displacement was observed with a defined thickness excitation electric field. This result validated the modeling process for the development of ZnO-based models.

A theoretical treatment of acoustic wave propagation in ZnO was provided through the use of the Christoffel equation. The piezoelectrically stiffened form of this equation was solved in order to elicit the acoustic modes that can be electrically stimulated using a lateral excitation field. It was found that three thickness modes (two shear modes and one longitudinal mode) exist in thin-film *c*-axis oriented ZnO. However, only one of the shear modes is piezoelectrically coupled. The particle displacement was found to be parallel to the electric field while the non-coupled shear mode was found to have orthogonal particle displacement in the x-y plane. The longitudinal mode was also found to be uncoupled to a lateral excitation field but is widely known to be activated by a thickness excitation electric field. The results of the theoretical treatment were verified through the development of a finite element model which implemented a lateral field excitation electrode configuration. The model predicted that shear mode particle displacement could be excited with a variety of electrode configurations including two

plane-parallel electrodes as well as a paired configuration of top and bottom plane-parallel electrodes. An analysis of the electric field generated by the electrode configurations showed that the field is primarily laterally oriented through the ZnO thin film between the two electrodes. The modeling results provided sufficient theoretical evidence to spur the experimental development of the resonators.

One of the most important aspects in the development of a functional solidly mounted resonator is the acoustic reflector. If the acoustic reflector is not designed correctly or implements materials with a poor impedance mismatch, the device will likely not resonate at all. It was discovered that an acoustic mirror comprised of tungsten and silicon dioxide had a favorable acoustic impedance mismatch for the shear resonance in ZnO. Experimentally, the acoustic reflector was found to effectively sustain the TSM resonance with 6 and 8 layer reflector structures with each layer being a quarter-wavelength thick at the resonant frequency.

Resonators comprised of a thin-film of sputtered ZnO deposited on top of an 8-layer acoustic mirror were fabricated. A variety of electrode configurations were tested and the resulting devices were analyzed based on Q and the piezoelectric coupling constant. It was found experimentally that the straight electrode configurations tended to have higher Q, on average, than the circular electrode configurations while the former exhibited higher piezoelectric coupling. Since the ability to track a resonant frequency shift is dependent upon the Q of the resonator, we chose to focus on devices with the straight electrode configuration. The devices were found to operate reasonably well and responded to water loading with only partial reduction of the acoustic resonance. 8-device arrays were developed and tested for susceptibility to ionic solution concentrations

and the effects of the array configuration on device Q. We found that the array configuration did not significantly affect the device Q. Testing indicated however, that the noise level increased with increased ionic concentration of the sample under test.

The development of a surface chemistry capable of linking antibodies to the ZnO surface was a necessary task in the development of the TSM biosensors due to the active acoustic area being located between the electrodes rather than under the electrodes as is the case with QCMs. The surface chemistry protocols developed here involve the use of organosilanes and phosphonic acids for functionalizing ZnO. A crosslinking molecule was used to functionalize thiol-terminated molecules to make them more reactive towards immobilization of antibodies. The protocol employing MTS and GMBS was found to give the highest surface coverage and uniformity. The protocol employing MPA with GMBS also provided high surface coverage of antibodies. The GPS protocol does not require the use of a crosslinker, but was found to provide the lowest surface coverage of the three. This was the first investigation (to our knowledge) of any studies performed for immobilizing antibodies to a planar ZnO surface.

The next step after producing functional resonators and developing the surface chemistry to transform them into molecularly specific biosensors was to test the detection capabilities with clinically relevant markers. A dose-response curve was developed using serial dilutions of purified mesothelin-rFc protein. The results of the tests indicate that the sensors have a limit of detection that is on the order of clinically relevant concentrations, but require further development for improving the mass resolution to differentiate between samples with slight differences in target concentration. PSA testing helped to illustrate the specificity of the sensors and also illustrated the capability of the sensors for

operating in complex media where a large number of proteins and other molecules are present. Through statistical analysis, it was shown that the sensors could differentiate between alkaline phosphatase and PSA.

A new sensor system which implements a passive filter network was modeled and tested experimentally. The system is comprised of narrow-band resonators that are configured in a ladder or lattice network structure. The frequency response of the collective structure contains features that correspond to the operating frequency of each of the resonators that comprise it. When the series or shunt resonators are perturbed with a mass loading event, the resonant frequencies shift. This manifests itself as a shift of the features in the frequency response. This type of structure is passive and can be operated without the use of an oscillator circuit which is a significant advantage over traditional resonator sensors. A 9-element ladder network was fabricated and the responses were analyzed after the deposition of known quantities of mass on the resonators. The results indicate that the sensor system has high sensitivity and holds promise for a new detection technology paradigm.

8.2 Future Work

Now that initial testing has been performed on the TSM sensors, the most logical direction for the research which is currently ongoing is the development of an electrical system that will allow for the real-time simultaneous measurement of the 8 devices on the array. Also currently being developed is a disposable printed circuit board for the sensor chip to mate with. The system (shown in Figure 8.1), when finished, will include a flow cell so that the antibody immobilization and sensor testing can be performed *in situ*. The

disposable sensor board and a non-disposable pcb containing an 8-way RF switch have already been developed. The sensor board plugs into the switch board via a card slot connector. The RF-switch determines which resonator device is being queried by the analysis tool – which in our case will be a network analyzer. The current issues with the system lie in the interface between the sensor chip and the sensor board. If the leads coming from the sensor are too large, a large clamped capacitance will dominate the resonance and drown out the signal. However, if the leads are too small, it will be difficult to interface the chip with the board using conductive epoxy. Therefore, a balance must be met with the design such that the resonance quality is not drastically compromised as this would lead to reduced sensitivity.

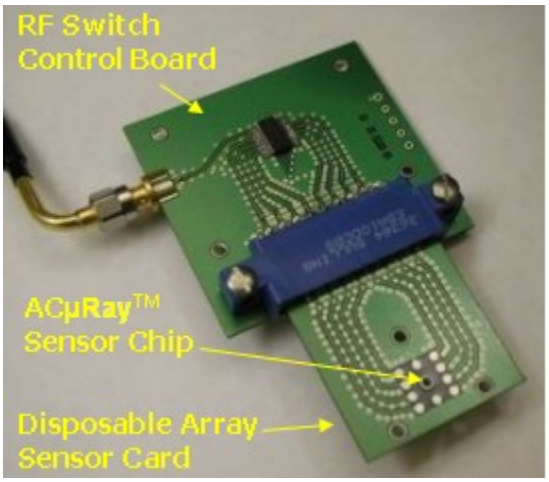

Figure 8.1 An image of the sensor array interface system. The system is comprised of a disposable sensor card to which the sensor array would be bonded. The sensor card then connects to the RF switch control board via a card-slot connector.

The sensor experiments for mesothelin and PSA indicate that the mass resolution of the sensors must be improved. This could be accomplished by further improving the Q of the resonators to reduce the noise and increase the sensitivity to mass perturbation. Investigations are already underway to look at higher harmonics of the fundamental resonance which may have improved Q. Also, a systematic characterization of the

acoustic mirror should be carried out to find the optimal thicknesses for the reflector materials to give the strongest resonance. In the design phase, a smaller-scale study was carried out to optimize the mirror, but it is believed that further improvements may be achieved if a wider range of thicknesses are tested.

The ladder filter network project has significant potential for future sensor research. In the past, engineers have designed acoustic filters to have very specific pass-band responses. However, they have never before been designed from a sensor's viewpoint. An interesting topic for future research is that of exploring the contribution of each individual resonator on the total response so that a change in the response can be mapped back to a single sensor. This also will then open the door for researchers to look at how to best design a frequency response specifically for sensors purposes.

With the proper development, acoustic sensors have the potential to make a significant impact on the field of medical diagnostics. Because of the innate sensitivity to perturbation that acoustic sensors possess, the applications for the technology are endless. It is the job of the engineers to continue developing and improving acoustic biosensor technology platforms while continuing to explore new avenues of research in the development of new sensor systems.

8.3 Published/Presented Works

Journal Papers

C. D. Corso, D. D. Stubbs, S. H. Lee *et al.*, "Real-time detection of mesothelin in pancreatic cancer cell line supernatant using an acoustic wave immunosensor," *Cancer Detect Prev,* vol. 30, no. 2, pp. 180-7, 2006.

C. D. Corso, A. Dickherber, and W. D. Hunt, “Lateral field excitation of thickness shear mode waves in a thin film ZnO solidly mounted resonator,” jointly in *Journal of Applied Physics,* vol. 101, 2007 & *Virtual Journal of Biological Physics Research*, 15 Mar 2007

A. Dickherber, C. D. Corso, and W. D. Hunt, “Optimization and characterization of a ZnO biosensor array,” Sensors and Actuators A: Physical, vol. *In Press.*

C. D. Corso, P. J. Edmonson, A. Dickherber, W. D. Hunt, “A multi-element acoustic wave device sensor based on a filter network configuration,” *Sensors & Actuators A: Physical*, *(Submitted)*, 2008.

C. D. Corso, A. Dickherber, and W. D. Hunt, “An investigation of antibody immobilization methods employing organosilanes on planar ZnO surfaces for biosensor applications,” *Biosensors & Bioelectronics*, (*Submitted)*, 2008.

Conference Papers

A. Dickherber, C. D. Corso, and W. Hunt, "Stability of a RF sputtered ZnO solidly mounted resonator sensor in varying temperature and conductivity environments," Proceedings of the IEEE Sensors 2007 Conference. pp. 1440-3.

C. D. Corso, A. Dickherber, and W. D. Hunt, "A thickness shear mode zinc oxide liquid sensor with off-axis excitation," Proceedings of the IEEE Sensors 2007 Conference. pp. 931-3.

A. Dickherber, C. D. Corso, and W. D. Hunt, "Lateral field excitation (LFE) of thickness shear mode (TSM) acoustic waves in thin film bulk acoustic resonators (FBAR) as a potential biosensor," Conference Proceedings. Annual International Conference of the IEEE EMBS pp. 4

Conference Presentations

W. D. Hunt, C. D. Corso, and A. Dickherber, “Piezoelectric Bulk Acoustic Wave Biosensors for Real-Time Biomarker Detection in Complex Media,” *Moving Biosensors to Point-of-Care Cancer Diagnostics (National Cancer Institute Conference)*, Rockville, MD, June 8-9, 2005.

C. D. Corso, A. Dickherber, P. Shah et al., “Development of a Simple Inexpensive Bulk Acoustic Wave (BAW) Nanosensor for Cancer Biomarkers: Detection of Secreted Sonic Hedgehog from Prostate Cancer Cells” American Association of Cancer Researchers, Washington, D.C., 2006.

A. Dickherber, C. D. Corso, W. D. Hunt et al., "Mesothelin-fc fusion protein detection using a novel microelectronic acoustic sensor platform," 2007 AACR International Conference on Molecular Diagnostics in Cancer Therapeutic Development, Sept 17-20, 2007.

C. D. Corso, A. Dickherber, I. K. Pastan, W. D. Hunt "Development and functionalization of a ZnO-based acoustic sensor array for cancer biomarker detection," MD/PhD Program Summer Retreat, Atlanta, GA, 2007.

Filed and Provisional Patents

P. J. Edmonson, W. D. Hunt, C. D. Corso et al., An Acoustic Wave Sensor Assembly Utilizing A Multi-Element Structure, Application No. 11/822045, USPTO, *filed* 2007.

C. D. Corso, W. D. Hunt, "*Piezoelectric nanoparticle drug delivery via ultrasound excitation.*" GTRC ID No. 3507 (*provisional)*

C. D. Corso, W. D. Hunt, "*Method for Detecting Relative Analyte Levels by Comparison to a Normal Sample*" GTRC ID No. 3508 (*provisional)*

A. Dickherber, C. D. Corso, W. D. Hunt, "*A Novel High Quality Bulk Acoustic Wave Thickness Shear Mode Resonator/Transducer by Lateral Field Excitation of a Multi-layer Piezoelectric Bulk*," GTRC ID No. 3911 (*provisional)*

REFERENCES

[1] G. L. Perkins, E. D. Slater, G. K. Sanders, and J. G. Prichard, "Serum tumor markers," *Am Fam Physician,* vol. 68, pp. 1075-82, Sep 15 2003.

[2] A. Jemal, R. Siegel, E. Ward, T. Murray, J. Xu, C. Smigal, and M. J. Thun, "Cancer statistics, 2006," *CA Cancer J Clin,* vol. 56, pp. 106-30, Mar-Apr 2006.

[3] R. E. Ritts and H. A. Pitt, "CA 19-9 in pancreatic cancer," *Surg Oncol Clin N Am,* vol. 7, pp. 93-101, Jan 1998.

[4] M. K. Gupta, R. Arciaga, L. Bocci, R. Tubbs, R. Bukowski, and S. D. Deodhar, "Measurement of a monoclonal-antibody-defined antigen (CA19-9) in the sera of patients with malignant and nonmalignant diseases. Comparison with carcinoembryonic antigen," *Cancer,* vol. 56, pp. 277-83, Jul 15 1985.

[5] K. Chang and I. Pastan, "Molecular cloning and expression of a cDNA encoding a protein detected by the K1 antibody from an ovarian carcinoma (OVCAR-3) cell line," *Int J Cancer,* vol. 57, pp. 90-7, Apr 1 1994.

[6] K. Chang and I. Pastan, "Molecular cloning of mesothelin, a differentiation antigen present on mesothelium, mesotheliomas, and ovarian cancers," *Proc Natl Acad Sci U S A,* vol. 93, pp. 136-40, Jan 9 1996.

[7] P. Argani, C. Iacobuzio-Donahue, B. Ryu, C. Rosty, M. Goggins, R. E. Wilentz, S. R. Murugesan, S. D. Leach, E. Jaffee, C. J. Yeo, J. L. Cameron, S. E. Kern, and R. H. Hruban, "Mesothelin is overexpressed in the vast majority of ductal adenocarcinomas of the pancreas: identification of a new pancreatic cancer

marker by serial analysis of gene expression (SAGE)," *Clin Cancer Res,* vol. 7, pp. 3862-8, Dec 2001.

[8] C. A. Iacobuzio-Donahue, A. Maitra, G. L. Shen-Ong, T. van Heek, R. Ashfaq, R. Meyer, K. Walter, K. Berg, M. A. Hollingsworth, J. L. Cameron, C. J. Yeo, S. E. Kern, M. Goggins, and R. H. Hruban, "Discovery of novel tumor markers of pancreatic cancer using global gene expression technology," *Am J Pathol,* vol. 160, pp. 1239-49, Apr 2002.

[9] N. Scholler, N. Fu, Y. Yang, Z. Ye, G. E. Goodman, K. E. Hellstrom, and I. Hellstrom, "Soluble member(s) of the mesothelin/megakaryocyte potentiating factor family are detectable in sera from patients with ovarian carcinoma," *Proc Natl Acad Sci U S A,* vol. 96, pp. 11531-6, Sep 28 1999.

[10] C. Mathelin, C. Koehl, and M. C. Rio, "[Circulating proteinic biomarkers and breast cancer]," *Gynecol Obstet Fertil,* vol. 34, pp. 638-46, Jul-Aug 2006.

[11] A. Martin, M. D. Corte, A. M. Alvarez, J. C. Rodriguez, A. Andicoechea, M. Bongera, S. Junquera, D. Pidal, T. Allende, J. L. Muniz, and F. Vizoso, "Prognostic value of pre-operative serum CA 15.3 levels in breast cancer," *Anticancer Res,* vol. 26, pp. 3965-71, Sep-Oct 2006.

[12] C. D. Corso, D. D. Stubbs, S. H. Lee, M. Goggins, R. H. Hruban, and W. D. Hunt, "Real-time detection of mesothelin in pancreatic cancer cell line supernatant using an acoustic wave immunosensor," *Cancer Detect Prev,* vol. 30, pp. 180-7, 2006.

[13] C. D. Corso, A. Dickherber, and W. D. Hunt, "A Thickness Shear Mode Zinc Oxide Liquid Sensor with Off-axis Excitation," in *Sensors, 2007 IEEE*, 2007, pp. 930-933.

[14] C. D. Corso, A. Dickherber, and W. D. Hunt, "Lateral field excitation of thickness shear mode waves in a thin film ZnO solidly mounted resonator," *Journal of Applied Physics,* vol. 101, pp. 54514-1, 2007.

[15] A. Dickherber, C. D. Corso, and W. Hunt, "Stability of a RF sputtered ZnO solidly mounted resonator sensor in varying temperature and conductivity environments," in *Sensors, 2007 IEEE*, 2007, pp. 1440-1443.

[16] R. L. Miller, C. E. Nothnick, and D. S. Bailey, *Acoustic charge transport : device technology and applications*. Boston: Artech House, 1992.

[17] J. F. Rosenbaum, *Bulk acoustic wave theory and devices*. Boston: Artech House, 1988.

[18] B. A. Auld, *Acoustic Fields and Waves In Solids*, 2nd ed. vol. I. Malabar, FL: Krieger, 1973.

[19] D. S. Ballantine, *Acoustic wave sensors : theory, design, and physico-chemical applications*. San Diego: Academic Press, 1997.

[20] Z. Hao, M. S. Marma, K. Eun Sok, C. E. McKenna, and M. E. Thompson, "Implantable resonant mass sensor for liquid biochemical sensing," in *Micro Electro Mechanical Systems, 2004. 17th IEEE International Conference on. (MEMS)*, 2004, pp. 347-350.

[21] H. Zhang and E. S. Kim, "Micromachined Acoustic Resonant Mass Sensor," *Microelectromechanical Systems, Journal of,* vol. 14, pp. 699-706, 2005.

[22] R. Gabl, E. Green, M. Schreiter, H. D. Feucht, H. Zeininger, R. Primig, D. Pitzer, G. Eckstein, and W. Wersing, "Novel integrated FBAR sensors: a universal

technology platform for bio- and gas-detection," in *Sensors, 2003. Proceedings of IEEE*, 2003, pp. 1184-1188 Vol.2.

[23] I. Ben-Dov, I. Willner, and E. Zisman, "Piezoelectric immunosensors for urine specimens of Chlamydia trachomatis employing quartz crystal microbalance microgravimetric analyses," *Anal Chem,* vol. 69, pp. 3506-12, Sep 1 1997.

[24] F. N. Dultsev, R. E. Speight, M. T. Fiorini, J. M. Blackburn, C. Abell, V. P. Ostanin, and D. Klenerman, "Direct and quantitative detection of bacteriophage by "hearing" surface detachment using a quartz crystal microbalance," *Anal Chem,* vol. 73, pp. 3935-9, Aug 15 2001.

[25] M. S. Jenkins, K. C. Wong, O. Chhit, J. F. Bertram, R. J. Young, and N. Subaschandar, "Quartz crystal microbalance-based measurements of shear-induced senescence in human embryonic kidney cells," *Biotechnol Bioeng,* vol. 88, pp. 392-8, Nov 5 2004.

[26] Y. Luo, M. Chen, Q. Wen, M. Zhao, B. Zhang, X. Li, F. Wang, Q. Huang, C. Yao, T. Jiang, G. Cai, and W. Fu, "Rapid and simultaneous quantification of 4 urinary proteins by piezoelectric quartz crystal microbalance immunosensor array," *Clin Chem,* vol. 52, pp. 2273-80, Dec 2006.

[27] M. Muratsugu, F. Ohta, Y. Miya, T. Hosokawa, S. Kurosawa, N. Kamo, and H. Ikeda, "Quartz crystal microbalance for the detection of microgram quantities of human serum albumin: relationship between the frequency change and the mass of protein adsorbed," *Anal Chem,* vol. 65, pp. 2933-7, Oct 15 1993.

[28] E. Uttenthaler, M. Schraml, J. Mandel, and S. Drost, "Ultrasensitive quartz crystal microbalance sensors for detection of M13-Phages in liquids," *Biosens Bioelectron,* vol. 16, pp. 735-43, Dec 2001.

[29] Y. Y. Wong, S. P. Ng, M. H. Ng, S. H. Si, S. Z. Yao, and Y. S. Fung, "Immunosensor for the differentiation and detection of Salmonella species based on a quartz crystal microbalance," *Biosens Bioelectron,* vol. 17, pp. 676-84, Aug 2002.

[30] Z. Yang, S. Si, C. Zhang, and G. Song, "Quartz crystal microbalance studies on bilirubin adsorption on self-assembled phospholipid bilayers," *J Colloid Interface Sci,* vol. 305, pp. 1-6, Jan 1 2007.

[31] M. Meissner, L. A. French, W. Pinkham, C. York, G. Bernhardt, M. P. Pereira da Cunha, and J. F. Vetelillo, "Electrode optimization for a lateral field excited acoustic wave sensor," in *Ultrasonics Symposium, 2004 IEEE*. vol. 1, 2004, pp. 314-318 Vol.1.

[32] J. Weber, W. M. Albers, J. Tuppurainen, M. Link, R. Gabl, W. Wersing, and M. Schreiter, "Shear mode FBARs as highly sensitive liquid biosensors," *Sensors and Actuators A: Physical,* vol. 128, pp. 84-88, 2006.

[33] C. Campbell, *Surface acoustic wave devices and their signal processing applications*. Boston: Academic Press, 1989.

[34] D. D. Stubbs, S. H. Lee, and W. D. Hunt, "Investigation of cocaine plumes using surface acoustic wave immunoassay sensors," *Analytical Chemistry,* vol. 75, pp. 6231-6235, Nov 2003.

[35] E. Berkenpas, P. Millard, and M. Pereira da Cunha, "Detection of Escherichia coli O157:H7 with langasite pure shear horizontal surface acoustic wave sensors," *Biosens Bioelectron,* vol. 21, pp. 2255-62, Jun 15 2006.

[36] F. Martin, M. I. Newton, G. McHale, K. A. Melzak, and E. Gizeli, "Pulse mode shear horizontal-surface acoustic wave (SH-SAW) system for liquid based sensing applications," *Biosens Bioelectron,* vol. 19, pp. 627-32, Jan 15 2004.

[37] D. W. Branch and S. M. Brozik, "Low-level detection of a bacillus anthracis simulant using Love-wave biosensors on 36 degrees YX LiTaO3," *Biosens Bioelectron,* vol. 19, pp. 849-59, Mar 15 2004.

[38] T. M. A. Gronewold, S. Glass, E. Quandt, and M. Famulok, "Monitoring complex formation in the blood-coagulation cascade using aptamer-coated SAW sensors," *Biosensors and Bioelectronics,* vol. 20, pp. 2044-2052, 2005.

[39] D. D. Stubbs, W. D. Hunt, S. H. Lee, and D. F. Doyle, "Gas phase activity of anti-FITC antibodies immobilized on a surface acoustic wave resonator device," *Biosens Bioelectron,* vol. 17, pp. 471-7, Jun 2002.

[40] J. Andle, J. Vetelino, M. Lade, and D. McAllister, "Detection of nucleic acid hybridization with an acoustic plate mode microsensor," Honolulu, HI, USA: IEEE, 1990, pp. 291-4.

[41] J. C. Andle, J. F. Vetelino, M. W. Lade, and D. J. McAllister, "An acoustic plate mode biosensor," *Sensors and Actuators B (Chemical),* vol. B8, pp. 191-8, 1992.

[42] J. C. Andle, J. F. Vetelino, R. Lec, and D. J. McAllister, "An acoustic plate mode immunosensor," Hilton Head Island, SC, USA: IEEE, 1990, pp. 82-5.

[43] R. Dahint and F. Bender, "A concentration dependent study of acoustic plate mode immunosensor response using antigen/antibody systems with different binding ability," *IEEE Transactions on Ultrasonics, Ferroelectrics and Frequency Control,* vol. 45, pp. 1216-20, 1998.

[44] J. Pepper, R. Noring, M. Klempner, B. Cunningham, A. Petrovich, R. Bousquet, C. Clapp, J. Brady, and B. Hugh, "Detection of proteins and intact microorganisms using microfabricated flexural plate silicon resonator arrays," *Sensors and Actuators, B: Chemical,* vol. 96, pp. 565-575, 2003.

[45] C.-J. Shih, W.-W. Ke, and C.-H. Lieu, "Detecting drug screen by acoustic wave sensor," Anaheim, CA, United States: Nano Science and Technology Institute, Cambridge, MA 02139, United States, 2005, pp. 474-476.

[46] J. Curie and P. Curie, "An oscillating quartz crystal mass detector," *Rendu,* vol. 91, pp. 294-297, 1880.

[47] A. Shons, F. Dorman, and J. Najarian, "An immunospecific microbalance," *J Biomed Mater Res,* vol. 6, pp. 565-70, Nov 1972.

[48] S. F. Chou, W. L. Hsu, J. M. Hwang, and C. Y. Chen, "Determination of alpha-fetoprotein in human serum by a quartz crystal microbalance-based immunosensor," *Clin Chem,* vol. 48, pp. 913-8, Jun 2002.

[49] Z. Y. Wu, G. L. Shen, S. P. Wang, and R. Q. Yu, "Quartz-crystal microbalance immunosensor for Schistsoma-japonicum-infected rabbit serum," *Anal Sci,* vol. 19, pp. 437-40, Mar 2003.

[50] X. L. Su and Y. Li, "A self-assembled monolayer-based piezoelectric immunosensor for rapid detection of Escherichia coli O157:H7," *Biosens Bioelectron,* vol. 19, pp. 563-74, Jan 15 2004.

[51] C. D. Corso, A. Dickherber, P. Shah, A. Migdal, M. W. Datta, D. Sumana, and W. D. Hunt, "Development of a Simple Inexpensive Bulk Acoustic Wave (BAW) Nanosensor for Cancer Biomarkers: Detection of Secreted Sonic Hedgehog from Prostate Cancer Cells " *American Association of Cancer Researchers,* vol. Washington, D.C., 2006.

[52] G. Sauerbrey, "Use of vibrating quartz for thin film weighing and microweighing (in German)," *Z. Phys. ,* vol. 155, pp. 206-222, 1959.

[53] W. D. Hunt, D. D. Stubbs, and L. Sang-Hun, "Time-dependent signatures of acoustic wave biosensors," *Proceedings of the IEEE,* vol. 91, pp. 890-901, 2003.

[54] K. K. Kanazawa and J. G. Gordon, "Frequency of a quartz microbalance in contact with liquid," *Anal. Chem.,* vol. 57, pp. 1770-1771, 1985.

[55] S. P. Sakti, R. Lucklum, P. Hauptmann, F. Buhling, and S. Ansorge, "Disposable TSM-biosensor based on viscosity changes of the contacting medium," *Biosensors and Bioelectronics,* vol. 16, pp. 1101-1108, 2001.

[56] *IEEE Standard on Piezoelectricity*. New York The Institute of Electrical and Electronics Engineers, Inc, 1987.

[57] V. E. Bottom, *Introduction to Quartz Crystal Unit Design*. New York: Van Nostrand Reinhold, 1982.

[58] C. Crystals, "www.crovencrystals.com/quartzhistory.htm," 2007.

[59] W. P. Mason, *Piezoelectric Crystals and Their Application to Ultrasonics*. New York: Van Nostrand, 1950.

[60] R. Bechman, "Elastic and Piezoelectric Constants of Alpha-Quartz," *Physical Review,* vol. 110, pp. 1060-1061, 1958.

[61] F. Lu, Lee, H. P., Lim, S. P., "Finite element modeling and analysis of multi-channel quartz crystal microbalance," *Sensors, 2003. Proceedings of IEEE,* vol. 2, pp. 888-892, 2003.

[62] K. L. Prime and G. M. Whitesides, "Self-assembled organic monolayers: model systems for studying adsorption of proteins at surfaces," *Science,* vol. 252, pp. 1164-7, May 24 1991.

[63] S. H. Lee, D. D. Stubbs, J. Cairney, and W. D. Hunt, "Real-time detection of bacteria spores using a QCM based immunosensor." vol. Vol.2 Toronto, Ont., Canada: IEEE, 2003, pp. 1194-8.

[64] R. L. Stanfield, T. M. Fieser, R. A. Lerner, and I. A. Wilson, "Crystal structures of an antibody to a peptide and its complex with peptide antigen at 2.8 A," *Science,* vol. 248, pp. 712-9, May 11 1990.

[65] S. L. Pinkett, W. D. Hunt, B. P. Barber, and P. L. Gammel, "Determination of ZnO temperature coefficients using thin film bulk acoustic wave resonators," *Ultrasonics, Ferroelectrics and Frequency Control, IEEE Transactions on,* vol. 49, pp. 1491- 1496, Nov 2002 2002.

[66] S. L. Pinkett, "Techniques to facilitate the fabrication of zinc oxide-based thin film bulk acoustic wave devices," in *Electrical and Computer Engineering*. vol. Doctor of Philosophy Atlanta: Georgia Institute of Technology, 2003.

[67] J. V. Atanasoff and P. J. Hart, "Dynamical determination of the elastic constants and their temperature coefficients for quartz," *Physical Review,* vol. 59, pp. 85-96, 1941.

[68] R. Bechmann, "Parallel Field Excitation of Thickness Modes of Quartz Plates," pp. 68-88, 1960.

[69] E. R. Hatch and A. Ballato, "Lateral-Field Excitation of Quartz Plates," pp. 512-515, 1983.

[70] A. W. Warner, "Use of Parallel-Field Excitation in the Design of Quartz Crystal Units," pp. 248-266, 1963.

[71] H. Yihe, L. A. French, Jr., K. Radecsky, M. Pereira da Cunha, P. Millard, and J. F. Vetelino, "A lateral field excited liquid acoustic wave sensor," *IEEE Transactions on Ultrasonics, Ferroelectrics and Frequency Control,* vol. 51, pp. 1373-80, 2004.

[72] H. Yihe, L. A. French, Jr., K. Radecsky, M. Pereira da Cunha, P. Millard, and J. F. Vetelino, "A lateral field excited liquid acoustic wave sensor," *Ultrasonics, Ferroelectrics and Frequency Control, IEEE Transactions on,* vol. 51, pp. 1373-1380, 2004.

[73] W. Pinkham, M. Wark, S. Winters, L. French, D. J. Frankel, and J. F. Vetelino, "A lateral field excited acoustic wave pesticide sensor." vol. 4, 2005, pp. 2279-2283.

[74] C. York, L. A. French, P. Millard, and J. F. Vetelino, "A lateral field excited acoustic wave biosensor," 2005, pp. 44-49.

[75] A. Ballato, E. R. Hatch, M. Mizan, and T. J. Lukaszek, "Lateral Field Equivalent Networks and Piezocoupling Factors of Quartz Plates Driven in Simple Thickness Modes," *Ultrasonics, Ferroelectrics and Frequency Control, IEEE Transactions on,* vol. 33, pp. 385-393, 1986.

[76] S. V. Krishnaswamy, B. R. McAvoy, W. J. Takei, and R. A. Moore, "Oriented ZnO Films for Microwave Shear Mode Transducers," 1982, pp. 476-479.

[77] J. S. Wang and K. M. Lakin, "Sputtered C-Axis Inclined ZnO Films for Shear Wave Resonators," 1982, pp. 480-483.

[78] M. Link, M. Schreiter, J. Weber, R. Gabl, D. Pitzer, R. Primig, W. Wersing, M. B. Assouar, and O. Elmazria, "c-axis inclined ZnO films for shear-wave transducers deposited by reactive sputtering using an additional blind," *Journal of Vacuum Science & Technology A: Vacuum, Surfaces, and Films,* vol. 24, pp. 218-222, 2006.

[79] M. Link, M. Schreiter, J. Weber, R. Primig, D. Pitzer, and R. Gabl, "Solidly mounted ZnO shear mode film bulk acoustic resonators for sensing applications in liquids," *Ultrasonics, Ferroelectrics and Frequency Control, IEEE Transactions on,* vol. 53, pp. 492-496, 2006.

[80] P. Wei, Y. Hongyu, K. Jae Wan, Z. Hao, and K. Eun Sok, "Self-aligned lateral field excitation film acoustic resonator with very large electromechanical coupling [FBAR]," 2004, pp. 558-561.

[81] K. M. Lakin, G. R. Kline, and K. T. McCarron, "Development of miniature filters for wireless applications," in *Microwave Symposium Digest, 1995., IEEE MTT-S International*, 1995, pp. 883-886 vol.2.

[82] W. E. Newell, "Face-mounted piezoelectric resonators," *Proceedings of the IEEE,* vol. 53, pp. 575-581, 1965.

[83] K. M. Lakin, K. M. Lakin, K. T. McCarron, and R. E. Rose, "Solidly mounted resonators and filters," in *Ultrasonics Symposium, 1995. Proceedings., 1995 IEEE*, 1995, pp. 905-908.

[84] K. M. Lakin, G. R. Kline, and K. T. McCarron, "Development of miniature filters for wireless applications," *IEEE Transactions on Microwave Theory and Techniques,* vol. 43, pp. 2933-2939, 1995.

[85] L. Woo Wai, S. Yonghua, and K. Eun Sok, "Lateral-field-excitation acoustic resonators for monolithic oscillators and filters," 1996, pp. 558-562.

[86] A. Dickherber, C. D. Corso, and W. D. Hunt, "Optimization and characterization of a ZnO biosensor array," *Sensors & Actuators: A. Physical,* vol. 144, pp. 7-12, 2008.

[87] W. Pan, C. J. Durning, and N. J. Turro, "Kinetics of alkanethiol adsorption on gold," *Langmuir,* vol. 12, pp. 4469-4473, Sep 1996.

[88] D. L. Allara and R. G. Nuzzo, "Spontaneously Organized Molecular Assemblies .1. Formation, Dynamics, and Physical-Properties of Normal-Alkanoic Acids Adsorbed from Solution on an Oxidized Aluminum Surface," *Langmuir,* vol. 1, pp. 45-52, 1985.

[89] S. K. Bhatia, L. C. Shriver-Lake, K. J. Prior, J. H. Georger, J. M. Calvert, R. Bredehorst, and F. S. Ligler, "Use of thiol-terminal silanes and heterobifunctional crosslinkers for immobilization of antibodies on silica surfaces," *Anal Biochem,* vol. 178, pp. 408-13, May 1 1989.

[90] L. C. Shriver-Lake, B. Donner, R. Edelstein, K. Breslin, S. K. Bhatia, and F. S. Ligler, "Antibody immobilization using heterobifunctional crosslinkers," *Biosensors & Bioelectronics,* vol. 12, pp. 1101-1106, 1997.

[91] I. Luzinov, D. Julthongpiput, A. Liebmann-Vinson, T. Cregger, M. D. Foster, and V. V. Tsukruk, "Epoxy-terminated self-assembled monolayers: Molecular glues for polymer layers," *Langmuir,* vol. 16, pp. 504-516, Jan 2000.

[92] V. V. Tsukruk, I. Luzinov, and D. Julthongpiput, "Sticky Molecular Surfaces: Epoxysilane Self-Assembled Monolayers," *Langmuir,* vol. 15, pp. 3029-3032, 1999.

[93] C. M. Ruan, L. J. Yang, and Y. B. Li, "Immunobiosensor chips for detection of Escherichia coli O157 : H7 using electrochemical impedance spectroscopy," *Analytical Chemistry,* vol. 74, pp. 4814-4820, Sep 2002.

[94] L. Yang and Y. Li, "AFM and impedance spectroscopy characterization of the immobilization of antibodies on indium-tin oxide electrode through self-assembled monolayer of epoxysilane and their capture of Escherichia coli O157:H7," *Biosens Bioelectron,* vol. 20, pp. 1407-16, Jan 15 2005.

[95] P. H. Mutin, G. Guerrero, and A. Vioux, "Organic-inorganic hybrid materials based on organophosphorus coupling molecules: from metal phosphonates to surface modification of oxides," *Comptes Rendus Chimie,* vol. 6, pp. 1153-1164, Aug-Oct 2003.

[96] M. A. Aziz and H. Yang, "Electrochemical immunosensor using the modification of an amine-functionalized indium tin oxide electrode with carboxylated single-

walled carbon nanotubes," *Bulletin of the Korean Chemical Society,* vol. 28, pp. 1171-1174, Jul 2007.

[97] G. Guerrero, P. H. Mutin, and A. Vioux, "Anchoring of phosphonate and phosphinate coupling molecules on titania particles," *Chemistry of Materials,* vol. 13, pp. 4367-4373, Nov 2001.

[98] M. M. Demir, K. Koynov, U. Akbey, C. Bubeck, I. Park, I. Lieberwirth, and G. Wegner, "Optical properties of composites of PMMA and surface-modified zincite nanoparticles," *Macromolecules,* vol. 40, pp. 1089-1100, Feb 2007.

[99] P. Kim, S. C. Jones, P. J. Hotchkiss, J. N. Haddock, B. Kippelen, S. R. Marder, and J. W. Perry, "Phosphonic acid-modiried barium titanate polymer nanocomposites with high permittivity and dielectric strength," *Advanced Materials,* vol. 19, pp. 1001-+, Apr 2007.

[100] T. L. Breen, P. M. Fryer, R. W. Nunes, and M. E. Rothwell, "Patterning Indium Tin Oxide and Indium Zinc Oxide Using Microcontact Printing and Wet Etching," *Langmuir,* vol. 18, pp. 194-197, 2002.

[101] S. Krishnamoorthy, T. Bei, E. Zoumakis, G. P. Chrousos, and A. A. Iliadis, "Morphological and binding properties of interleukin-6 on thin ZnO films grown on (100) silicon substrates for biosensor applications," *Biosens Bioelectron,* vol. 22, pp. 707-14, Dec 15 2006.

[102] L. Thomsen, B. Watts, and P. C. Dastoor, "A NEXAFS orientation study of gamma-aminopropyltriethoxysilane on zinc oxide surfaces," *Surface and Interface Analysis,* vol. 38, pp. 1139-1145, 2006.

[103] B. Watts, L. Thomsen, J. R. Fabien, and P. C. Dastoor, "Understanding the Conformational Dynamics of Organosilanes: gamma-APS on Zinc Oxide Surfaces," *Langmuir,* vol. 18, pp. 148-154, 2002.

[104] A. Kornherr, S. A. French, A. A. Sokol, C. R. A. Catlow, S. Hansal, W. E. G. Hansal, J. O. Besenhard, H. Kronberger, G. E. Nauer, and G. Zifferer, "Interaction of adsorbed organosilanes with polar zinc oxide surfaces: a molecular dynamics study comparing two models for the metal oxide surface," *Chemical Physics Letters,* vol. 393, pp. 107-11, 2004.

[105] P. W. Sadik, S. J. Pearton, D. P. Norton, E. Lambers, and F. Ren, "Functionalizing Zn- and O-terminated ZnO with thiols," *Journal of Applied Physics,* vol. 101, pp. 104514-5, 2007.

[106] T. Y. Liu, H. C. Liao, C. C. Lin, S. H. Hu, and S. Y. Chen, "Biofunctional ZnO Nanorod Arrays Grown on Flexible Substrates," *Langmuir,* vol. 22, pp. 5804-5809, 2006.

[107] J. W. Soares, D. M. Steeves, D. Ziegler, and B. S. DeCristofano, "Surface modification of nanocrystalline zinc oxide for bio-sensing applications," *Nanomaterial Synthesis and Integration for Sensors, Electronics, Photonics, and Electro-Optics,* vol. 6370, pp. 637011-9, 2006.

[108] M. Y. Tsai and J. C. Lin, "Surface characterization and platelet adhesion studies of self-assembled monolayer with phosphonate ester and phosphonic acid functionalities," *Journal of Biomedical Materials Research,* vol. 55, pp. 554-565, Jun 2001.

[109] A. Tlili, A. Abdelghani, K. Aguir, M. Gillet, and N. Jaffrezic-Renault, "Adsorption characteristics of self-assembled thiol and dithiol layer on gold," *Materials Science & Engineering C-Biomimetic and Supramolecular Systems,* vol. 27, pp. 620-624, May 2007.

[110] M. D. Porter, T. B. Bright, D. L. Allara, and C. E. D. Chidsey, "Spontaneously organized molecular assemblies. 4. Structural characterization of n-alkyl thiol monolayers on gold by optical ellipsometry, infrared spectroscopy, and electrochemistry," *J. Am. Chem. Soc.,* vol. 109, pp. 3559-3568, 1987.

[111] K. Chang, I. Pastan, and M. C. Willingham, "Frequent expression of the tumor antigen CAK1 in squamous-cell carcinomas," *Int J Cancer,* vol. 51, pp. 548-54, Jun 19 1992.

[112] N. G. Ordonez, "Application of mesothelin immunostaining in tumor diagnosis," *Am J Surg Pathol,* vol. 27, pp. 1418-28, Nov 2003.

[113] R. Hassan, T. Bera, and I. Pastan, "Mesothelin: a new target for immunotherapy," *Clin Cancer Res,* vol. 10, pp. 3937-42, Jun 15 2004.

[114] R. Hassan, A. T. Remaley, M. L. Sampson, J. Zhang, D. D. Cox, J. Pingpank, R. Alexander, M. Willingham, I. Pastan, and M. Onda, "Detection and quantitation of serum mesothelin, a tumor marker for patients with mesothelioma and ovarian cancer," *Clin Cancer Res,* vol. 12, pp. 447-53, Jan 15 2006.

[115] J. Creaney, D. Yeoman, L. K. Naumoff, M. Hof, A. Segal, A. W. Musk, N. De Klerk, N. Horick, S. J. Skates, and B. W. Robinson, "Soluble mesothelin in effusions: a useful tool for the diagnosis of malignant mesothelioma," *Thorax,* vol. 62, pp. 569-76, Jul 2007.

[116] B. W. Robinson, J. Creaney, R. Lake, A. Nowak, A. W. Musk, N. de Klerk, P. Winzell, K. E. Hellstrom, and I. Hellstrom, "Mesothelin-family proteins and diagnosis of mesothelioma," *Lancet,* vol. 362, pp. 1612-6, Nov 15 2003.

[117] M. Onda, M. Willingham, S. Nagata, T. K. Bera, R. Beers, M. Ho, R. Hassan, R. J. Kreitman, and I. Pastan, "New monoclonal antibodies to mesothelin useful for immunohistochemistry, fluorescence-activated cell sorting,Western blotting, and ELISA," *Clinical Cancer Research,* vol. 11, pp. 5840-5846, Aug 2005.

[118] L. C. Shriver-Lake and F. S. Ligler, "The array biosensor for counterterrorism," *Sensors Journal, IEEE,* vol. 5, pp. 751-756, 2005.

[119] Y. Zuo, S. Chakrabartty, Z. Muhammad-Tahir, S. Pal, and E. C. Alocilja, "Spatio-Temporal Processing for Multichannel Biosensors Using Support Vector Machines," *Sensors Journal, IEEE,* vol. 6, pp. 1644-1651, 2006.

[120] K. M. Lakin, G. R. Kline, and K. T. McCarron, "Development of miniature filters for wireless applications," *Microwave Symposium Digest, 1995., IEEE MTT-S International,* pp. 883-886, 1995.

[121] G. G. Fattinger, J. Kaitila, R. Aigner, and W. Nessler, "Thin film bulk acoustic wave devices for applications at 5.2 GHz," *Ultrasonics, 2003 IEEE Symposium,* vol. 1, pp. 174-177, 2003.

[122] J. Kaitila, M. Ylilammi, J. Molarius, J. Ella, and T. Makkonen, "ZnO based thin film bulk acoustic wave filters for EGSM band," *Ultrasonics Symposium, 2001 IEEE,* vol. 1, pp. 803-806, 2001.

[123] R. Weigel, K. Weigenthaler, R. Dill, and I. Schropp, "A 900 MHz ladder-type SAW filter duplexer," *Microwave Symposium Digest, 1996., IEEE MTT-S International,* vol. 2, pp. 413-416, 1996.

[124] K. M. Lakin, "Thin film BAW filters for wide bandwidth and high performance applications," *Microwave Symposium Digest, 2004 IEEE MTT-S International,* vol. 2, pp. 923-926, 2004.

[125] K. M. Lakin, "Thin film resonator technology," *Proceedings of the 2003 IEEE International Frequency Control Symposium and PDA Exhibition.,* pp. 765-78, 2003.

[126] A. Arnau, Y. Jimenez, and T. Sogorb, "An extended Butterworth Van Dyke model for quartz crystal microbalance applications in viscoelastic fluid media," *Ultrasonics, Ferroelectrics and Frequency Control, IEEE Transactions on,* vol. 48, pp. 1367-1382, 2001.

[127] K. Yoonkee, J. R. Vig, and A. Ballato, "Doubly rotated resonators for sensing the properties of liquids," *Ultrasonics, 2003 IEEE Symposium,* vol. 1, pp. 52-55, 2003.

[128] K. M. Lakin, J. Belsick, J. F. McDonald, and K. T. McCarron, "Improved bulk wave resonator coupling coefficient for wide bandwidth filters," *Ultrasonics Symposium, 2001 IEEE,* vol. 1, pp. 827-831, 2001.

[129] K. K. Kanazawa and J. G. Gordon, "Frequency of a Quartz Microbalance in Contact with Liquid," *Analytical Chemistry,* vol. 57, pp. 1770-1771, 1985.

[130] C. B. Saw, P. M. Smith, P. J. Edmonson, and C. K. Campbell, "Mode selection in a multimode SAW oscillator using FM chirp mixing signal injection," *IEEE*

Transactions on Ultrasonics, Ferroelectrics and Frequency Control, vol. 35, pp. 390-5, 1988.

[131] C. D. Corso, A. Dickherber, and W. D. Hunt, "A thickness shear mode zinc oxide liquid sensor with off-axis excitation," Atlanta, GA, USA: IEEE, 2007, pp. 931-3.

[132] C. D. Corso, A. Dickherber, and W. D. Hunt, "An investigation of antibody immobilization methods employing organosilanes on planar ZnO surfaces for biosensor applications," *Biosensors & Bioelectronics,* 2008.

[133] C. D. Corso, P. J. Edmonson, A. Dickherber, and W. Hunt, "A multi-element acoustic wave device sensor based on a filter network configuration," *Sensors & Actuators A,* 2008.

VITA

CHRISTOPHER D. CORSO

Christopher D. Corso was born in Pittsburgh, Pennsylvania. He attended public school in the North Allegheny School District in Allegheny County, Pennsylvania. He received a B.S. in Electrical and Computer Engineering from the Georgia Institute of Technology, Atlanta, GA in 2004. For his doctoral work, he chose to stay at the Georgia Institute of Technology to join the Microelectronic Acoustics Group and pursue a PhD in Bioengineering. He is a student in the MD/PhD program which is a combined degree program between the Georgia Institute of Technology and Emory University. When he is not working on his studies, he enjoys working on his house and cars. He is an avid sports fan and supports the Pittsburgh black and gold. He also enjoys cooking and eating Italian food and playing bocce with friends. He now joins the Emory School of Medicine as part of the MD/PhD program. He currently resides in Decatur, GA with his wife, Mindi and two cats Audrey and Waffles.